

Date: May 18, 2017

## Proposal for JLab PAC45

# Strange Hadron Spectroscopy with a Secondary $K_L$ Beam at GlueX

S. Adhikari<sup>12</sup>, H. Al Ghouli<sup>13</sup>, A. Ali<sup>17</sup>, M. J. Amarian<sup>40,\*†</sup>, E. G. Anassontzis<sup>2</sup>,  
A. V. Anisovich<sup>20,14</sup>, A. Austregesilo<sup>32</sup>, M. Baalouch<sup>40</sup>, F. Barbosa<sup>32</sup>, A. Barnes<sup>9</sup>,  
M. Bashkanov<sup>10,†</sup>, T. D. Beattie<sup>44</sup>, R. Bellwied<sup>22</sup>, V. V. Berdnikov<sup>37</sup>, T. Black<sup>41</sup>, W. Boeglin<sup>12</sup>,  
W. J. Briscoe<sup>15</sup>, T. Britton<sup>32</sup>, W. K. Brooks<sup>46</sup>, B. E. Cannon<sup>13</sup>, E. Chudakov<sup>32</sup>, P. L. Cole<sup>23</sup>,  
V. Crede<sup>13</sup>, M. M. Dalton<sup>32</sup>, A. Deur<sup>32</sup>, P. Degtyarenko<sup>32</sup>, S. Dobbs<sup>42</sup>, G. Dodge<sup>40</sup>,  
A. G. Dolgolenko<sup>29</sup>, M. Döring<sup>15,32</sup>, M. Dugger<sup>1</sup>, R. Dzhygadlo<sup>17</sup>, R. Edwards<sup>32</sup>, H. Egiyan<sup>32</sup>,  
S. Eidelman<sup>4,31</sup>, A. Ernst<sup>13</sup>, A. Eskandarian<sup>15</sup>, P. Eugenio<sup>13</sup>, C. Fanelli<sup>35</sup>, S. Fegan<sup>36</sup>,  
A. M. Foda<sup>44</sup>, J. Frye<sup>24</sup>, S. Furlotov<sup>32</sup>, L. Gan<sup>41</sup>, A. Gasparian<sup>39</sup>, G. Gavalian<sup>32</sup>,  
V. Gauzshtein<sup>47,48</sup>, N. Gevorgyan<sup>50</sup>, D. I. Glazier<sup>16</sup>, K. Goetzen<sup>17</sup>, J. Goity<sup>32,21</sup>,  
V. S. Goryachev<sup>29</sup>, L. Guo<sup>12</sup>, H. Habertzettl<sup>15</sup>, M. Hadžimehmedović<sup>49</sup>, H. Hakobyan<sup>46</sup>,  
A. Hamdi<sup>17</sup>, S. Han<sup>53</sup>, J. Hardin<sup>35</sup>, A. Hayrapetyan<sup>19</sup>, T. Horn<sup>7</sup>, G. M. Huber<sup>44</sup>, C. E. Hyde<sup>40</sup>,  
D. G. Ireland<sup>16</sup>, M. M. Ito<sup>32</sup>, B. C. Jackson<sup>18</sup>, N. S. Jarvis<sup>6</sup>, R. T. Jones<sup>9</sup>, V. Kakoyan<sup>50</sup>,  
G. Kalicy<sup>7</sup>, M. Kamel<sup>12</sup>, C. D. Keith<sup>32</sup>, C. W. Kim<sup>15</sup>, F. J. Klein<sup>15</sup>, C. Kourkouveli<sup>2</sup>,  
S. Kuleshov<sup>46</sup>, I. Kuznetsov<sup>47,48</sup>, A. B. Laptev<sup>30</sup>, I. Larin<sup>29</sup>, D. Lawrence<sup>32</sup>, M. Levillain<sup>39</sup>,  
W. I. Levine<sup>6</sup>, K. Livingston<sup>16</sup>, G. J. Lolos<sup>44</sup>, V. E. Lyubovitskij<sup>47,48,33,46</sup>, D. Mack<sup>32</sup>, M. Mai<sup>15</sup>,  
D. M. Manley<sup>27</sup>, U.-G. Meißner<sup>20,26</sup>, H. Marukyan<sup>50</sup>, V. Mathieu<sup>24</sup>, P. T. Mattione<sup>32</sup>,  
M. Matveev<sup>14</sup>, V. Matveev<sup>29</sup>, M. McCaughan<sup>32</sup>, M. McCracken<sup>6</sup>, W. McGinley<sup>6</sup>, J. McIntyre<sup>9</sup>,  
C. A. Meyer<sup>6</sup>, R. Miskimen<sup>34</sup>, R. E. Mitchell<sup>24</sup>, F. Mokaya<sup>9</sup>, V. Mokeev<sup>32</sup>, K. Nakayama<sup>18</sup>,  
F. Nerling<sup>17</sup>, Y. Oh<sup>28</sup>, H. Osmanović<sup>49</sup>, A. I. Ostrovidov<sup>13</sup>, R. Omerović<sup>49</sup>, Z. Papandreou<sup>44</sup>,  
K. Park<sup>32</sup>, E. Pasyuk<sup>32</sup>, M. Patsyuk<sup>35</sup>, P. Pauli<sup>16</sup>, R. Pedroni<sup>39</sup>, L. Pentchev<sup>32</sup>, K. J. Peters<sup>17</sup>,  
W. Phelps<sup>12</sup>, E. Pooser<sup>32</sup>, B. Pratt<sup>9</sup>, J. W. Price<sup>5</sup>, N. Qin<sup>53</sup>, J. Reinhold<sup>12</sup>, D. Richards<sup>32</sup>,  
D.-O. Riska<sup>11</sup>, B. G. Ritchie<sup>1</sup>, J. Ritman<sup>3,26,†</sup>, L. Robison<sup>42</sup>, D. Romanov<sup>37</sup>, H.-Y. Ryu<sup>43</sup>,  
C. Salgado<sup>38</sup>, E. Santopinto<sup>25</sup>, A. V. Sarantsev<sup>20,14</sup>, R. A. Schumacher<sup>6</sup>, C. Schwarz<sup>17</sup>,  
J. Schwiening<sup>17</sup>, A. Semenov<sup>44</sup>, I. Semenov<sup>44</sup>, K. K. Seth<sup>42</sup>, M. R. Shepherd<sup>24</sup>, E. S. Smith<sup>32</sup>,  
D. I. Sober<sup>7</sup>, D. Sokhan<sup>16</sup>, A. Somov<sup>32</sup>, S. Somov<sup>37</sup>, O. Soto<sup>46</sup>, N. Sparks<sup>1</sup>, J. Stahov<sup>49</sup>,  
M. J. Staib<sup>6</sup>, J. R. Stevens<sup>51,†</sup>, I. I. Strakovsky<sup>15,†</sup>, A. Subedi<sup>24</sup>, A. Švarc<sup>45</sup>, A. Szczepaniak<sup>24,32</sup>,  
V. Tarasov<sup>29</sup>, S. Taylor<sup>32</sup>, A. Teymurazyan<sup>44</sup>, A. Tomaradze<sup>42</sup>, A. Tsaris<sup>13</sup>, G. Vasileiadis<sup>2</sup>,  
D. Watts<sup>10</sup>, D. Werthmüller<sup>16</sup>, N. Wickramaarachchi<sup>40</sup>, T. Whitlatch<sup>32</sup>, M. Williams<sup>35</sup>,  
B. Wojtsekhowski<sup>32</sup>, R. L. Workman<sup>15</sup>, T. Xiao<sup>42</sup>, Y. Yang<sup>35</sup>, N. Zachariou<sup>10</sup>, J. Zangl<sup>24</sup>,  
Z. Zhang<sup>53</sup>, B. Zou<sup>8</sup>, J. Zhang<sup>52</sup>, X. Zhou<sup>53</sup>, B. Zihlmann<sup>32</sup>

<sup>1</sup> Arizona State University, Tempe, AZ 85287, USA

<sup>2</sup> National and Kapodistrian University of Athens, Athens 15771, Greece

- <sup>3</sup> Institut für Experimentalphysik I - Ruhr-Universität, Bochum 44780, Germany
- <sup>4</sup> Budker Institute of Nuclear Physics SB RAS, Novosibirsk 630090, Russia
- <sup>5</sup> California State University, Dominguez Hills, Carson, CA 90747, USA
- <sup>6</sup> Carnegie Mellon University, Pittsburgh, PA 15213, USA
- <sup>7</sup> The Catholic University of America, Washington, DC 20064, USA
- <sup>8</sup> Institute of Theoretical Physics CAS, Beijing 100190, People's Republic of China
- <sup>9</sup> University of Connecticut, Storrs, CO 06269, USA
- <sup>10</sup> University of Edinburgh, Edinburgh EH9 3FD, United Kingdom
- <sup>11</sup> Finnish Society of Science and Letters, Helsinki 00130, Finland
- <sup>12</sup> Florida International University, Miami, FL 33199, USA
- <sup>13</sup> Florida State University, Tallahassee, FL 32306, USA
- <sup>14</sup> National Research Centre "Kurchatov Institute", Petersburg Nuclear Physics Institute, Gatchina 188300, Russia
- <sup>15</sup> The George Washington University, Washington, DC 20052, USA
- <sup>16</sup> University of Glasgow, Glasgow G12 8QQ, United Kingdom
- <sup>17</sup> GSI Helmholtzzentrum für Schwerionenforschung GmbH, Darmstadt 64291, Germany
- <sup>18</sup> University of Georgia, Athens, GA 30602, USA
- <sup>19</sup> II. Physikalisches Institut, Justus Liebig-University of Giessen, Giessen 35392, Germany
- <sup>20</sup> Helmholtz-Institut für Strahlen- und Kernphysik, Universität Bonn, Bonn 53115, Germany
- <sup>21</sup> Hampton University, Hampton, VA 23668, USA
- <sup>22</sup> University of Houston, Houston, TX 77204, USA
- <sup>23</sup> Idaho State University, Pocatello, ID 83209, USA
- <sup>24</sup> Indiana University, Bloomington, IN 47403, USA
- <sup>25</sup> I.N.F.N. Sezione di Genova, Genova 16146, Italy
- <sup>26</sup> Institute für Kernphysik & Jülich Center für Hadron Physics, Jülich 52425, Germany
- <sup>27</sup> Kent State University, Kent, OH 44242, USA
- <sup>28</sup> Kyungpook National University, Daegu 702-701, Republic of Korea
- <sup>29</sup> National Research Centre "Kurchatov Institute", Institute for Theoretical and Experimental Physics, Moscow 117218, Russia
- <sup>30</sup> Los Alamos National Laboratory, Los Alamos, NM 87545, USA
- <sup>31</sup> Novosibirsk State University, Novosibirsk 630090, Russia
- <sup>32</sup> Thomas Jefferson National Accelerator Facility, Newport News, VA 23606, USA
- <sup>33</sup> Institute of Theoretical Physics, University of Tübingen, Tübingen 72076, Germany
- <sup>34</sup> University of Massachusetts, Amherst, MA 01003, USA
- <sup>35</sup> Massachusetts Institute of Technology, Cambridge, MA 02139, USA
- <sup>36</sup> Institut für Kernphysik, University of Mainz, Mainz 55099, Germany
- <sup>37</sup> National Research Nuclear University Moscow Engineering Physics Institute, Moscow 115409, Russia
- <sup>38</sup> Norfolk State University, Norfolk, VA 23504, USA
- <sup>39</sup> North Carolina A&T State University, Greensboro, NC 27411, USA
- <sup>40</sup> Old Dominion University, Norfolk, VA 23529, USA
- <sup>41</sup> University of North Carolina at Wilmington, Wilmington, NC 28403, USA
- <sup>42</sup> Northwestern University, Evanston, IL 60208, USA
- <sup>43</sup> Pusan National University, Busan 46241, Republic of Korea
- <sup>44</sup> University of Regina, Regina, SA S4S 0A2, Canada

- <sup>45</sup> Rudjer Bošković Institute, Zagreb 10002, Croatia  
<sup>46</sup> Universidad Técnica Federico Santa María, Casilla 110-V Valparaíso, Chile  
<sup>47</sup> Tomsk State University, Tomsk 634050, Russia  
<sup>48</sup> Tomsk Polytechnic University, Tomsk 634050, Russia  
<sup>49</sup> University of Tuzla, Tuzla 75000, Bosnia and Herzegovina  
<sup>50</sup> Yerevan Physics Institute, Yerevan 0036, Armenia  
<sup>51</sup> College of William and Mary, Williamsburg, VA 23185, USA  
<sup>52</sup> University of Virginia, Charlottesville, VA 22904, USA  
<sup>53</sup> Wuhan University, Wuhan, Hubei 430072, People's Republic of China  
\* Contact Person: mamaryan@odu.edu  
† Spokesperson

(The GLUEX Collaboration)

## Abstract

We propose to create a secondary beam of neutral kaons in Hall D at Jefferson Lab to be used with the GlueX experimental setup for strange hadron spectroscopy. A flux on the order of  $3 \times 10^4$   $K_L$ /s will allow a broad range of measurements to be made by improving the statistics of previous data obtained on hydrogen targets by three orders of magnitude. Use of a deuteron target will provide first measurements on the neutron which is *terra incognita*.

The experiment will measure both differential cross sections and self-analyzed polarizations of the produced  $\Lambda$ ,  $\Sigma$ ,  $\Xi$ , and  $\Omega$  hyperons using the GlueX detector at the Jefferson Lab Hall D. The measurements will span c.m.  $\cos\theta$  from  $-0.95$  to  $0.95$  in the c.m. range above  $W = 1490$  MeV and up to  $3500$  MeV. These new GlueX data will greatly constrain partial-wave analyses and reduce model-dependent uncertainties in the extraction of strange resonance properties (including pole positions), and provide a new benchmark for comparisons with QCD-inspired models and lattice QCD calculations.

The proposed facility will also have an impact in the strange meson sector by providing measurements of the final-state  $K\pi$  system from threshold up to  $2$  GeV invariant mass to establish and improve on the pole positions and widths of all  $K^*(K\pi)$  P-wave states as well as for the S-wave scalar meson  $\kappa(800)$ .



# Contents

|           |   |           |
|-----------|---|-----------|
| <b>1</b>  | <b>Executive Summary</b>  | <b>1</b>  |
| <b>2</b>  | <b>Scope of the Proposal</b>  | <b>2</b>  |
| <b>3</b>  | <b>The Brief Case for Hyperon Spectroscopy</b>                                | <b>4</b>  |
| 3.1       | The $\Lambda(1405) - \Lambda(1520) 1/2^- - 3/2^-$ Doublet . . . . .           | 5         |
| 3.2       | The Low-Lying Positive-Parity Resonances . . . . .                            | 5         |
| 3.3       | The Negative-Parity Hyperon Resonances . . . . .                              | 6         |
| 3.4       | Summary for the Brief Case . . . . .  | 7         |
| <b>4</b>  | <b>Strange Hadrons from the Lattice</b>                                       | <b>7</b>  |
| <b>5</b>  | <b>The Interest of the RHIC/LHC Community in Excited Hyperon Measurements</b> | <b>9</b>  |
| <b>6</b>  | <b>Previous Measurements</b>  | <b>12</b> |
| <b>7</b>  | <b>Phenomenology / Partial-Wave Analysis</b>                                  | <b>13</b> |
| 7.1       | $KN$ and $\bar{K}N$ Final States . . . . .                                    | 14        |
| 7.2       | $\pi\Lambda$ Final States . . . . .   | 16        |
| 7.3       | $\pi\Sigma$ Final States . . . . .  | 16        |
| 7.4       | $K\Xi$ Final States . . . . .   | 19        |
| 7.5       | $KK\Omega$ Final States . . . . .   | 19        |
| 7.6       | Summary for PWA . . . . .   | 19        |
| <b>8</b>  | <b>Theory for "Neutron" Target Measurements</b>                               | <b>20</b> |
| <b>9</b>  | <b>Strange Meson Spectroscopy: <math>K\pi</math> Interaction</b>              | <b>22</b> |
| <b>10</b> | <b>Proposed Measurements</b>  | <b>25</b> |
| 10.1      | $K_L$ Beam in Hall D . . . . .  | 25        |
| 10.1.1    | Compact Photon Source: Conceptual Design . . . . .                            | 26        |
| 10.1.2    | Simulations Study of $K_L$ Beam Production . . . . .                          | 28        |

|           |   |           |
|-----------|---|-----------|
| 10.1.3    | $K_L$ Beam Parameters . . . . .   | 29        |
| 10.1.4    | $K_L$ Beam Background: Gammas, Muons, and Neutrons . . . . .                          | 32        |
| 10.1.5    | $K_L$ Momentum Determination and Beam Resolution . . . . .                            | 34        |
| 10.1.6    | GlueX Detector Time Resolution . . . . .  | 35        |
| 10.1.7    | Measurement of $K_L$ Flux . . . . .   | 37        |
| 10.2      | LH <sub>2</sub> /LD <sub>2</sub> Cryotarget for Neutral Kaon Beam at Hall D . . . . . | 37        |
| <b>11</b> | <b>Running Condition</b>  | <b>39</b> |
| 11.1      | Event Identification, Reconstruction, Acceptances . . . . .                           | 39        |
| 11.1.1    | Simulations and Reconstruction of Various Channels Using GlueX Detector               | 39        |
| 11.1.2    | $K_L p \rightarrow K_S p$ Reaction . . . . .  | 41        |
| 11.1.3    | $K_L p \rightarrow \pi^+ \Lambda$ Reaction . . . . .                                  | 41        |
| 11.1.4    | $K_L p \rightarrow K^+ \Xi^0$ Reaction . . . . .                                      | 44        |
| 11.1.5    | $K_L p \rightarrow K^+ n$ Reaction . . . . .  | 46        |
| 11.1.6    | Reaction $K_L p \rightarrow K^- \pi^+ p$ . . . . .                                    | 48        |
| 11.2      | Summary and Beam Time Request . . . . .   | 50        |
| <b>12</b> | <b>Cover Letter for KLF Proposal Submission to PAC45</b>                              | <b>52</b> |
| <b>13</b> | <b>Appendix A1: Analysis of Three-Body Final States</b>                               | <b>54</b> |
| <b>14</b> | <b>Appendix A2: Determination of Pole Positions</b>                                   | <b>55</b> |
| <b>15</b> | <b>Appendix A3: Statistics Tools for Spectroscopy of Strange Resonances</b>           | <b>58</b> |
| 15.1      | Minimizing Resonance Content . . . . .  | 58        |
| 15.2      | Goodness-of-Fit Tests . . . . .   | 60        |
| 15.3      | Representation of Results . . . . .   | 60        |
| <b>16</b> | <b>Appendix A4: Neutron Background</b>  | <b>60</b> |
| <b>17</b> | <b>Appendix A5: Details of Monte Carlo Study</b>                                      | <b>61</b> |
| 17.1      | Particle Identification . . . . .   | 61        |

|           |   |           |
|-----------|---|-----------|
| 17.1.1    | Details of MC study for $K_{Lp} \rightarrow K_{Sp}$ . . . . .                       | 64        |
| 17.1.2    | Details of MC study for $K_{Lp} \rightarrow \pi^+\Lambda$ . . . . .                 | 64        |
| 17.1.3    | Details of MC study for $K_{Lp} \rightarrow K^+\Xi^0$ . . . . .                     | 67        |
| 17.1.4    | Details of MC study for $K_{Lp} \rightarrow K^+n$ . . . . .                         | 72        |
| <b>18</b> | <b>Appendix A6: Current Hadronic Projects</b>                                       | <b>76</b> |
| 18.1      | Project X, USA . . . . .  | 76        |
| 18.2      | J-PARC, Japan . . . . .   | 76        |
| 18.3      | Belle, Japan . . . . .  | 77        |
| 18.4      | BaBar, USA . . . . .  | 77        |
| 18.5      | $\overline{P}$ ANDA, Germany . . . . .  | 77        |
| 18.6      | COMPASS, CERN . . . . .   | 78        |
| <b>19</b> | <b>Appendix A7: Additional Physics Potential with a <math>K_L</math> Beam</b>       | <b>78</b> |
| <b>20</b> | <b>Appendix A8: List of New Equipment and of Changes in Existing Setup Required</b> | <b>79</b> |
| <b>21</b> | <b>References</b>   | <b>80</b> |

# 1 Executive Summary

We propose to establish a secondary  $K_L$  beam line at JLab Hall D for scattering experiments on both proton and neutron (for the first time) targets in order to determine the differential cross sections and the self-polarization of strange hyperons with the GlueX detector to enable precise partial wave analysis in order to determine all the resonances up to 2400 MeV in the spectra of the  $\Lambda$ ,  $\Sigma$ ,  $\Xi$ , and  $\Omega$  hyperons.

In addition, we intend to do strange meson spectroscopy by studies of the  $\pi - K$  interaction to locate the pole positions in the  $I = 1/2$  and  $3/2$  channels.

The  $K_L$  beam will be generated by directing a high energy, high intensity photon beam onto a Be target in front of the GlueX detector. The flux of the  $K_L$  beam will be of the order  $3 \times 10^4 K_L/s$  on a liquid hydrogen/deuterium cryotarget within the GlueX detector, which has a large acceptance with coverage of both charged and neutral particles. This flux will allow statistics in the case of hydrogen targets to exceed that of earlier experiments by almost three orders of magnitude. The main components of the experimental setup are the compact photon source, the Be target with a beam plug, sweeping magnet and a pair spectrometer.

The physics case for the experiments is aligned with the *2015 Long Range Plan for Nuclear Science* [1]: "...a better understanding of the role of strange quarks became an important priority". Knowledge of the hyperon spectra is an important component for this. The empirical knowledge of the low lying spectra of the  $\Lambda$  and  $\Sigma$  hyperons remains very poor in comparison with that of the nucleon, and in the case of the  $\Xi$  hyperons extremely poor. The structure of these hyperon resonances cannot be understood without empirical determination of their pole positions and decays, which is the goal of the proposed experiments. The determination of the strange hyperon spectra in combination with the current measurements of the spectra of the charm and beauty hyperons at the LHCb experiment at CERN should allow a clear understanding of soft QCD matter and the approach to heavy quark symmetry.

As the first stage of the GlueX program the focus will be on two-body and quasi-two-body: elastic  $K_L p \rightarrow K_S p$  and charge-exchange  $K_L p \rightarrow K^+ n$  reactions, then on two-body reactions producing  $S = -1$  ( $S = -2$ ) hyperons as  $K_L p \rightarrow \pi^+ \Lambda$ ,  $K_L p \rightarrow \pi^+ \Sigma^0$ , and  $K_L p \rightarrow \pi^0 \Sigma^+$  ( $K_L p \rightarrow K^+ \Xi^0$ ), as well as three body  $K_L p \rightarrow K^+ K^+ \Omega^-$ .

For analyzing the data a coupled channel partial wave analysis will be done of the GlueX data in parallel with an analysis of the data from the J-PARC  $K^-$  measurements, when available. The best fit will determine the partial wave amplitudes and the resonance pole positions, residues and Breit-Wigner parameters. These will provide a benchmark for results of forthcoming QCD lattice calculations and lead to the desired understanding of the structure of the strange hyperons.

Our timeline is to begin  $K_L$  beam experiments at the completion of the current GlueX physics program.

## 2 Scope of the Proposal

The nature of QCD confinement continues to provide a challenge to our understanding of soft QCD. Studies of the baryon spectrum provide one obvious avenue to understand this region since the location and properties of excited states reflect the dynamics and relevant degrees-of-freedom of hadrons.

Through analyses of decades worth of data, from both hadronic and electromagnetic (EM) scattering experiments, numerous baryon resonances have been observed, with their masses, widths, and quantum numbers fully determined. There are 109 baryons in the PDG2016 listings but only 58 of them are  $4^*$  or  $3^*$  [2]. Many more states are predicted by quark models (QMs). For example, in the case of  $SU(6) \times O(3)$ , 434 resonances would be required, if all partly revealed multiplets were completed (three 70 and four 56).

Three light quarks can be arranged in six baryonic families,  $N^*$ ,  $\Delta^*$ ,  $\Lambda^*$ ,  $\Sigma^*$ ,  $\Xi^*$ , and  $\Omega^*$ . The possible number of members in a family is not arbitrary [3]. If the  $SU(3)_F$  symmetry of QCD is controlling, then for the octet:  $N^*$ ,  $\Lambda^*$ , and  $\Sigma^*$ , and for the decuplet:  $\Delta^*$ ,  $\Sigma^*$ ,  $\Xi^*$ , and  $\Omega^*$ . The number of experimentally identified resonances in each baryon family in PDG2016 summary tables is 17  $N^*$ , 24  $\Delta^*$ , 14  $\Lambda^*$ , 12  $\Sigma^*$ , 7  $\Xi^*$ , and 2  $\Omega^*$ . Constituent QMs, for instance, predict the existence of no fewer than 64  $N^*$  and 22  $\Delta^*$  states with mass less than 3 GeV. The seriousness of the "missing-states" problem [4] is obvious from these numbers. To complete  $SU(3)_F$  multiplets, one needs no fewer than 17  $\Lambda^*$ s, 41  $\Sigma^*$ s, 41  $\Xi^*$ s, and 24  $\Omega^*$ s.

If these "missing resonances" exist, they have either eluded detection or have produced only weak signals in the existing data sets. The search for such resonances provides a natural motivation for future measurements at Jefferson Lab. As stated in the *2015 Long Range Plan for Nuclear Science* [1]: *For many years, there were both theoretical and experimental reasons to believe that the strange sea-quarks might play a significant role in the nucleon's structure; a better understanding of the role of strange quarks became an important priority.*

Low-lying baryon resonances, both hyperons and non-strange states, are usually considered to be three-quark systems; however, those quarks are constituent, not current ones. This prevents their description by the well-understood perturbative QCD. It seems, however, that some qualitative consequences of perturbative QCD still apply even for the non-perturbative constituent quarks. One of them is the suppression of the effective strong interaction for the heavier strange quark in comparison with the lighter up and down flavored quarks (due to the asymptotic freedom). This is revealed, e.g., in smaller widths of hyperon resonances as compared with similar non-strange baryon resonances. The same phenomenon is seen also for meson resonances (compare the widths of  $K^*$  and  $\rho$  meson resonances). Further investigation of this and other similar properties may help to improve our understanding of the nature of the constituent quarks and other non-perturbative effects.

The JLab 12 GeV energy upgrade, with the new Hall D, is an ideal tool for extensive studies of non-strange and, specifically, strange baryon resonances [5,6]. Our plan is to take advantage of the existing high-quality photon beam line and experimental area in the Hall D complex at Jefferson Lab to deliver a beam of  $K_L$  particles onto a liquid hydrogen/deuterium cryotarget ( $LH_2/LD_2$ )

within the GlueX detector.

The recently constructed GlueX detector in Hall D is a large acceptance spectrometer with good coverage for both charged and neutral particles that can be adapted to this purpose. Obviously, a  $K_L$  beam facility with good momentum resolution is crucial to provide the data needed to identify and characterize the properties of hyperon resonances. The masses and widths of the lowest  $\Lambda$  and  $\Sigma$  baryons were determined mainly with kaon beam experiments in the 1970s [2]. First determinations of the pole position in the complex-energy plane for a hyperon, for instance for the  $\Lambda(1520)3/2^-$ , has been made only recently [7]. An intense  $K_L$  beam would open a new window of opportunity, not only to locate "missing resonances", but also to establish their properties by studying different decay channels systematically.

The recent white paper, dedicated to the physics with meson beams and endorsed by a broad physics community, summarized unresolved issues in hadron physics, and outlined the vast opportunities and advances that only become possible with a "secondary beam facility" [8]. The Hall D GlueX K-long Facility (KLF) measurements will allow studies of very poorly known multiplets of  $\Lambda^*$ ,  $\Sigma^*$ ,  $\Xi^*$ , and even  $\Omega^*$  hyperons with unprecedented statistical precision. These measurements also have the potential to observe dozens of predicted (but heretofore unobserved) states and to establish the quantum numbers of already observed hyperons listed in PDG2016 [2]. Interesting puzzles exist for PDG-listed excited hyperons that do not fit into any of the low-lying excited multiplets, and these need to be further revisited and investigated. Excited  $\Xi$ s, for instance, are very poorly known. Establishing and discovering new states is important, in particular, for determination of the multiplet structure of excited baryons.

We have organized three Workshops: *Physics with Neutral Kaon Beam at JLab* (KL2016) (February 2016) [9], *Excited Hyperons in QCD Thermodynamics at Freeze-Out* (YSTAR2016) (November 2016) [10], and *New Opportunities with High-Intensity Photon Sources* (HIPS2017) (February 2017) [11]. They were dedicated to the physics of hyperons produced by the neutral kaon beam. The KL2016 Workshop [12] followed our LoI-12-15-001 [13] to help address the comments made by PAC43 and to prepare the full proposal for PAC45. The proposed GlueX KLF program is complementary, for instance, to the CLAS12 baryon spectroscopy experiments [14, 15] and would operate in Hall D for several years. The YSTAR2016 Workshop [16] was a successor to the recent KL2016 Workshop and considered the influence of possible "missing" hyperon resonances on QCD thermodynamics, on freeze-out in heavy ion collisions and in the early universe, and in spectroscopy. Finally, the HIPS2017 Workshop [17] aimed at producing an optimized photon source concept with potential increase of scientific output at Jefferson Lab, and at refining the science for hadron physics experiments benefitting from such a high-intensity photon source.

Additionally, the proposed facility will also have a great impact in the strange meson sector by measurements of the final-state  $K\pi$  system from threshold up to 2 GeV in invariant mass to establish and improve on pole positions and widths of all  $K^*(K\pi)$   $P$ -wave states and the  $S$ -wave scalar meson  $\kappa(800)$ . In particular, the  $\kappa(800)$  meson has been under discussion for decades and still remains to be unequivocally confirmed with corresponding quantum numbers by doing detailed phase-shift analysis with high statistics data [18]. A detailed study of the  $K\pi$  system is very important to extract the so-called  $K\pi$  vector and scalar form factors to be compared with  $\tau \rightarrow K\pi\nu_\tau$  decay and can be used to constrain the  $V_{us}$  Cabibbo-Kobayashi-Maskawa (CKM) matrix element

as well as to be used in testing CP violation in decays of heavy  $B$  and  $D$  mesons into  $K\pi\pi$  final states.

The proposal is organized in the following manner. We give an Executive Summary in Sec. 1 and the Scope of the proposal in Sec. 2. Then the Brief Case of Hyperon Spectroscopy is given in Sec. 3 while Hyperons in Lattice studies are presented in Sec. 4. An overview of the Interest of the RHIC/LHC community in Hyperon measurements is summarized in Sec. 5. The short overview of previous bubble chamber measurements is given in Sec. 6. Partial-wave phenomenology is considered in Sec. 7 and Theory for the "Neutron" Target in Sec. 8. A short overview for Strange Meson Spectroscopy is given in Sec. 9. Our Proposed measurements are reported in Sec. 10. It describes a Compact Photon Source,  $K_L$  production and  $K_L$  beam properties, Start Counter Resolution, measurements of  $K_L$  flux, and cryotarget description. Running conditions are described in Sec. 11. Sec. 12 contains a Cover Letter for the KLF proposal submission. The Appendixes contain many technical details for our proposal: Analysis of Three-Body Final States in Appendix A1 13, Determination of Pole Positions in Appendix A2 14, Statistics Tools for Spectroscopy of Strange Resonances in Appendix A3 15, Neutron Background in Appendix A4 16, Details of Monte Carlo Study in Appendix A5 17, Current Hadronic Projects in Appendix A6 18, Additional Physics Potential with a  $K_L$  Beam Appendix in A7 19, and List of New Equipment and of Changes in Existing Setup Required in Appendix A8 20.

### 3 The Brief Case for Hyperon Spectroscopy

Our present experimental knowledge of the strange hyperon spectrum is deplorably incomplete, despite the fact that the ground states of the strange hyperons have been known since the 1960s. In the case of the  $\Lambda$  hyperon resonance spectrum, only the lowest negative-parity doublet is well established even though the structure of these resonances remains under discussion. In the case of the  $\Sigma$  and  $\Xi$  hyperons, only the lowest decuplet resonance states  $\Sigma(1385)$  and  $\Xi(1530)$  are well understood.

The masses of the lowest positive-parity resonances in the spectrum of the  $\Lambda$  and  $\Sigma$  hyperons, the  $\Lambda(1600)$  and  $\Sigma(1660)$  are experimentally known, but their structure is not. In the case of the  $\Xi$  hyperon, the lowest positive-parity resonance remains unobserved.

To settle the nature of the hyperon resonances, their main decay modes have to be determined by experiment. A clear example of how the decay modes can settle the structure of the resonances is provided by the  $\pi$ -decay widths of the decuplets  $\Delta(1232)$ ,  $\Sigma(1385)$ , and  $\Xi(1530)$ . The ratio of these decay widths is 13:4:1, whereas if they were simple three-quark states, with 3, 2, and 1 light quarks each, the ratio should be 9:4:1. A comparison of these ratios indicates that the  $\Sigma(1385)$  and  $\Xi(1530)$  appear to be three-quark states, while the  $\Delta(1232)$  is more complex and formed by a three-quark core with a surrounding meson (or multiquark) cloud. This conclusion is well supported by extensive theoretical calculations [19, 20].



### 3.1 The $\Lambda(1405) - \Lambda(1520) 1/2^- - 3/2^-$ Doublet

In the simplest constituent quark model, the most natural – and the oldest – interpretation, is that the  $\Lambda(1405) - \Lambda(1520) 1/2^- - 3/2^-$  doublet is a low-lying flavor singlet multiplet of three quarks ( $uds$ ). Dynamical versions of this model, with two-body interactions between the quarks can describe the low mean energy of this multiplet, but not the 115 MeV splitting between them. This has led to suggestions that there may even be two different  $1/2^-$  states – one dynamical low  $\bar{K}N$  resonance at 1405 MeV, and an unresolved higher state close to 1520 MeV [21]. If so, it is high time that the "missing"  $1/2^-$  higher-energy state be empirically identified. This problem indicates that the  $\Lambda(1405)$  has a more complex multi-quark structure. This structure is tested in modern theoretical approaches, including constraints from unitarity and chiral symmetry. Confirmed by multiple calculations later on, a two pole structure of  $\Lambda(1405)$  was found in Ref. [22]. The narrow pole lies slightly below  $\bar{K}N$  threshold fixed by the scattering data rather well, see Ref. [23] for the comparison of different modern coupled-channel approaches. However, the position of the second pole is determined less precisely, lying much further below  $\bar{K}N$  threshold and deeper in the complex plane. Recent photoproduction data on  $\pi\Sigma$  by CLAS [24] can be used to reduce the theoretical ambiguity on this (second) pole of  $\Lambda(1405)$  as demonstrated in Ref. [25]. Modern lattice QCD (LQCD) calculations also support the view that its structure is a  $\bar{K}N$  state [26]. In Skyrme's topological soliton model for the baryons, the low-lying  $\Lambda(1405)$  state also appears naturally as a mainly 5-quark state [27, 28]. That model is consistent with QCD in the large color number ( $N_C$ ) limit.

There are similar low-lying flavor-singlet parity doublets in both the charm and bottom hyperon spectra:  $\Lambda_c(2595) - \Lambda_c(2625) 1/2^- - 3/2^-$  and  $\Lambda_b(5912) - \Lambda_b(5920) 1/2^- - 3/2^-$  doublets [2]. The ratio between the  $1/2^- - 3/2^-$  splittings in these three doublets are 8.2:2.1:1, which is not far from the corresponding inverse ratios of the  $K$ ,  $D$ , and  $B$  meson masses: 10.7:2.8:1. The latter is what one should expect from the gradual approach to heavy-quark symmetry with increasing meson (or constituent quark) mass if the quark structure of these three multiplets is similar. This pattern is also consistent with the large  $N_C$  limit of QCD.

### 3.2 The Low-Lying Positive-Parity Resonances

In the spectra of the nucleon and the  $\Lambda$  and  $\Sigma$  hyperons, the lowest positive-parity resonances all lie below the lowest negative-parity multiplets except for the flavor singlet doublet  $\Lambda(1405) - \Lambda(1520) 1/2^- - 3/2^-$ . This reversal of normal ordering cannot be achieved in the constituent quark model with purely color-spin-dependent quark interactions. These low-lying positive-parity resonances are the  $N(1440)$ ,  $\Lambda(1600)$ , and the  $\Sigma(1660) 1/2^+$  states. Their low masses do however appear naturally, if the interactions between the quarks are flavor dependent [29].

Present day LQCD calculations have not yet converged on whether these low-lying states can be described as having a mainly three-quark structure [30]. This may reflect that there is a collective nature in the quark content of all these resonances, which have a low soft vibrational mode. Skyrme's topological soliton model for the baryons, which represents one version of the large  $N_C$  limit of QCD, describes these low-lying states as such vibrational states.



In the spectrum of the  $\Xi$ , the  $\Xi(1690)$  may be such a  $1/2^+$  state as well, although the quantum numbers of that state are yet to be determined.

In the corresponding decuplet spectra, a similar low-lying positive-parity state has so far only been definitely identified in the  $\Delta(1232)$  spectrum: namely, the  $\Delta(1600)3/2^+$ . The  $\Sigma(1840)3/2^+$  resonance very likely represents the corresponding positive-parity  $\Sigma^*$  state. It should be important to identify the corresponding  $3/2^+$  state in the spectrum of the  $\Xi^*$ .

It is of course very probable that corresponding low-lying positive-parity states will be found in the spectra of the  $\Lambda_c$  and  $\Lambda_b$  hyperons, given the fact that they have low-lying negative-parity states akin to those of the  $\Lambda$  hyperon as described above. The experimental identification of those is an important task. Even if the still tentative resonance  $\Lambda_c(2765)$  turns out to be a  $1/2^+$  state, its energy appears to be too high for being the equivalent of the  $\Lambda(1600)$  in the charm hyperon spectrum.

In the spectrum of the  $\Sigma_c$ , the decuplet state  $\Sigma_c(2520)$  is well established. The tentative resonance  $\Sigma_c(2800)$  may, should it turn out to be a  $1/2^+$  state, correspond to the  $\Sigma(1660)$  in the strange hyperon spectrum.

### 3.3 The Negative-Parity Hyperon Resonances

In the spectrum of the nucleon, two well-separated groups of negative-parity resonances appear above the  $1/2^+$  state  $N(1440)$ . In the three-quark model, the symmetry of the lowest energy group is  $[21]_{FS}[21]_F[21]_S$ ; i.e., it has mixed flavor (F) and spin (S) symmetry as well as mixed flavor-spin (FS) symmetry [29, 31]. This group consists of the  $N(1535)1/2^-$  and the  $N(1520)3/2^-$  resonances. There is a direct correspondence in the  $\Lambda(1670)1/2^-$  and the  $\Lambda(1690)3/2^-$  resonances. There is also a repeat of this group in the spectrum of the  $\Sigma$  hyperon in the two resonances  $\Sigma(1620)1/2^-$  (tentative) and  $\Sigma(1670)3/2^-$ .

These spin  $1/2^-$  and  $3/2^-$  states in the spectrum of the nucleon have intriguing decay patterns. The  $N(1535)$  resonance has a large (32-52%) decay branch to  $\eta N$ , even though its energy lies very close to the  $\eta N$  threshold. This pattern repeats in the case of the  $\Lambda(1670)$ , which also has a substantial (10-25%) decay branch to the corresponding  $\eta\Lambda$  state, even though it lies even closer to the threshold for that decay. As the still uncertain  $\Sigma(1620)1/2^-$  resonance is located almost exactly at the threshold for  $\eta\Sigma$ , there is naturally no signal for an  $\eta\Sigma$  decay from it. The ratio of the  $\eta$  decay widths of the  $N(1535)$  and the  $\Lambda(1670)$  is about 6:1, which suggests that the  $\eta$  decay might involve a pair of quarks rather than a single constituent quark as in the  $\pi$  decay of the decuplet resonances.

In the spectrum of the  $\Xi$  hyperon, none of the negative-parity multiplets is complete. The state  $\Xi(1820)3/2^-$  may be the analog in the  $\Xi$  spectrum of the states  $N(1520)$ ,  $\Lambda(1670)$ , and  $\Sigma(1670)$ . It should be important to identify the lowest  $1/2^-$  resonance in the  $\Xi$  spectrum. If that resonance lacks an  $\eta$  decay branch, it would demonstrate that the  $\eta$  decay of the  $1/2^-$  resonances in the spectra of the nucleon,  $\Lambda$  and  $\Sigma$  involves two quarks.

It should also be important to determine whether the uncertain "bumps" referred to in the Particle Data Tables labelled  $\Sigma(1480)$ ,  $\Sigma(1560)$ , and  $\Xi(1620)$  represent true resonances.

About 120 MeV above the  $1/2^- - 3/2^-$  pair of nucleon resonances  $N(1535)$  and  $N(1520)$ , the nucleon spectrum has three negative-parity resonances close in energy to one another. This multiplet is formed of the  $N(1650)1/2^-$ ,  $N(1700)3/2^-$ , and  $N(1675)5/2^-$  resonances. In the three-quark model the symmetry configuration of these states are  $[21]_{FS}[21]_F[21]_S$ ; i.e., their spin configuration is completely symmetric.

The analogs in the spectrum of the  $\Lambda$  of the first and last of these nucleon resonances are the  $\Lambda(1800)1/2^-$  and the  $\Lambda(1830)5/2^-$  resonances. This correspondence remains uncertain, however, because the missing  $3/2^-$  state in this  $\Lambda$  resonance multiplet has not yet been identified.

A common feature of all the  $1/2^-$  resonances in these multiplets is their substantial  $\eta$  decay branches.

Our present knowledge of the spectrum of the  $\Xi$  hyperons remains too incomplete to identify any member of the negative-parity multiplet with the symmetry structure  $[21]_{FS}[21]_F[21]_S$ .

### 3.4 Summary for the Brief Case

This overview shows that the present empirical knowledge of the spectrum of the strange hyperons remains remarkably incomplete. As a consequence, the quark structure of even the lowest-energy resonances remains uncertain. Only an experimental determination of the lowest-energy positive- and negative-parity hyperon resonances and their decay branches would settle the main open issues.

In the spectrum of the  $\Lambda$  hyperon, there remains a question of the existence of a  $1/2^-$  partner to the  $\Lambda(1520)3/2^-$  resonance. In addition, it should be important to search for the missing  $3/2^-$   $\Lambda$  resonance near 1700 MeV. Equally important would be the search for the apparently "missing"  $3/2^-$  state near 1750 MeV in the spectrum of the  $\Sigma$  hyperon.

Our present knowledge of the spectrum of the  $\Sigma$  hyperons remains too incomplete to identify any member of the corresponding negative-parity multiplet formed of  $1/2^-$ ,  $3/2^-$ , and  $5/2^-$  resonances.

It should also be important to determine, whether the uncertain "bumps" referred to in the Particle Data Tables labelled  $\Sigma(1480)$ ,  $\Sigma(1560)$ , and  $\Sigma(1620)$  represent true resonances [2].

## 4 Strange Hadrons from the Lattice

Our knowledge of the excited-state spectrum of QCD through the solution of the theory on a Euclidean space-time lattice has undergone tremendous advances over the past several years. What we characterize as excited states are resonances that are unstable under the strong interaction, and their properties are encapsulated in momentum-dependent scattering amplitudes. The means of calculating such momentum-dependent phase shifts for elastic scattering on a Euclidean lattice at finite volume was provided many years ago [32] and extended to systems in motion [33], but its implementation for QCD remained computationally elusive until recently. A combination of theoretical, algorithmic, and computational advances has changed this situation dramatically, notably

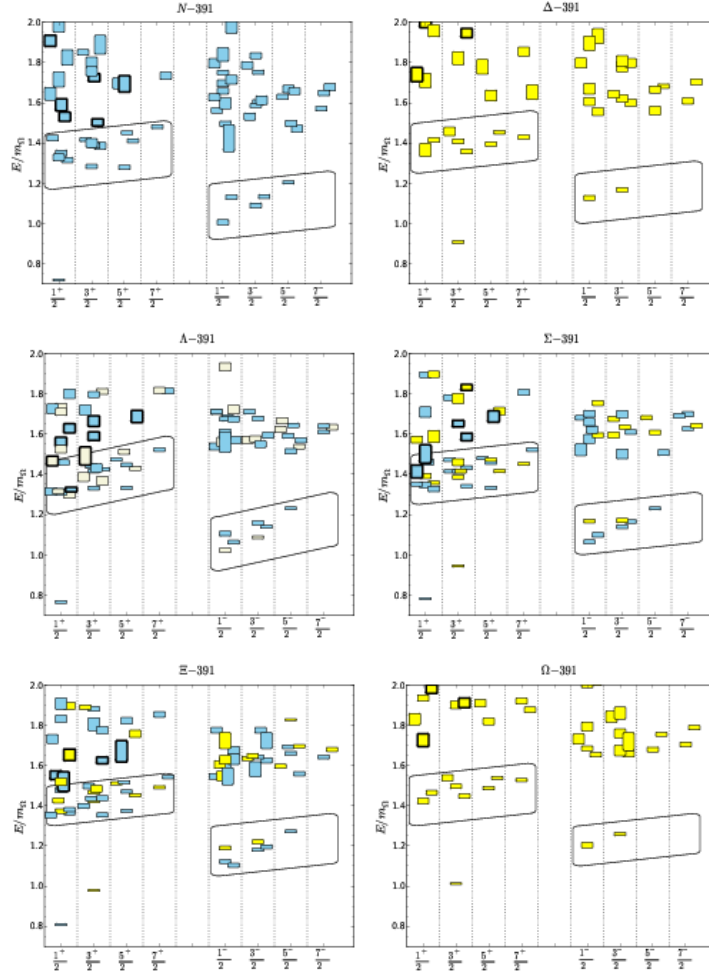


Figure 1: Results for baryon excited states using an ensemble with  $m_\pi = 391$  MeV are shown versus  $J^P$  [52]. Colors are used to display the flavor symmetry of dominant operators as follows: blue for  $8_F$  in  $N$ ,  $\Lambda$ ,  $\Sigma$ , and  $\Xi$ ; beige for  $1_F$  for  $\Lambda$ ; yellow for  $10_F$  in  $\Delta$ ,  $\Sigma$ ,  $\Xi$ , and  $\Omega$ . The lowest bands of positive- and negative-parity states are highlighted within slanted boxes. Hybrid states, in which the gluons play a substantive role, are shown for positive parity by symbols with thick borders.

in the case of mesons. There have been several lattice calculations of the momentum-dependent phase shift of the  $\rho$  mesons [34–40]. More recently, the formulation to extract amplitude information has been extended to the coupled-channel case [41–45], and applied to the case of the coupled  $K\bar{K} - \pi\pi$  [46] system describing the  $\rho$  resonance, and to the  $\eta K - \eta\pi$  [47,48].

The application to baryons is far more limited but, nonetheless, important insights have been gained. In an approach in which the excited-state hadrons are treated as stable particles, a spectrum of baryons at least as rich as that of the quark model is revealed [49, 50], and evidence has been presented for "hybrid" baryon states, beyond those of the quark model, in which gluon degrees of freedom are essential [51]. Notably, this picture extends to the spectrum of  $\Lambda$ ,  $\Sigma$ ,  $\Xi$ , and  $\Omega$  states where the counting of states reflects  $SU(6) \times O(3)$  symmetry, and the presence of hybrids is common across the spectrum. As indicated above, these calculations are incomplete in that the momentum-dependent scattering amplitudes remain to be extracted. In Fig. 1, baryon spectra from [52] are presented in units of  $\Omega$  mass from LQCD calculations with ensemble  $m_\pi = 391$  MeV (not yet at physical  $m_\pi$ ). However, in comparison with the case of mesons cited above, the challenges are more computational than theoretical or conceptual, and the progress made in the meson sector will be reflected for the case of baryons in the coming years.

## 5 The Interest of the RHIC/LHC Community in Excited Hyperon Measurements

The relativistic heavy-ion community at RHIC and the LHC has recently embarked on specific analyses to address the issue of strangeness hadronization. LQCD calculations in the QCD crossover transition region between a deconfined phase of quark and gluons and a hadronic resonance gas have revealed a potentially interesting sub-structure related to the hadronization process. Studies of flavor-dependent susceptibilities, which can be equated to experimental measurements of conserved quantum-number fluctuations, seem to indicate a slight flavor hierarchy in the three-quark sector (u,d,s) in thermalized systems. Specifically, the ratios of higher-order susceptibilities in the strange sector show a higher transition temperature than in the light sector [53]. Both pseudo-critical temperatures are still within the error bars of the quoted transition temperature based on all LQCD order parameters [54,55], which is  $154 \pm 9$  MeV, but the difference of the specific susceptibilities is around 18 MeV and well outside their individual uncertainties.

This difference seems to be confirmed by statistical thermal-model calculations that try to describe the yields of emitted hadrons from a QGP based on a common chemical freeze-out temperature. Although the yields measured by ALICE at the LHC in 2.76 TeV PbPb collisions can be described by a common temperature of  $156 \pm 2$  MeV, with a reasonable  $\chi^2$ , the fit improves markedly if one allows the light quark baryons to have a lower temperature than the strange quark baryons [56]. A similar result has been found when the thermal fluctuations of particle yields as measured by STAR Collaboration [57, 58], which can be related to the light quark dominated susceptibilities of the electric charge and the baryon number on the lattice, have been compared to statistical model calculations [59].

If one assumes that strange and light quarks indeed prefer different freeze-out temperatures, then

the question arises how this could impact the hadronization mechanism and abundance of specific hadronic species. In other words, is the production of strange particles, in particular excited resonant states, enhanced in a particular temperature range in the crossover region? Strange ground-state particle production shows evidence of enhancement, but the most likely scenario is that the increased strange quark abundance will populate excited states; therefore, the emphasis of any future experimental program trying to understand hadron production is shifting towards strange baryonic resonance production. Furthermore, recent LHC measurements in small systems, down to elementary proton-proton collisions, have revealed that even in these small systems there is evidence for deconfinement, if the achieved energy density, documented by the measured charged particle multiplicity is large enough [60]. Therefore, future measurements of elementary collisions in the K-Long Facility experiment at JLab might well provide the necessary link to future analysis of strange resonance enhancements in heavy-ion collisions at RHIC and the LHC and a deeper understanding of the hadronization process.

This statement is also supported by comparisons between the aforementioned LQCD calculations and model predictions based on a non-interacting hadronic resonance gas. The Hadron Resonance Gas (HRG) model [61–64] yields a good description of most thermodynamic quantities in the hadronic phase up to the pseudo-critical temperature. The idea that strongly interacting matter in the ground state can be described in terms of a non-interacting gas of hadrons and resonances, which effectively mimics the interactions of hadrons by simply increasing the number of possible resonant states exponentially as a function of temperature, was proposed early on by Hagedorn [65]. The only input to the model is the hadronic spectrum: usually it includes all well-known hadrons in the *Review of Particle Physics* (RPP), namely the ones rated with at least two stars. Recently, it has been noticed that some more differential observables present a discrepancy between lattice and HRG model results. The inclusion of not-yet-detected states, such as the ones predicted by the original Quark Model (QM) [66, 67] has been proposed to improve the agreement [68, 69]. A systematic study based on a breakdown of contributions to the thermodynamic pressure given by particles grouped according to their quantum numbers (in particular baryon number and strangeness) enables us to infer in which hadron sector more states are needed compared to the well-known ones from the RPP [70]. In case of a flavor hierarchy in the transition region one would expect the number of strange resonances to increase, due to a higher freeze-out temperature, compared to the number of light-quark resonances. Figure 2 shows the effect of different strange hadron input spectra to the HRG model in comparison to LQCD. Figure 2(upper plot) shows the number of states in PDG-2016 [2], PDG-2016+ (including one star states), the standard QM, and a Quark Model with enhanced quark interactions in the hadron (hyper-central model hQM [71]). Fig. 2(lower plot) shows a comparison of the HRG results to a leading-order LQCD calculation of  $\mu_s/\mu_B$ ; i.e., the ratio to strange to baryon number susceptibility [70].

An interesting conclusion that arises from these studies is that the improvement in the listing of strange resonances between PDG-2008 [72] and PDG-2016 definitely brought the HRG calculations closer to the LQCD data. By looking at details in the remaining discrepancy, which is in part remedied by including one-star rated resonances in PDG-2016, it seems that the effect is more carried by singly strange resonances rather than multi-strange resonances, also in light of comparisons to quark models that include di-quark structures [73] or enhanced quark interactions in the baryon (hypercentral models [71]). This is good news for the experiments since the  $\Lambda$  and  $\Sigma$  reso-

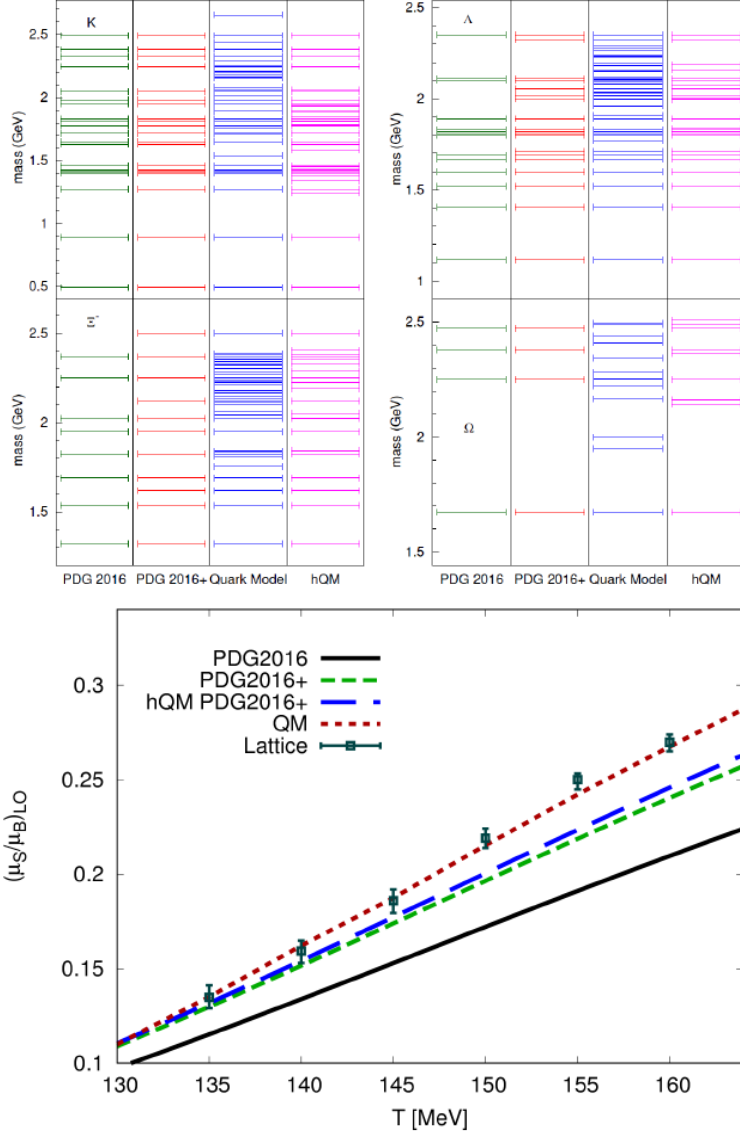


Figure 2: Upper plot: Comparison of predicted and measured excited strange hadronic states in PDG-2016, PDG-2016+ (including one star states), QM, and hQM. Lower plot: Lattice QCD calculation of the temperature dependence of the leading order susceptibility ratio  $(\mu_s/\mu_B)$  compared to results from HRG model calculations with varying number of hadronic states.

nances below  $2 \text{ GeV}/c^2$  are well within reach of the KLF experiment and, to a lesser significance, the RHIC/LHC experiments. In this context it is also important to point out that the use of both hydrogen and deuterium targets in KLF is crucial since it will enable the measurement of charged and neutral hyperons. A complete spectrum of singly strange hyperon states is necessary to make a solid comparison to first-principle calculations.

In summary: Any comparisons between experimentally verified strange quark-model states from YSTAR and LQCD will shed light on a multitude of interesting questions relating to hadronization in the non-perturbative regime, exotic particle production, the interaction between quarks in

baryons and a possible flavor hierarchy in the creation of confined matter.

## 6 Previous Measurements

While a formally complete experiment requires the measurement, at each energy,  $W$ , and angle,  $\theta$ , of at least three independent observables, the current database for  $K_{LP} \rightarrow \pi Y$  and  $KY$  is populated mainly by unpolarized cross sections. Figure 3 illustrates this quite clearly.

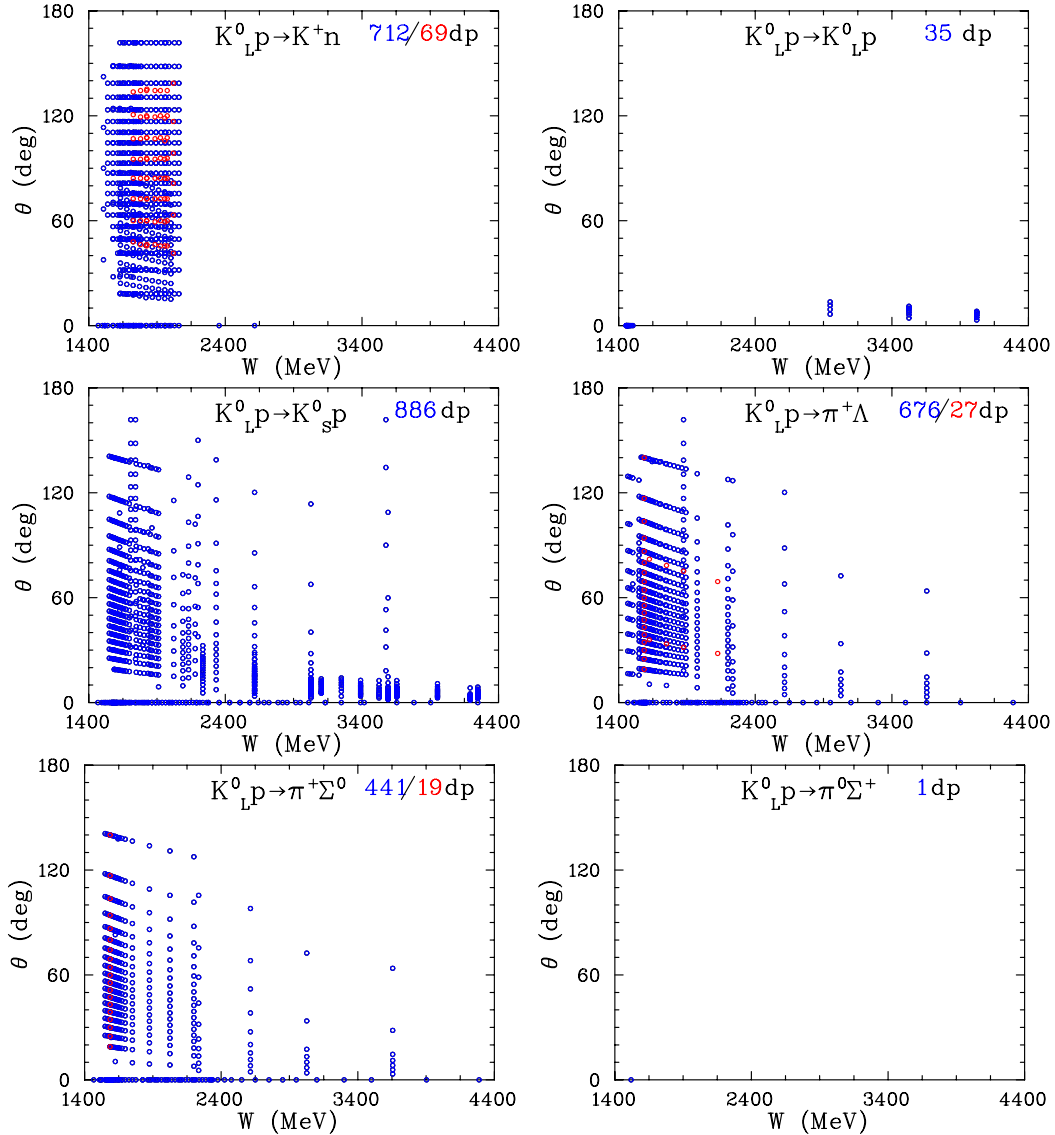


Figure 3: Experimental data available for  $K_{LP} \rightarrow K^+ n$ ,  $K_{LP} \rightarrow K_{LP}$ ,  $K_{LP} \rightarrow K_{Sp}$ ,  $K_{LP} \rightarrow \pi^+ \Lambda$ ,  $K_{LP} \rightarrow \pi^+ \Sigma^0$ , and  $K_{LP} \rightarrow \pi^0 \Sigma^+$  as a function of c.m. energy  $W$  [74]. The number of data points (dp) is given in the upper righthand side of each subplot [blue (red) shows amount of unpolarized (polarized) observables]. Total cross sections are plotted at zero degrees.



The initial studies of the KLF program at GlueX will likely focus on two-body and quasi-two-body processes: elastic  $K_{LP} \rightarrow K_{SP}$  and charge-exchange  $K_{LP} \rightarrow K^+n$  reactions, then two-body reactions producing  $S = -1$  ( $S = -2$ ) hyperons as  $K_{LP} \rightarrow \pi^+\Lambda$ ,  $K_{LP} \rightarrow \pi^+\Sigma^0$ , and  $K_{LP} \rightarrow \pi^0\Sigma^+$  ( $K_{LP} \rightarrow K^+\Xi^0$ ). Most of the previous measurements induced by a  $K_L$  beam, were collected for  $W = 1454$  MeV and with some data up to  $W = 5054$  MeV. Experiments were performed between 1961 and 1982 with mostly hydrogen bubble chambers at ANL, BNL, CERN, DESY, KEK, LRL, NIMROD, NINA, PPA, and SLAC. Note that some of data were taken at EM facilities at NINA [75] (a short overview about NINA experiments is given by Albrow recently [76]) and SLAC [77]. The goal of the Manchester University group that worked at the Daresbury 5-GeV electron synchrotron NINA was CP-violation, which was a hot topic back to the mid 1960s. The main physics topics that the SLAC group addressed were studies of the systematics for particle/anti-particle processes through the intrinsic properties of the K-longs.

The first paper that discussed the possibility of creating a practical neutral kaon beam at an electron synchrotron through photoproduction was an optimistic prediction for SLAC by Drell and Jacob in 1965 [78]. With significant developments in technology, high-quality EM facilities, such as JLab [13], are now able to realize a complete hyperon spectroscopy program.

The overall systematics of previous  $K_{LP}$  experiments varies between 15% and 35%, and the energy binning is much broader than hyperon widths. The previous number of  $K_L$ -induced measurements (2426  $d\sigma/d\Omega$ , 348  $\sigma^{tot}$ , and 115  $P$  observables) [74] was very limited. Additionally, we are not aware of any measurements on a "neutron" target.

Our knowledge about the non-strange sector is more advanced vs. the strange one [2]. For the non-strange case, for instance, phenomenology has access to 51k data of  $\pi N \rightarrow \pi N$  and 39k data of  $\gamma N \rightarrow \pi N$  below  $W = 2.5$  GeV [79].

## 7 Phenomenology / Partial-Wave Analysis

Here, we summarize some of the physics issues involved with such processes. Following Ref. [80], the differential cross section and polarization for  $K_{LP}$  scattering are given by

$$\frac{d\sigma}{d\Omega} = \lambda^2(|f|^2 + |g|^2), \quad (1)$$

$$P \frac{d\sigma}{d\Omega} = 2\lambda^2 \text{Im}(fg^*), \quad (2)$$

where  $\lambda = \hbar/k$ , with  $k$  the magnitude of c.m. momentum for the incoming meson. Here  $f = f(W, \theta)$  and  $g = g(W, \theta)$  are the usual spin-nonflip and spin-flip amplitudes at c.m. energy  $W$  and meson c.m. scattering angle  $\theta$ . In terms of partial waves,  $f$  and  $g$  can be expanded as

$$f(W, \theta) = \sum_{l=0}^{\infty} [(l+1)T_{l+} + lT_{l-}] P_l(\cos \theta), \quad (3)$$

$$g(W, \theta) = \sum_{l=1}^{\infty} [T_{l+} - T_{l-}] P_l^1(\cos \theta), \quad (4)$$



where  $l$  is the initial orbital angular momentum,  $P_l(\cos \theta)$  is a Legendre polynomial, and  $P_l^1(\cos \theta)$  is an associated Legendre function. The total angular momentum for the amplitude  $T_{l+}$  is  $J = l + \frac{1}{2}$ , while that for the amplitude  $T_{l-}$  is  $J = l - \frac{1}{2}$ . For hadronic scattering reactions, we may ignore small CP-violating terms and write

$$K_L = \frac{1}{\sqrt{2}}(K^0 - \bar{K}^0), \quad (5)$$

$$K_S = \frac{1}{\sqrt{2}}(K^0 + \bar{K}^0). \quad (6)$$

We may generally have both  $I = 0$  and  $I = 1$  amplitudes for  $KN$  and  $\bar{K}N$  scattering, so that the amplitudes  $T_{l\pm}$  can be expanded in terms of isospin amplitudes as

$$T_{l\pm} = C_0 T_{l\pm}^0 + C_1 T_{l\pm}^1, \quad (7)$$

where  $T_{l\pm}^I$  are partial-wave amplitudes with isospin  $I$  and total angular momentum  $J = l \pm \frac{1}{2}$ , with  $C_I$  the appropriate isospin Clebsch-Gordon coefficients.

We plan to do a coupled-channel partial-wave analysis (PWA) with new GlueX data in combination with available new J-PARC  $K^-$  measurements when they will come. Then the best fit will allow determine model-independent (data-driven) partial-wave amplitudes and associated resonance parameters (pole positions, residues, Breit-Wigner (BW) parameters, etc.) as the SAID group does, for instance, for the analysis of  $\pi N$ -elastic, charge-exchange, and  $\pi^- p \rightarrow \eta n$  data [81].

## 7.1 $KN$ and $\bar{K}N$ Final States

The amplitudes for reactions leading to  $KN$  and  $\bar{K}N$  final states are

$$T(K^- p \rightarrow K^- p) = \frac{1}{2}T^1(\bar{K}N \rightarrow \bar{K}N) + \frac{1}{2}T^0(\bar{K}N \rightarrow \bar{K}N), \quad (8)$$

$$T(K^- p \rightarrow \bar{K}^0 n) = \frac{1}{2}T^1(\bar{K}N \rightarrow \bar{K}N) - \frac{1}{2}T^0(\bar{K}N \rightarrow \bar{K}N), \quad (9)$$

$$T(K^+ p \rightarrow K^+ p) = T^1(KN \rightarrow KN), \quad (10)$$

$$T(K^+ n \rightarrow K^+ n) = \frac{1}{2}T^1(KN \rightarrow KN) + \frac{1}{2}T^0(KN \rightarrow KN), \quad (11)$$

$$T(K_{LP} \rightarrow K_{SP}) = \frac{1}{2} \left( \frac{1}{2}T^1(KN \rightarrow KN) + \frac{1}{2}T^0(KN \rightarrow KN) \right) - \frac{1}{2}T^1(\bar{K}N \rightarrow \bar{K}N), \quad (12)$$

$$T(K_{LP} \rightarrow K_{LP}) = \frac{1}{2} \left( \frac{1}{2}T^1(KN \rightarrow KN) + \frac{1}{2}T^0(KN \rightarrow KN) \right) + \frac{1}{2}T^1(\bar{K}N \rightarrow \bar{K}N), \quad (13)$$

$$T(K_{LP} \rightarrow K^+ n) = \frac{1}{\sqrt{2}} \left( \frac{1}{2}T^1(KN \rightarrow KN) - \frac{1}{2}T^0(KN \rightarrow KN) \right). \quad (14)$$

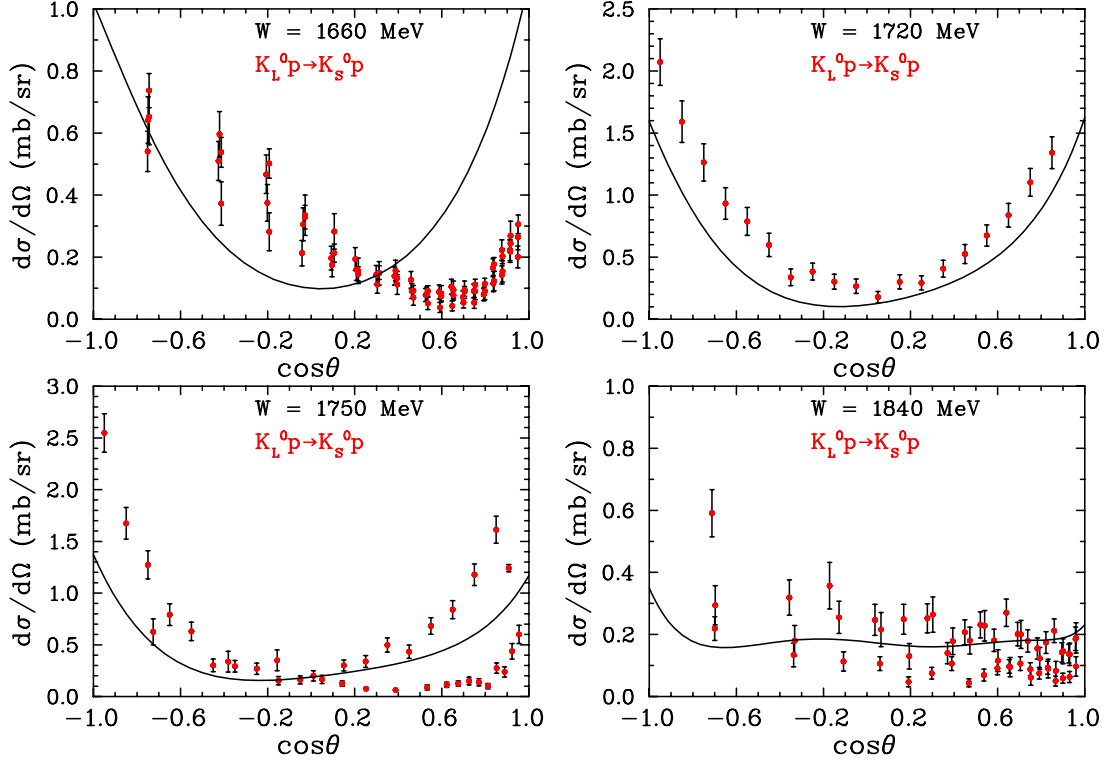


Figure 4: Selected differential cross section data for  $K_L p \rightarrow K_S p$  at  $W = 1660$  MeV, 1720 MeV, 1750 MeV, and 1840 MeV, from Ref. [82]. The plotted points from previously published experimental data are those data points within 20 MeV of the kaon c.m. energy indicated on each panel [79]. Plotted uncertainties are statistical only. The curves are predictions using amplitudes from a recent PWA of  $\bar{K}N \rightarrow \bar{K}N$  data [83,84], combined with  $KN \rightarrow KN$  amplitudes from the SAID database [79].

No differential cross-section data are available for  $K_{LP} \rightarrow K_{LP}$  below  $W \sim 2948$  MeV. A fair amount of data are available for the reaction,  $K^+n \rightarrow K^0p$ , measured on a deuterium target. Figure 4 shows a sample of available differential cross sections for  $K_{LP} \rightarrow K_{SP}$  compared with predictions determined from a recent PWA of  $\bar{K}N \rightarrow \bar{K}N$  data [83, 84], combined with  $KN \rightarrow KN$  amplitudes from the SAID database [79]. The predictions at lower and higher energies tend to agree less well with the data.

## 7.2 $\pi\Lambda$ Final States

The amplitudes for reactions leading to  $\pi\Lambda$  final states are

$$T(K^-p \rightarrow \pi^0\Lambda) = \frac{1}{\sqrt{2}}T^1(\bar{K}N \rightarrow \pi\Lambda), \quad (15)$$

$$T(K_{LP} \rightarrow \pi^+\Lambda) = -\frac{1}{\sqrt{2}}T^1(\bar{K}N \rightarrow \pi\Lambda). \quad (16)$$

The  $K^-p \rightarrow \pi^0\Lambda$  and  $K_{LP} \rightarrow \pi^+\Lambda$  amplitudes imply that observables for these reactions measured at the same energy should be the same except for small differences due to the isospin-violating mass differences in the hadrons. No differential cross-section data for  $K^-p \rightarrow \pi^0\Lambda$  are available at c.m. energies  $W < 1540$  MeV, although data for  $K_{LP} \rightarrow \pi^+\Lambda$  are available at such energies. At 1540 MeV and higher energies, differential cross-section and polarization data for the two reactions are in fair agreement, as shown in Figs. 5 and 6.

## 7.3 $\pi\Sigma$ Final States

$SU(3)$  flavor symmetry allows as many  $S = -2$  baryon resonances as there are  $N$  and  $\Delta$  resonances combined ( $\sim 27$ ); however, until now only three states,  $\Xi(1322)1/2^+$ ,  $\Xi(1530)3/2^+$ , and  $\Xi(1820)3/2^-$ , have their quantum numbers assigned and only a few more states have been observed [2].

The amplitudes for reactions leading to  $\pi\Sigma$  final states are

$$T(K^-p \rightarrow \pi^-\Sigma^+) = -\frac{1}{2}T^1(\bar{K}N \rightarrow \pi\Sigma) - \frac{1}{\sqrt{6}}T^0(\bar{K}N \rightarrow \pi\Sigma), \quad (17)$$

$$T(K^-p \rightarrow \pi^+\Sigma^-) = \frac{1}{2}T^1(\bar{K}N \rightarrow \pi\Sigma) - \frac{1}{\sqrt{6}}T^0(\bar{K}N \rightarrow \pi\Sigma), \quad (18)$$

$$T(K^-p \rightarrow \pi^0\Sigma^0) = \frac{1}{\sqrt{6}}T^0(\bar{K}N \rightarrow \pi\Sigma), \quad (19)$$

$$T(K_{LP}^0 \rightarrow \pi^+\Sigma^0) = -\frac{1}{2}T^1(\bar{K}N \rightarrow \pi\Sigma), \quad (20)$$

$$T(K_{LP}^0 \rightarrow \pi^0\Sigma^+) = \frac{1}{2}T^1(\bar{K}N \rightarrow \pi\Sigma). \quad (21)$$

Figure 7 shows a comparison of differential cross-section data for  $K^-p$  and  $K_{LP}$  reactions leading to  $\pi\Sigma$  final states at  $W = 1660$  MeV (or  $P_{\text{lab}} = 716$  MeV/c). The curves are based on energy-

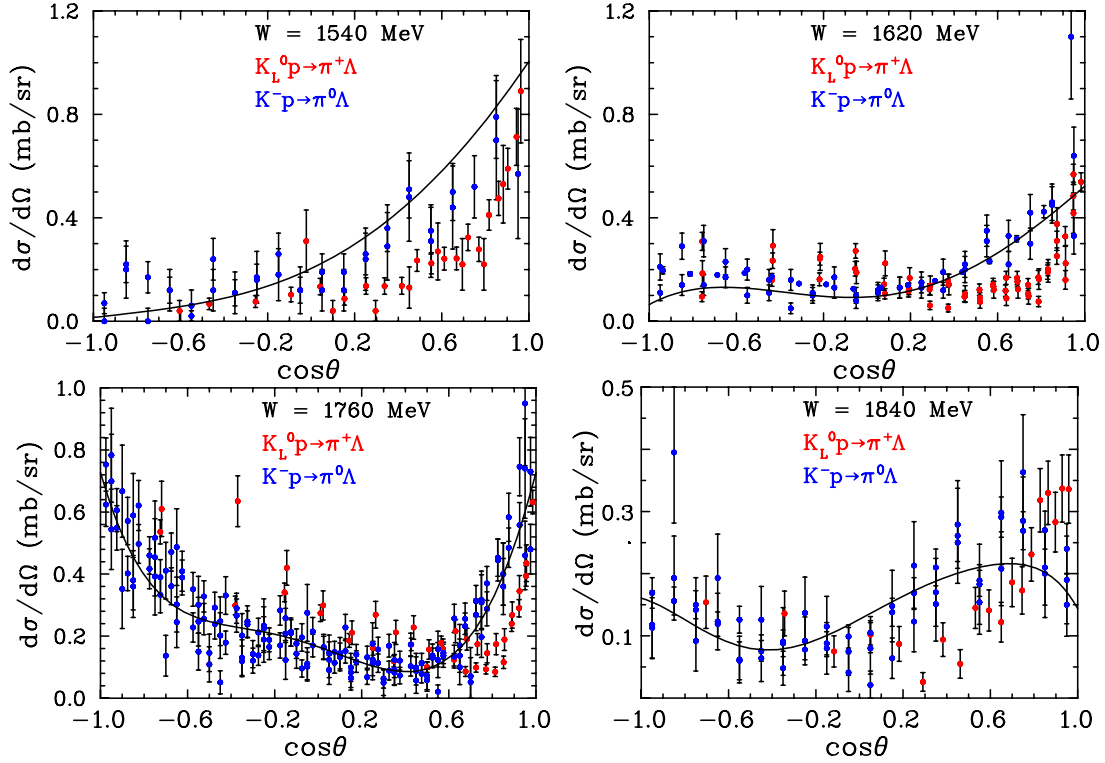


Figure 5: Comparison of selected differential cross section data for  $K^-p \rightarrow \pi^0\Lambda$  and  $K_L p \rightarrow \pi^+\Lambda$  at  $W = 1540$  MeV,  $1620$  MeV,  $1760$  MeV, and  $1840$  MeV, from Ref. [82]. The plotted points from previously published experimental data are those data points within 20 MeV of the kaon c.m. energy indicated on each panel [79]. Plotted uncertainties are statistical only. The curves are from a recent PWA of  $K^-p \rightarrow \pi^0\Lambda$  data [83, 84].

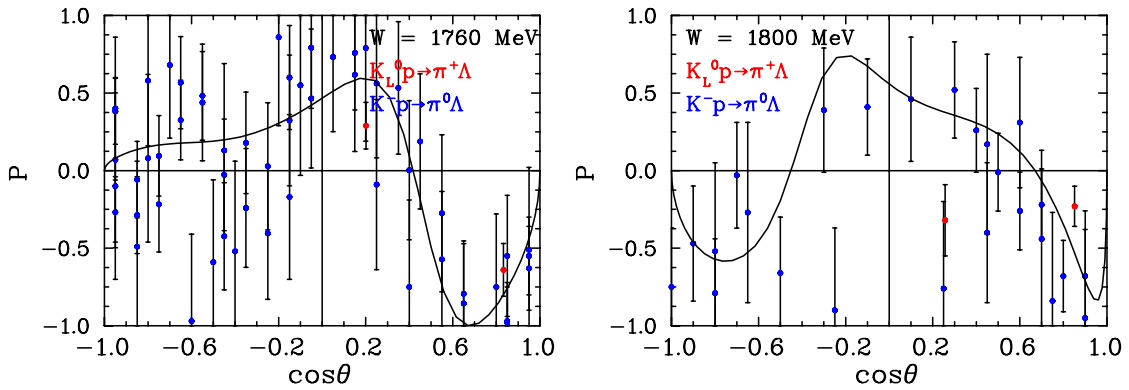


Figure 6: Comparison of selected polarization data for  $K^-p \rightarrow \pi^0\Lambda$  and  $K_L p \rightarrow \pi^+\Lambda$  at  $W = 1760$  MeV and  $1880$  MeV, from Ref. [82]. The plotted points from previously published experimental data are those data points within 20 MeV of the kaon c.m. energy indicated on each panel [79]. The curves are from a recent PWA of  $K^-p \rightarrow \pi^0\Lambda$  data [83, 84].

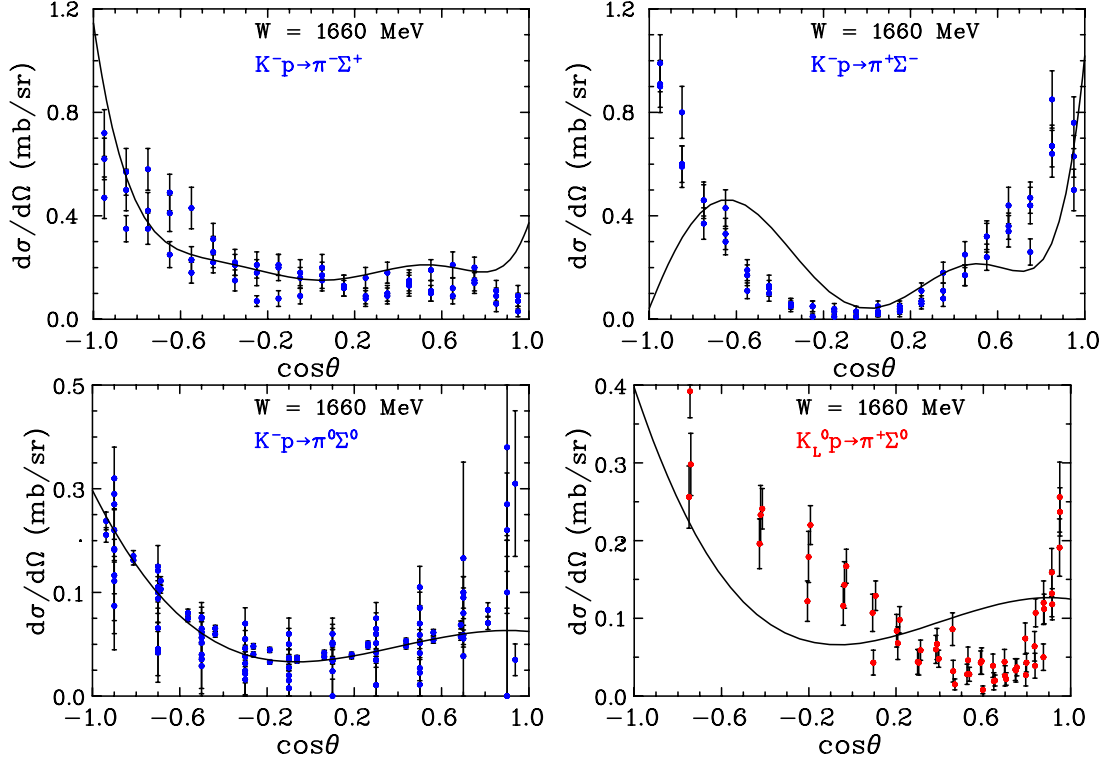


Figure 7: Comparison of selected differential cross-section data for  $K^-p \rightarrow \pi^-\Sigma^+$ ,  $K^-p \rightarrow \pi^+\Sigma^-$ ,  $K^-p \rightarrow \pi^0\Sigma^0$ , and  $K_L p \rightarrow \pi^0\Sigma^+$  at  $W = 1660$  MeV, from Ref. [82]. The plotted points from previously published experimental data are those data points within 20 MeV of the kaon c.m. energy indicated on each panel [79] The curves are from a recent PWA of  $K^-p \rightarrow \pi\Sigma$  data [83, 84].

dependent isospin amplitudes from a recent PWA [83, 84]. No differential cross-section data are available for  $K_L p \rightarrow \pi^0\Sigma^+$ . As this example shows, the quality of the  $K_L p$  data is comparable to that for the  $K^-p$  data. It would, therefore, be advantageous to combine the  $K_L p$  data in a new coupled-channel PWA with available  $K^-p$  data. Note that the reactions  $K_L p \rightarrow \pi^+\Sigma^0$  and  $K_L p \rightarrow \pi^0\Sigma^+$  are isospin selective (only  $I = 1$  amplitudes are involved) whereas the reactions  $K^-p \rightarrow \pi^-\Sigma^+$  and  $K^-p \rightarrow \pi^+\Sigma^-$  are not. New measurements with a  $K_L$  beam would lead to a better understanding of  $\Sigma^*$  states and would help constrain the amplitudes for  $K^-p$  scattering to  $\pi\Sigma$  final states

## 7.4 $K\Xi$ Final States

The amplitudes for reactions leading to  $K\Xi$  final states are

$$T(K^-p \rightarrow K^0\Xi^0) = \frac{1}{2}T^1(\bar{K}N \rightarrow K\Xi) + \frac{1}{2}T^0(\bar{K}N \rightarrow K\Xi), \quad (22)$$

$$T(K^-p \rightarrow K^+\Xi^-) = \frac{1}{2}T^1(\bar{K}N \rightarrow K\Xi) - \frac{1}{2}T^0(\bar{K}N \rightarrow K\Xi), \quad (23)$$

$$T(K_Lp \rightarrow K^+\Xi^0) = -\frac{1}{\sqrt{2}}T^1(\bar{K}N \rightarrow K\Xi). \quad (24)$$

The threshold for  $K^-p$  and  $K_Lp$  reactions leading to  $K\Xi$  final states is fairly high ( $W_{\text{thresh}} = 1816$  MeV). In Fig. 8(left), we present the cross section for  $\Xi$  production using a  $K^-$ -beam [85]. There are no differential cross-section data available for  $K_Lp \rightarrow K^+\Xi^0$  and very few (none recent) for  $K^-p \rightarrow K^0\Xi^0$  or  $K^-p \rightarrow K^+\Xi^-$ . Measurements for these reactions would be very helpful, especially for comparing with predictions from dynamical coupled-channel (DCC) models [86,87] and other effective Lagrangian approaches [88]. The *Review of Particle Physics* [2] lists only two states with branching fractions (BF) to  $K\Xi$ , namely,  $\Lambda(2100)7/2^-$  (BF < 3%) and  $\Sigma(2030)7/2^+$  (BF < 2%)

## 7.5 $KK\Omega$ Final States

The experimental situation with  $\Omega^{*-}$ s is even worse than for the  $\Xi^*$  case – there are very few data for excited states. The main reason for such a scarce dataset is the very low cross section for their indirect production with pion or photon beams. In Fig. 8(right), we present the cross section for  $\Omega$  production using a  $K^-$  beam [85].

A major effort in LQCD calculations involves the determination of inelastic and multi-hadron scattering amplitudes, and the first calculation to study an inelastic channel was recently performed [89,90]. For lattice calculations involving baryons that contain one or more strange quarks an advantage is that the number of open decay channels is generally smaller than for baryons comprised only of the light  $u$  and  $d$  quarks.

## 7.6 Summary for PWA

Pole positions have been determined (no uncertainties) for several  $\Lambda^*$ s and  $\Sigma^*$ s but information about pole positions has not been determined for  $\Xi$  or  $\Omega$  hyperons [2]. Our plan is to do a coupled-channel PWA with new GlueX KLF data in combination with available and new J-PARC  $K^-p$  measurements when they will be available. Then the best fit will allow the determination of data-driven (model independent) partial-wave amplitudes and associated resonance parameters (pole positions, residues, BW parameters, and so on. Additionally, PWAs with new GlueX data will allow a search for "missing" hyperons via looking for new poles in complex plane positions. It will provide a new benchmark for comparisons with QCD-inspired models and LQCD calculations.

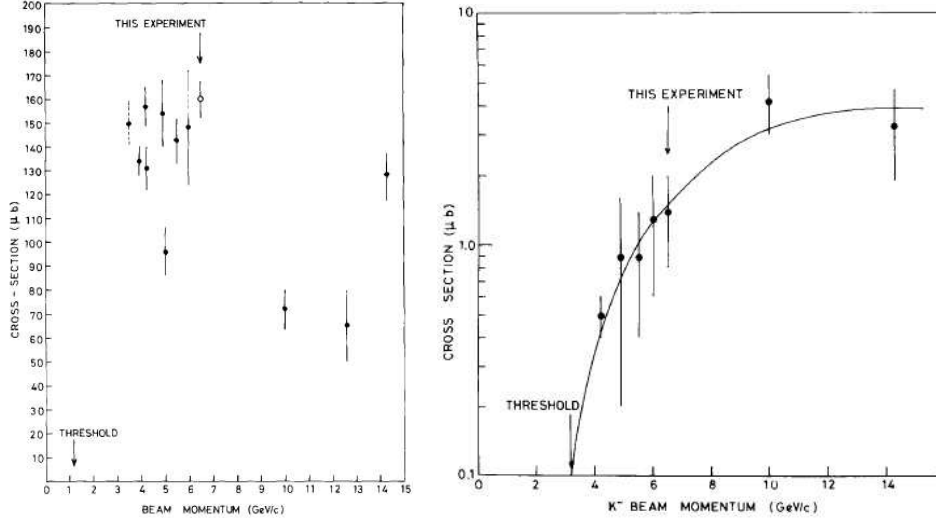


Figure 8: Left panel: Cross section of  $\Xi^-$  production,  $K^- p \rightarrow \Xi^- X$ , as a function of  $K^-$  momentum [85]. Right panel: Cross section of  $\Omega^-$  production,  $K^- p \rightarrow \Omega^- K^+ K^0$ , as a function of  $K^-$  momentum [85]. The curve is a fit by eye to the data.

## 8 Theory for "Neutron" Target Measurements

So-called coupled-channel chiral unitary approaches (UChPT) successfully describe the properties of the  $\bar{K}N$  sub-threshold resonance  $\Lambda(1405)1/2^-$ . Furthermore, such models lead to the prediction that the scattering amplitude has two poles in the complex-energy plane for the quantum numbers of this resonance ( $I = 0, L = 0, S = -1$ ). This coins the so-called the two-pole structure of the  $\Lambda(1405)$ ; see the current *Review of Particle Physics* [2] for more details.

In the most recent formulation, the aforementioned UChPT approaches rely on a chiral amplitude for the meson-baryon scattering up to next-to-leading chiral order. Whereas the unitarity constraint is usually imposed via the Bethe-Salpeter equation either in the full off-shell formulation [94, 95] or in the so-called on-shell approximation, e.g. [25, 91, 92]. For the analysis of data the former is quite intricate, while as it was shown in Ref. [94] the off-shell effects are rather small. Therefore, it is meaningful to use the latter formulation. Recently, a direct quantitative comparison of the on-shell models [25, 91–93] was performed in Ref. [23]. It was found there that various models, which typically have many free parameters, adjusted to the same experimental data, predict very different behavior of the scattering amplitude on and off the real-energy axis. This systematic uncertainty becomes evident, when comparing the pole positions of the  $\Lambda(1405)$  in these models (see Fig. 9). The position of the narrow (first) pole seems to be constrained at least in the real part rather well, while the predictions for the position of the broad (second) pole cover a very wide region of the complex-energy plane. This uncertainty is present even within models of the same type. This ambiguity can be traced back to the fact that the experimental data used to fix the parameters of the models are rather old and imprecise. It is expected that the proposed KLF experiment will lead to an improvement of this situation, as described below.

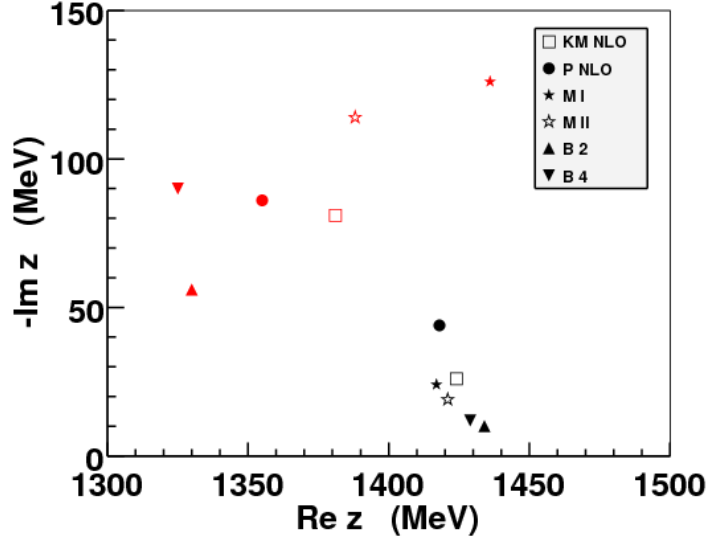


Figure 9: Pole positions of the  $\Lambda(1405)$  for chiral unitary approaches -  $KM$  from Ref. [91],  $B$  from Ref. [25],  $M$  from Ref. [92] and  $P$  from Ref. [93] as compared in Ref. [23]. Each symbol represents the position of the first (black) and second (red) pole in each model.

The  $K_L$  beam can be scattered on a "neutron" target, while measuring the strangeness  $S = -1$  final meson-baryon states (see, e.g., Sec. 7). In such a setup, the proposed experiment can become a new and very strongly desired new source of experimental data to pinpoint the properties of the  $\overline{K}N$  scattering amplitude. To make this statement more quantitative, we compare predictions of both solutions of the model<sup>1</sup> from Ref. [25]. These solutions agree with all presently available scattering, threshold as well as the photoproduction data for the  $\pi\Sigma$  line shapes by the CLAS Collaboration [24]. The predicted differential cross sections ( $d\sigma/d\Omega$ ) as well as polarized ones ( $Pd\sigma/d\Omega$ ) for the  $K_L n$  scattering with the final states  $K^-p$ ,  $\overline{K}^0 n$ ,  $\pi^0\Lambda$ , and  $\pi^{0/+/-}\Sigma^{0/+/-}$  are presented in Figs. 10 and 11, respectively. There is very little agreement on the prediction of these observables in the energy range aimed to study in the proposed  $K_L$  experiment. The latter is very encouraging, meaning that the actual data can sort out one (or maybe both) solutions as unphysical, which was not possible based on present experimental data.

In summary: The proposed KLF experiment will lead to new constraints on  $\overline{K}N$  models; thus, these data will sharpen our understanding of the long-debated nature of strangeness  $S = -1$  resonances.

<sup>1</sup>The choice of this model for the present analysis is justified by the fact that it includes the  $p$ -wave interaction in the kernel of the Bethe-Salpeter equation explicitly.



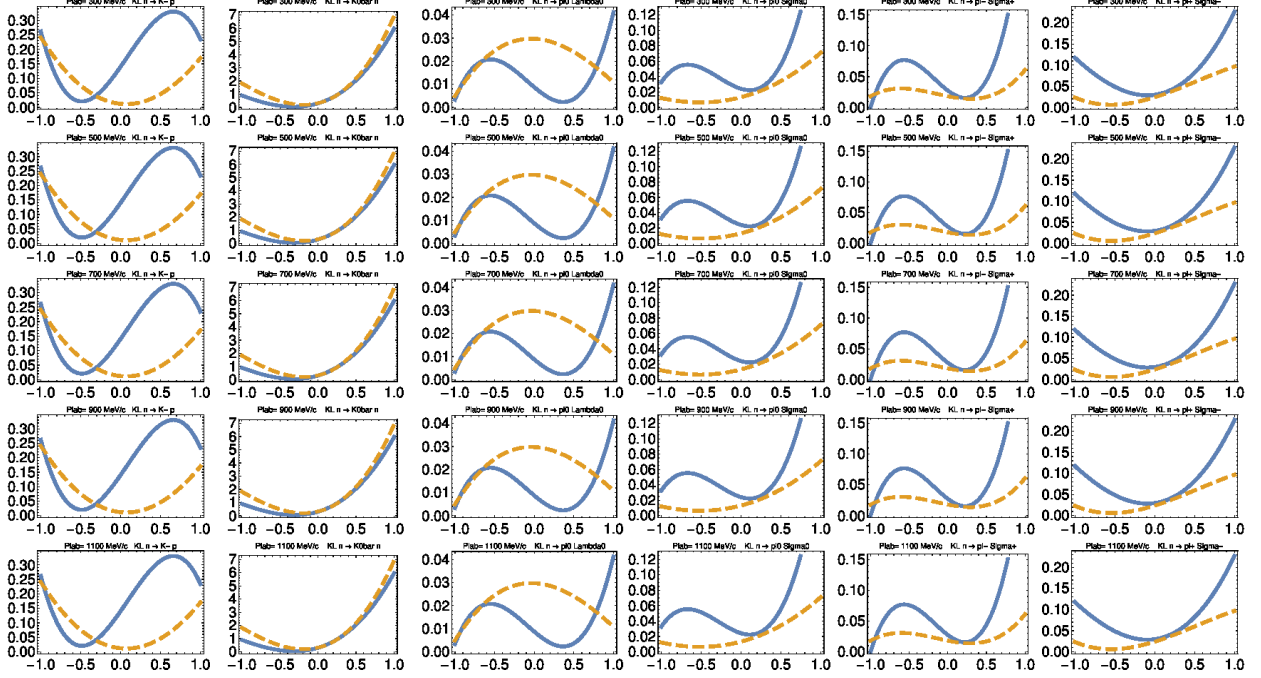


Figure 10: Theoretical predictions for differential cross sections,  $d\sigma/d\Omega$ , for reactions (columns)  $K_L n \rightarrow K^- p$ ,  $K_L n \rightarrow \bar{K}^0 n$ ,  $K_L n \rightarrow \pi^0 \Lambda$ ,  $K_L n \rightarrow \pi^0 \Sigma^0$ ,  $K_L n \rightarrow \pi^- \Sigma^+$ , and  $K_L n \rightarrow \pi^+ \Sigma^-$  as a function of c.m.  $\cos \theta$ . Each row associated with kaon lab momentum of 300, 400,  $\dots$  1000 MeV/c of initial neutral kaon beam. Orange dashed and blue solid lines show predictions within Model-B2 and Model-B4, respectively (see text for details).

## 9 Strange Meson Spectroscopy: $K\pi$ Interaction

The main source of our knowledge of kaon scattering amplitudes comes from the kaon beam experiments at SLAC in the 1970s and 1980s. The scattering amplitudes for the  $\pi K$  final state were extracted from reactions using a proton target by extrapolating to small momentum transfer,  $t$ , dominated by nearly-on-shell pion exchange. Phase-shift analysis of the flavor exotic isospin-3/2 amplitudes extracted from  $K^+ p \rightarrow K^+ \pi^+ n$  and  $K^- p \rightarrow K^- \pi^- \Delta^{++}$  reactions by Estabrooks *et al.* [96] indicates a weak repulsive S-wave interaction and very weak attractive interactions in P-wave and higher waves. In isospin-1/2, in addition to Estabrooks *et al.*, there is a considerable set of  $\pi K$  scattering data provided by the LASS experiment [97]. Reactions with the final states  $\pi K$ ,  $\eta K$  and  $\pi\pi K$  final states have been measured. In the PWA of  $\pi K \rightarrow \pi K$ , a peaking amplitude in S-wave is interpreted as a broad  $K^*(1430)$  resonance that appears to saturate unitarity. The narrow elastic vector resonance,  $K^*(892)$ , manifests itself as a rapid rise in the P-wave phase-shift. The D-wave amplitude has a peak, well below the unitarity limit, that can be interpreted as an inelastic  $K_2^*(1430)$  resonance. Further resonances in the "natural parity" series ( $J^P = 3^-, 4^+$ , and  $5^-$ ) are observed at higher energies.

The  $\eta K$  is another inelastic channel to open, but LASS reports no significant amplitude into  $\eta K$

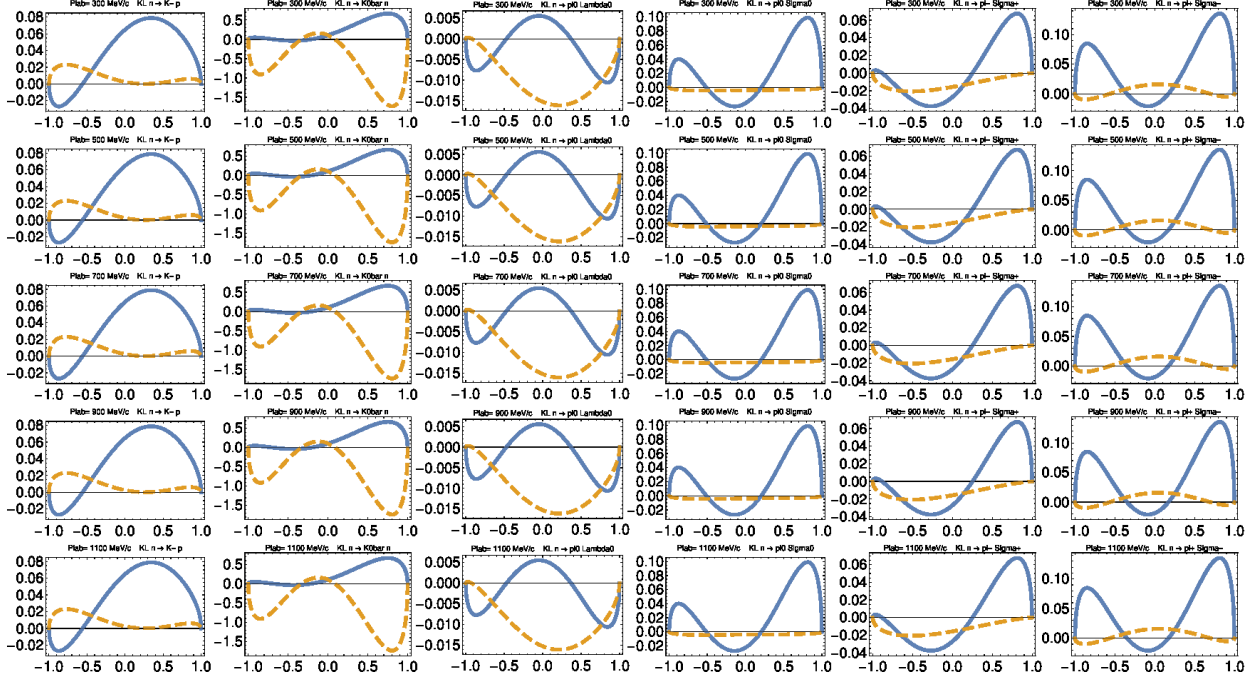


Figure 11: Theoretical predictions for polarized differential cross sections,  $Pd\sigma/d\Omega$ . The notation is the same as in Fig. 10.

for  $W < 2$  GeV in S-, P-, and D- waves. Indeed the inelasticity in P, D-waves and higher appears to come first from the  $\pi\pi K$  final state, where a significant amplitude is seen in  $1^-$  above 1.3 GeV and a peak in  $2^+$  at the  $K_2^*(1430)$ . The  $\pi\pi K$  also couples to the "unnatural parity" series, notably to  $J^P = 1^+$ , where peaking behavior is observed that is commonly described in terms of two axial resonances,  $K_1(1270)$  and  $K_1(1400)$ . Much higher statistics is needed to improve our knowledge on all these states.

Recently LQCD studies with  $m_\pi = 391$  MeV were performed to search for resonances in coupled  $\pi K$  and  $\eta K$  scattering [89]. Scalar  $\pi\pi/\overline{K}K$  and  $K\pi/K\eta$  form factors have been calculated within a variety of approaches using (unitarized) chiral perturbation theory [98–105] and dispersion relations [104, 106, 107], in many cases using the former to constrain polynomial ambiguities of the latter.

Measuring  $\pi K$  scattering provides a possibility for studying scalar and vector  $K^*$  states, including the S-wave  $\kappa(800)$  state (see [108, 109]), which is not yet well established. Such studies are also necessary to get precise vector and scalar  $\pi K$  form factors as an input for the extraction of the Cabibbo-Kobayashi-Maskawa (CKM) matrix element  $V_{us}$  from  $\tau \rightarrow K\pi\nu$  decay.  $\pi K$  scattering amplitudes with high precision are needed to study CP violation from Dalitz plot analyses of both open charm  $D$ -mesons [110] and the charmless decay of  $B$ -mesons [111] into  $K\pi\pi$  final state.

In Fig. 12, we present the phase of the form factor  $F_+(s)$  with experimental results of LASS Estabrooks [96, 97] together with the fit of Boito *et al.* to  $\tau$  decay data [112].

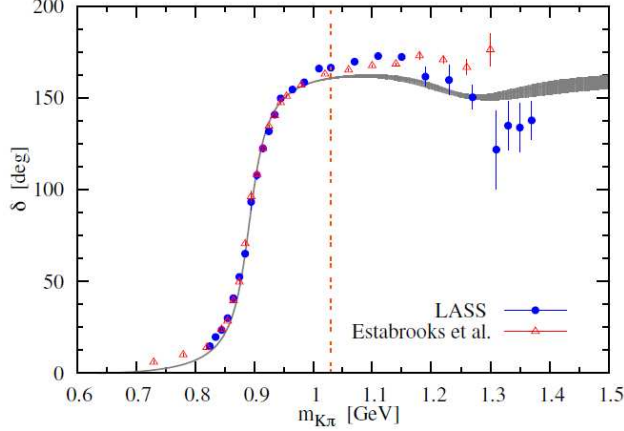


Figure 12:  $I=1/2$   $K\pi$  scattering P-wave phase shift together with experimental results from LASS [97] and Estabrooks *et al.* [96]. The opening of the first inelastic  $\pi K^*$  channel is indicated by dashed vertical line. The gray band represents the fit results from Boito *et al.* [112].

As one can see, all experimental data obtained at SLAC have very poor statistics above 1.2 GeV; furthermore, the data do not extend to higher energies, which are even more important for  $B$ -meson decays. Moreover, direct comparison of charged  $K^\pm\pi^\mp$  with  $\tau$  assumes isospin invariance as in the  $\tau$  decay one has  $K_S\pi^\pm$  final state depending on the sign of  $\tau$  lepton.

Similarly, as one can see from Fig. 13, the  $I = 1/2$  and  $I = 3/2$  S-wave and  $I = 3/2$  P-wave phase shifts are very poorly measured and need more experimental data.

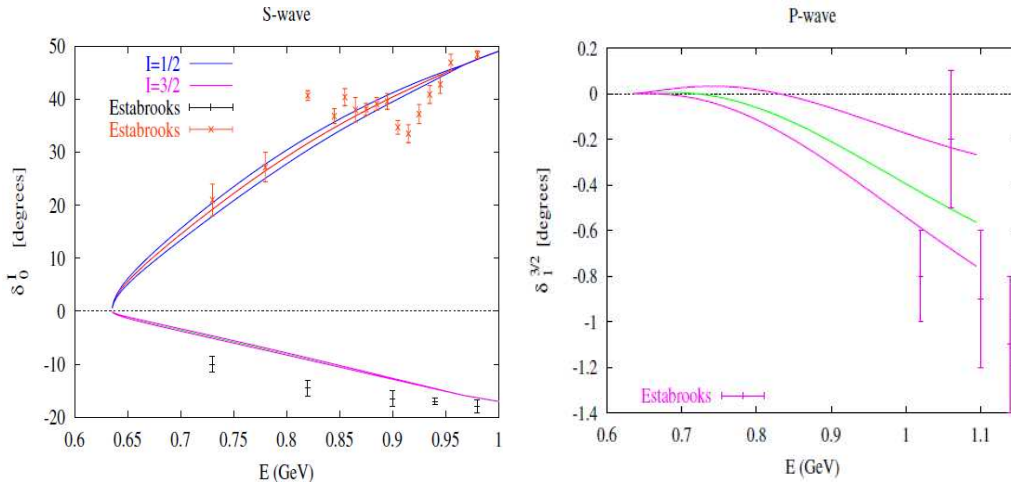


Figure 13: Left panel:  $I = 1/2$  S-wave phase shift (curves and data in the upper half of the figure) and the  $I = 3/2$  S-wave phase shift (curves and data in the lower half). Experimental data are from SLAC experiments as in previous figure. The curves are obtained from central, upper, and lower values of parameters in the Roy-Steiner solutions ellipse [113]. Right panel: Same as in previous figure for  $I = 3/2$ . Data points are from Estabrooks *et al.* [96].

The intensive beam flux of the proposed  $K_L$  beam will provide high statistics data on both charged

$K\pi$  as well as with final-state neutral kaon in the reactions:

- $K_L p \rightarrow K^\pm \pi^\mp p$  (simultaneously measurable with  $K_L$  beam).
- $K_L p \rightarrow K_S \pi^+ n$  on a proton target (*for the first time*).
- $K_L n \rightarrow K_S \pi^- p$  on a deuteron target (*for the first time*).

In summary: Experimental data obtained in the proposed KLF experiment at JLab will provide valuable data to search for yet not well understood and possibly incomplete scalar, vector, and tensor resonances in the strange sector through a phase-shift analysis of  $\pi K$  and  $\eta K$  scattering amplitudes.

## 10 Proposed Measurements

We propose to use the KL Facility with the GlueX spectrometer, in JLab Hall D, to perform precision measurements of  $K_L p \rightarrow KY^*$  from liquid hydrogen and deuterium cryotarget (LH<sub>2</sub>/LD<sub>2</sub>) in the resonance region,  $W = 1490 - 3500$  MeV and c.m.  $\cos\theta$  from  $-0.95$  to  $0.95$ . It will operate at a neutral kaon flux of  $3 \times 10^4$   $K_L/s$ . The ability of GlueX to measure over wide ranges in  $\theta$  and  $\phi$  with good coverage for both charged and neutral particles, together with the  $K_L$  energy information from the KL Facility, provide an ideal environment for these measurements.

### 10.1 $K_L$ Beam in Hall D

A schematic view of the Hall D beamline for KLF is presented in Fig. 14. At the first stage,  $E = 12$  GeV electrons produced at CEBAF will scatter in the radiator of the Compact Photon Source (CPS), generating an intense beam of untagged bremsstrahlung photons. The Hall D tagger magnet and detectors will not be used. At the second stage bremsstrahlung photons, created by electrons at a distance about 75 m upstream, hit the Be target assembly located in the cave, and produce neutral kaons along with neutrons and charged particles. Finally,  $K_L$  mesons will reach the LH<sub>2</sub>/LD<sub>2</sub> cryotarget inside the GlueX spectrometer.

Our calculations have been performed for the JLab Hall D beamline geometry. The primary  $K_L$  production target has been placed in the Hall D collimator cave. For the target material, we selected beryllium because, for thick targets, the  $K_L$  yield is roughly proportional to the radiation length and density, which gives beryllium as the best candidate. The beam plug and sweeping magnet are placed right after the target. For our calculations, we took a simple beam plug: a 15 cm thick piece of lead. The permanent sweeping magnet cleans up the charged component and has a field integral of 0.8 Tesla-meter, which is enough to remove all charged background coming out of the beam plug. The vacuum beam pipe has a 7 cm diameter and prevents neutron rescattering in air. There are two collimators: one is placed before the wall between collimator cave and experimental hall, while the other is placed in front of the Hall D detector. The distance between the primary Be target

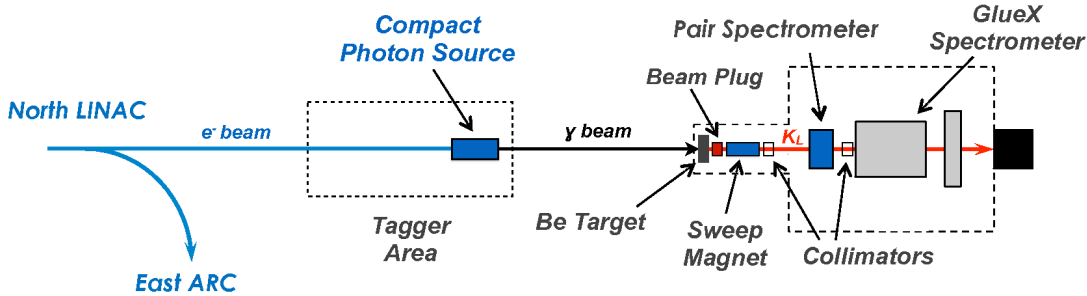


Figure 14: Schematic view of Hall D beamline on the way  $e \rightarrow \gamma \rightarrow K_L$ . Electrons first hit the tungsten radiator, then photons hit the Be target assembly, and finally, neutral kaons hit the  $\text{LH}_2/\text{LD}_2$  cryotarget. The main components are CPS, Be target assembly, beam plug, sweep magnet, and pair spectrometer. See the text for details.

and the  $\text{LH}_2/\text{LD}_2$  target (located inside Hall D detector) was taken as 16 m in our calculations. It can be increased up to 20 m.

### 10.1.1 Compact Photon Source: Conceptual Design

An intense high-energy gamma source is a prerequisite for the production of the  $K_L$  beam needed for the new experiments described in this proposal. In 2014, Hall A Collaboration has been discussed a novel concept of a Compact Photon Source (CPS) [114]. It was developed for a *Wide-Angle Compton Experiment* proposed to PAC43 [115]. Based on these ideas, we suggested (see Ref. [116]) to use the new concept in this experiment. A possible practical implementation adjusted to the parameters and limitations of the available infrastructure is discussed below. The vertical cut of the CPS model design, and the horizontal plane view of the present Tagger vault area with CPS installed are shown in Fig. 15.

The CPS design combines in a single properly shielded assembly all elements necessary for the production of the intense photon beam, such that the overall dimensions of the setup are limited and the operational radiation dose rates around it are acceptable. Compared to the alternative, the proposed CPS solution presents several advantages: much lower radiation levels, both prompt and post-operational due to the beam line elements' radio-activation at the vault. The new de-



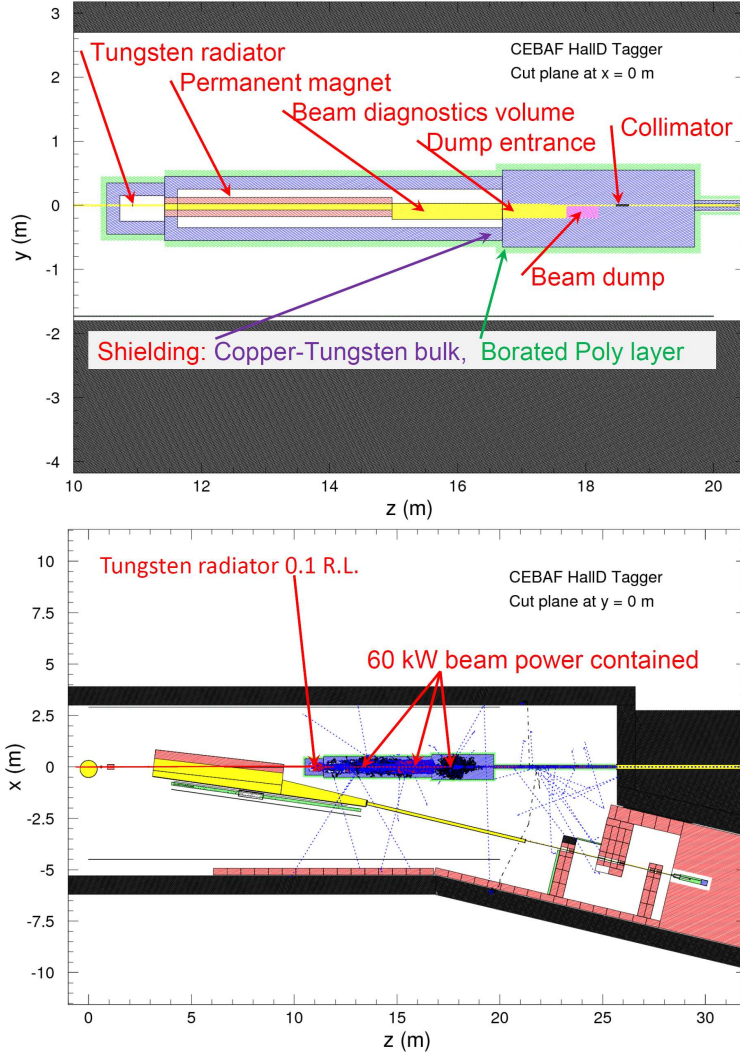


Figure 15: Elements of the design are indicated in the top panel (vertical cut plane of the DIN-REG/Geant3 model of the CPS). The bottom panel shows the CPS assembly in the Tagger vault and simulations of 2000 beam electrons at 12 GeV.

sign provides much less disturbance of the available infrastructure at the Tagger Area, and better flexibility in achieving high-intensity photon beam delivery to Hall D. The new CPS solution will satisfy the proposed  $K_L$  beam production parameters; we do not envision any significant technical or organizational difficulties in the implementation of the conceptual design.

The new setup utilizes the Hall D Tagger vault, properly shielded by design to accommodate the medium power beam dump capable of accepting up to 60 kW of 12 GeV  $e^-$  beam, assuming that proper local shielding is set around the dump. The presently installed dump is placed behind the iron labyrinth walls, and is surrounded by a massive iron shielding, made of iron blocks available at the time of construction. The standard GlueX setup is optimized for operations using very thin radiators producing relatively low intensity photon beam such that the beam electrons losing energy to photon production in the radiator may be detected and counted in the tagger hodoscope counters. The present setup is not suitable for production of massively more intense photon beams

needed for the  $K_L$  production, due to the expected overwhelming radiation and activation levels in the vault.

The new proposed CPS solution solves the problem by incorporating the new thick radiator and the new beam dump in one assembly installed along the straight beam line exiting from the tagger magnet (presently the line is used as the photon beam line). The new CPS device should be capable of taking the same beam power of 60 kW, using optimized shielding made of high-Z material, which would make the necessary equivalent shielding compact, requiring less total weight of the shielding. Qualitatively, if one needs a sphere of iron (8 g/cm<sup>3</sup>) of 2 m radius for the shielding, it may be roughly replaced by a sphere of 1 m radius made of tungsten-copper (16 g/cm<sup>3</sup>), with its weight actually four times smaller. The optimized design is able to limit the prompt radiation dose rates around the CPS to the present operational levels, while significantly limiting the post-operational doses around the heavily shielded assembly. Of course, the inner parts of the CPS device will be activated to high levels, preventing immediate access and disassembly, so the engineering requirements to the reliability of all parts inside must be strict. The overhead shielding at the CPS location in the tagger vault is about the same thickness (13 feet) of concrete and berm as at the present dump location. It will keep the radiation doses outside and at the CEBAF boundary within the design limits for the site.

The proposed CPS solution is just conceptual, and a full cycle of engineering design is required before the final optimized solution is found. The cost and space limitations will determine the choice of shielding materials for the CPS. Details of the dump and magnet design will also be included in the overall optimization process, taking into account the considerations of cost and reliability of the final device. We are considering a possible joint development of the more universal CPS solutions in collaboration with other experimental projects at JLab interested in implementing similar designs for their experiments [117].

### 10.1.2 Simulations Study of $K_L$ Beam Production

Neutral kaon production was simulated for a photon bremsstrahlung beam produced by the 12 GeV electron beam in the Hall D CPS. The main mechanism of  $K_L$  production in our energy range is via  $\phi$ -meson photoproduction, which yields the same number of  $K^0$  and  $\bar{K}^0$ . Another mechanism is hyperon photoproduction (yielding only  $K^0$ ), which was not studied in our simulations separately. Instead, we have taken as an alternative model the Pythia generator [118], which includes hyperon production. Total and differential cross sections for the  $\phi$ -meson photoproduction on proton and complex nuclei (coherent and incoherent) data were taken from Refs. [119, 120]. The angular distributions that we used for  $\phi \rightarrow K_L K_S$  decay are from Ref. [119, 121, 122]. Our calculations show that the  $\phi$  decay in its rest frame is mostly perpendicular to the axis of  $\phi$  momentum. Since  $K_L$ s need to stay along the original photon beam direction to get to the LH<sub>2</sub>/LD<sub>2</sub> cryotarget, this condition requires that the  $\phi$  production and decay angles in the laboratory frame be about the same. That means that we will have only  $K_L$ s from  $\phi$ -mesons produced at relatively high momentum transfer  $t$  at the Be target. It suppresses the number of "useful"  $K_L$ s by a factor of  $\sim 3$  or more (in comparison with the case if  $K_L$  and  $K_S$  momenta are parallel to the  $\phi$  momentum).  $K_L$  absorption, used in our calculations, was studied in Ref. [123] very well. About 80% of the produced  $K_L$ s will be absorbed in the Be target and following tungsten and water beam plug. The value of absorbed

$K_L$ s can be reduced by optimizing the beam plug setup.

### 10.1.3 $K_L$ Beam Parameters

One of the main  $K_L$ -beam parameters is the momentum distribution (momentum spectrum as a function of the distance and angle) [124]. Results of our simulations for the  $K_L$  momentum spectrum for those  $K_L$  reaching the LH<sub>2</sub>/LD<sub>2</sub> cryotarget is shown in Fig. 16. The spectrum first increases with  $K_L$  momentum up to  $\sim 4$  GeV/c since the  $\phi$  decay cone angle decreases at higher  $\gamma$ -beam and  $K_L$  momenta. This selects lower  $\phi$  production  $t$  values, which are more favorable according to the  $\phi$  differential cross section. At a certain point, the highest possible  $\gamma$ -beam momentum is reached and the  $K_L$  momentum spectrum decreases to the endpoint. For comparison, we selected part of the  $K_L$  spectrum from the Pythia generator that originated only from  $\phi$  decays and showed it on the same plot (red histogram). Pythia calculations show that  $\phi$  decays yield roughly 30% of the  $K_L$  flux. The number of  $K^0$  exceeds the number of  $\bar{K}^0$  by 30% according to this generator for our conditions. Their momentum spectra are shown in Fig. 17 separately.

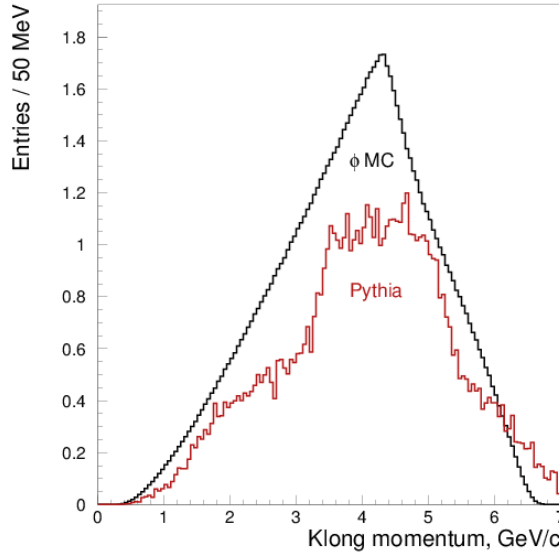


Figure 16:  $K_L$  momentum spectra originating from  $\phi$  decays: black histogram - our simulations using DINRREG/Geant3 [125], red histogram - Pythia generator result [118].

To estimate the expected rate of  $K_L$ s at the LH<sub>2</sub>/LD<sub>2</sub> cryotarget, we used the following conditions:

- electron beam current  $5 \mu\text{A}$ ,
- 10% R.L. tungsten radiator in CPS,
- Be-target diameter is 3 cm and length is 40 cm,
- and a cryotarget LH<sub>2</sub>/LD<sub>2</sub> radius of 3 cm



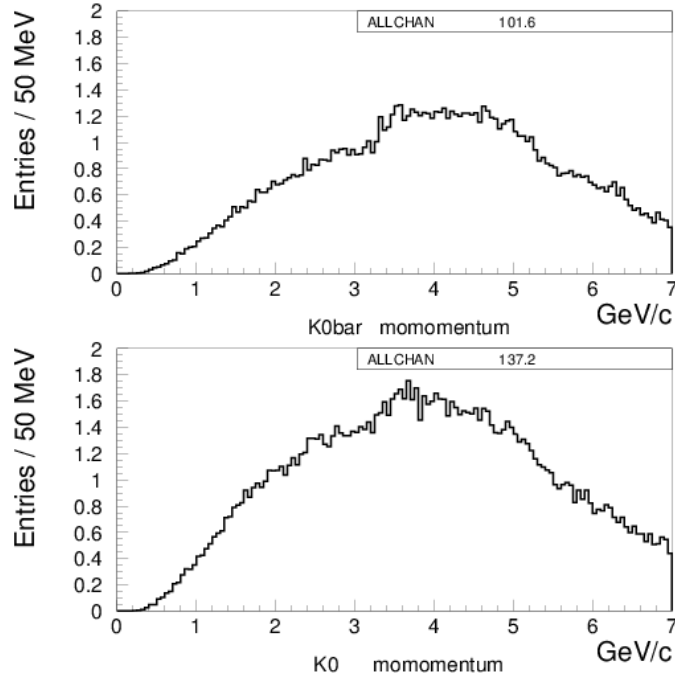


Figure 17: Momentum spectra from Pythia generator [118]. Top plot for  $\overline{K^0}$ . Bottom plot for  $K^0$ .

which results in a beam flux of about  $3 \times 10^4$   $K_L$ /s from all production mechanisms at the  $LH_2/LD_2$  target (Fig. 18). We simulated the  $K_L$  and neutron production from  $6 \times 10^9$  12-GeV electrons under these conditions for the GlueX  $K_L$  Facility and the results (Fig.18(left)) are in reasonable agreement with the  $K_L$  spectrum measured by SLAC at 16 GeV (Fig. 18(right)).

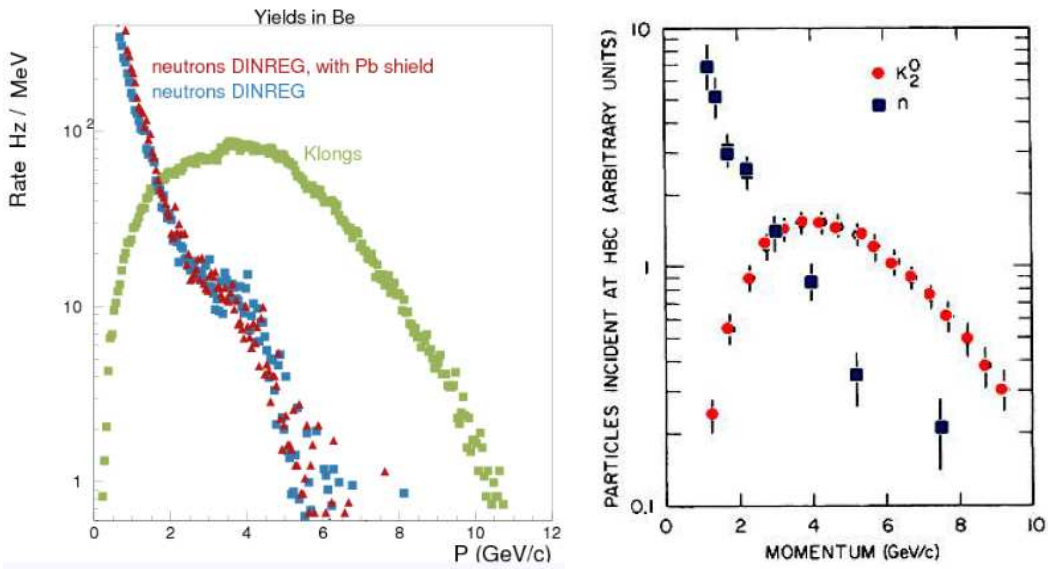


Figure 18:  $K_L$  and neutron momentum spectra. Left plot: The rate of  $K_L$  (green filled squares) and neutrons (blue and red filled squares and triangles) on  $\text{LH}_2/\text{LD}_2$  cryogenic target of Hall D as a function of their generated momentum, with a total rate of  $3 \times 10^4 K_L/\text{s}$ . Neutron calculations were performed using the JLab package DINREG/Geant3 [125]. Right plot: Experimental data from SLAC measurements using a 16 GeV/c electron beam from Ref. [77]. The rate of  $K_L$  (red filled circles) and neutrons (black filled squares).

### 10.1.4 $K_L$ Beam Background: Gammas, Muons, and Neutrons

Background radiation conditions are one of the most important parameters of the  $K_L$  beam for the JLab GlueX KL Facility [124].

#### 1. Gamma Background

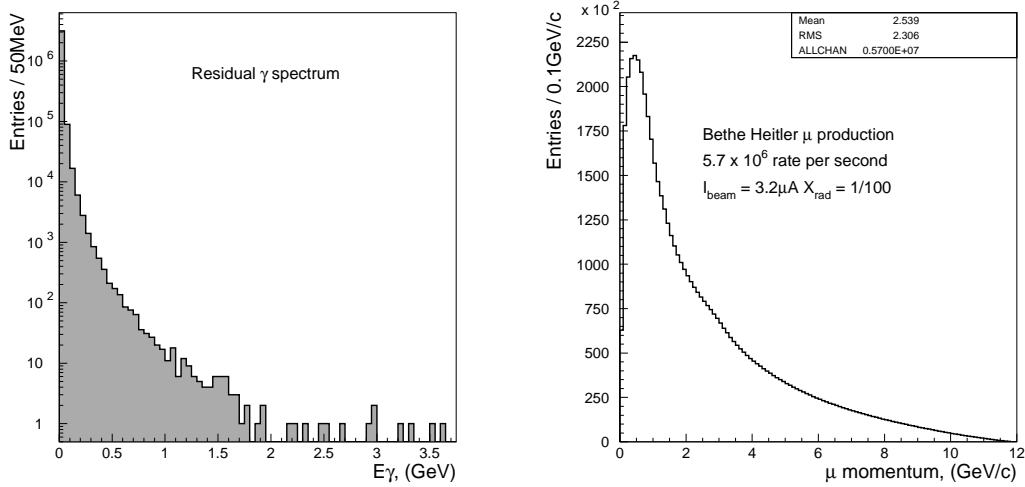


Figure 19: Left panel: Momentum spectrum of residual  $\gamma$ s just after the concrete shielding. Right panel: Muon momentum spectrum for Bethe-Heitler production.

After passing through 30% R.L. tungsten beam plug and the charged background component removed by the sweep magnet, we will have some residual  $\gamma$  background and neutrons produced by EM showers. The momentum spectrum of residual  $\gamma$ s is shown in Fig. 19(left). It decreases exponentially with increasing energy of photons. For the rates, we obtained  $\sim 10^5 \text{ s}^{-1}$  for  $\gamma$ s with energy above 50 MeV and  $\sim 10^3 \text{ s}^{-1}$  for  $\gamma$ s with energy above 500 MeV.

Overall, the gamma flux for the KLF experiment is tolerable.

#### 2. Muon Background

Following Keller [126], our Geant4 [127] simulations included Bethe-Heitler muon background from the Be-production target and photon dump, both background into the detector and muon dose rate outside Hall D. Obviously, most of the muons are produced in the photon dump. Our calculations show that muons will be swept out of the  $K_L$  beam line; thus, they are not inherently a significant background. However, due to their high penetration ability, it might be important for purposes of the shielding. We have taken into account only the Bethe-Heitler muon production process. Muons from pion decays and other production mechanisms will increase the total muon yield only slightly. They were not included in our model. The number of produced muon in the Be target and lead beam plug is about the same, but muons originating in lead have a much softer momentum spectrum. The estimated number of produced muons is  $\sim 6 \times 10^6 \text{ s}^{-1}$ . Their momentum spectrum is shown

in Fig. 19(right). The above number will increase by factor of 15 with  $I_e = 5\mu A$  and the radiator of 0.1 radiation length.

To summarize: Half of muons will have momenta higher than 2 GeV/c,  $\sim 10\%$  of muons will have momenta higher than 6 GeV/c, and  $\sim 1\%$  of muons will have momenta above 10 GeV/c. Overall, the muon flux for the KLF experiment is tolerable.

### 3. Neutron Background

To estimate the neutron flux in a beam and neutron dose in the experimental hall from scattered neutrons we used the MCNP6 N-Particle (MCNP) Transport code [128]. See Appendix A4 (Sec. 16) for further details. The experimental hall, beam cave, and photon beam resulted from tungsten radiator were modeled using the specifications from the layout presented in Fig.14. Figure 20 shows a graphic model of the experimental setup.

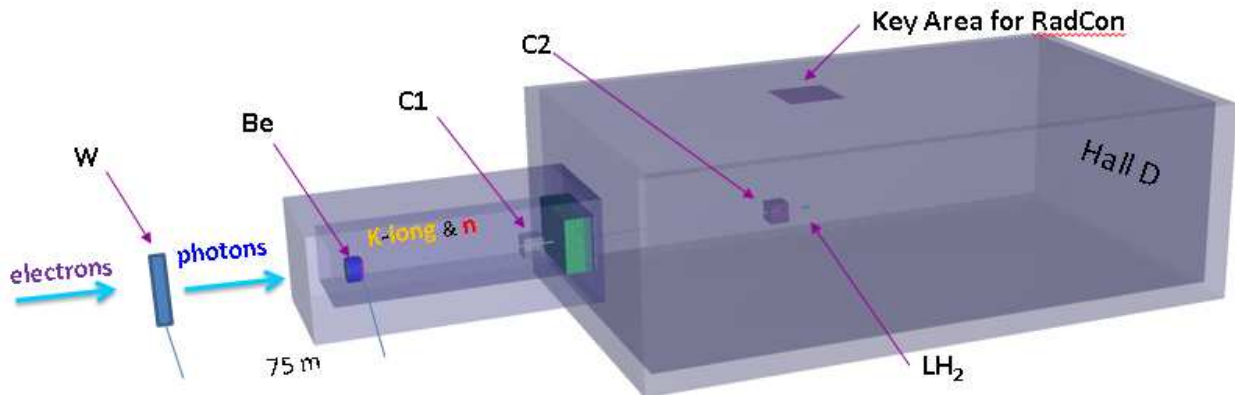


Figure 20: Schematic view of Hall D setting for MCNP6 transport code [128] calculations. Beam goes from left to right. The model is presented as semi-transparent for demonstration purposes. This 3D plot is similar as Fig. 14 shows.

The physical models implemented in the MCNP6 code take into account bremsstrahlung photon production, photonuclear reactions, gamma-ray and neutron multiple scattering processes. We ignored the GlueX detector setting in these calculations.

The MCNP model simulates a 12 GeV  $5\mu A$  electron beam hitting the tungsten radiator. Electron transport was traced in tungsten radiator, vacuum beam pipe for bremsstrahlung photons, and Be target. Neutrons and gamma rays were traced in all components of the used MCNP model. The media outside concrete walls of the beam cave and bremsstrahlung photon beam pipe was excluded from consideration to facilitate the calculations.

The tally to estimate neutron fluence at the experimental hall ceiling just above the  $LH_2/LD_2$  target, at Key Area for RadCon shown in Fig. 20. The neutron dose calculated for the layout from Fig. 41 is  $14.1 \pm 1.6$  mrem/h,  $2.7 \pm 0.8$  mrem/h for the layout from Fig. 42, and  $0.2 \pm 0.07$  mrem/h for the layout from Fig. 43. Neutron Fluence-to-Effective Dose conversion factors from ICRP 116 [129] were implemented to convert neutron fluence to effective dose. The neutron flux at the face of the  $LH_2/LD_2$  target is about  $2 \times 10^3$  N/(s·cm<sup>2</sup>) and is almost independent of the shielding location in the beam cave.

Overall, the neutron flux for the KLF experiment is tolerable and below the RadCon limit.

### 10.1.5 $K_L$ Momentum Determination and Beam Resolution

The mean lifetime of the  $K_L$  is 51.16 ns ( $c\tau = 15.3$  m) whereas the mean lifetime of the  $K^-$  is 12.38 ns ( $c\tau = 3.7$  m) [2]. For this reason, it is much easier to perform measurements of  $K_L p$  scattering at low beam energies compared with  $K^- p$  scattering.

The momentum of a  $K_L$  beam can be measured using time-of-flight (TOF) - the time between the accelerator bunch (RF signal from CEBAF) and the reaction in the  $\text{LH}_2/\text{LD}_2$  target as detected by the GlueX spectrometer. Thus the TOF resolution is a quadratic sum of accelerator time and GlueX spectrometer time resolutions. Since the accelerator signal has a very good time resolution ( $\sim 150$  ps or better), TOF resolution will be defined by GlueX detector. The time resolution of the GlueX detectors are discussed in Sec. 10.1.6. In our calculations, we used time resolutions from 50 ps to 300 ps to show the dependence of the beam momentum and  $W$  resolution.

Of course, to get TOF information, the electron beam needs to have a narrow bunch time structure with a bunch spacing of, at least, 60 ns. In order to be able to measure the roughly 20 ns ToF of the elastic protons, the beam for the  $G0$  experiment at Hall C has 32 ns between electron bunches (in contrast to the usual 2 ns spacing for each experimental hall) using a 31.1875 MHz pulsed laser to operate the electron source [130]. One cannot expect a problem with a 60 ns time structure to delivery an electron beam to any Hall, A, B, or C [131].

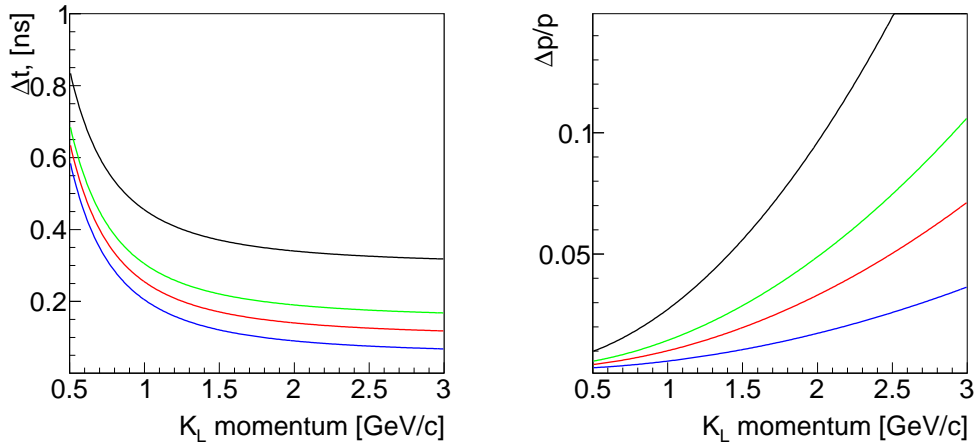


Figure 21: Left plot: Time resolution,  $\Delta t$ , for  $K_L$  beam as a function of  $K_L$  momentum. Right plot: Momentum resolution,  $\Delta p/p$ , as a function of momentum. For 300 ps (black), 150 ps (green), 100 ps (red), and 50 ps (blue) time resolutions.

The uncertainty in a neutral kaon production position at lower momenta ( $p < 0.5$  GeV/c) affects timing resolution caused by the TOF difference between the photon and kaon time traversing the Be target, however, as  $\Delta p/p = \gamma^2 \Delta T/T$  momentum resolution is below 1% at lower momenta. Figure 21 shows TOF,  $\Delta t$ , (left) and beam momentum resolution,  $\Delta p/p$  (right) as a function of the

$K_L$  beam momentum, respectively. The TOF resolution is flat for momenta higher than 1 GeV/ $c$ . The momentum resolution decreases with momentum: for 1 GeV/ $c$  it is  $\sim 1.4\%$  and for 2 GeV/ $c$  it is  $\sim 5\%$ . Figure 22 shows that for  $W < 2.1$  GeV,  $\Delta W < 30$  MeV, which is suitable for studying low-lying hyperons with widths of  $\Gamma = 30 - 50$  MeV [2]. For fully reconstructed final states  $W$  can be reconstructed directly, which provides a better resolution in the region where the TOF method deteriorates,  $W > 2.1$  GeV (see green dashed curve in Fig. 22).

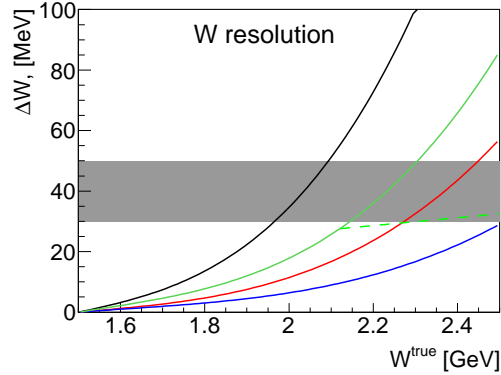


Figure 22: Energy resolution,  $\Delta W/W$ , as a function of energy, for 300 ps (black), 150 ps (green), 100 ps (red), and 50 ps (blue) time resolution. Green dashed line shows approximate  $W$  resolution from reconstruction of final-state particles. Shaded area corresponds to typical hyperon width.

### 10.1.6 GlueX Detector Time Resolution

The  $K_L$  beam momentum and time resolution is governed by the time resolution provided by the GLUEX detector from the reconstruction of charged particles produced in the  $\text{LH}_2/\text{LD}_2$  target. There are three detector systems that can provide precision timing information for reconstructed charged particles in GLUEX: the Start Counter (ST), Barrel Calorimeter (BCAL), and Time of Flight (TOF) detectors. The aforementioned detectors, and the charged particle time resolutions they provide, are discussed in this section.

The GLUEX Start Counter is a cylindrical plastic scintillator detector surrounding the  $\text{LH}_2/\text{LD}_2$  target, with 3 mm thick scintillator bars and a tapered nose region that bends toward the beamline at the downstream end. The scintillation light from each of the 30 scintillator bars is detected by an array of 4,  $3 \times 3 \text{ mm}^2$  Hamamatsu S10931-050P surface mount silicon photomultipliers (SiPMs) [132]. The time resolution of the ST was determined to be 250 ps during the 2016 and 2017 GLUEX run periods, as shown in Fig. 23, and thus provided adequate separation of the 250 MHz photon beam bunch structure delivered to Hall D during that time. This performance was achieved using the recommended operating gain and bias voltages supplied by Hamamatsu to provide both the FADC 250 analog signals and precision FITDC discriminator signals used in the GLUEX reconstruction. For the  $K_L$  program we propose to increase the gain of the ST SiPMs, thereby increasing the number of detected photoelectrons, as well as modify the pulse-shape processing electronics. Similar gain and readout electronic customization were implemented

in the GLUEX Tagger Microscope, which utilizes an identical SiPM readout system, and provided timing resolutions of 200 ps. Implementation of these non-invasive modifications to the ST will significantly improve the timing resolution. We, therefore, assumed a 150 ps resolution as the baseline ST performance, which may be achieved with modifications to the current device.

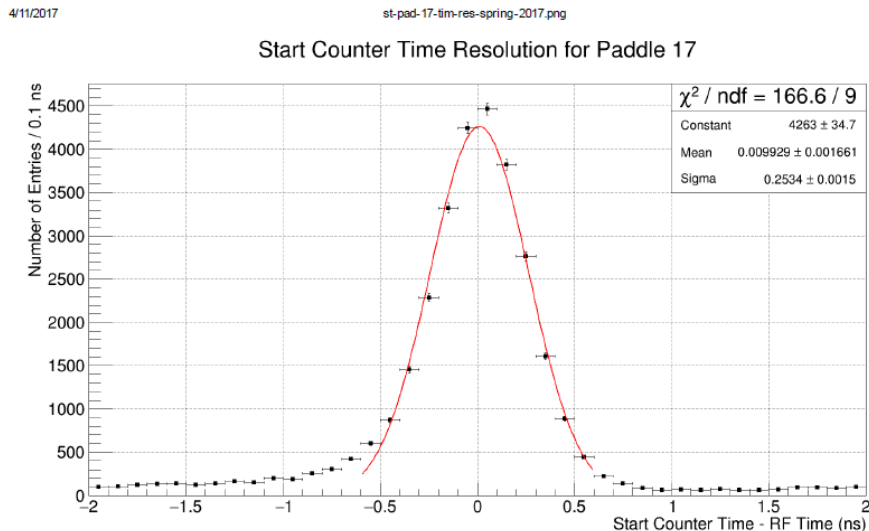


Figure 23: Time difference between the measured and expected ST time from the Spring 2017 GLUEX run period. The data were fitted with a Gaussian to determine the current time resolution of  $\sim 250$  ps.

Future improvements to the start counter to reduce the time resolution further will be studied to increase both the light production in the scintillators and the light collection efficiency. A future goal would be to reach a time resolution of 50-100 ps for the ST, which would likely require a complete replacement of the current device. Increased light production could come through an increase of the scintillator bar thickness, or a different choice of scintillator material with a higher light yield and shorter decay time such as EJ-204. Improved photodetectors, including Microchannel Plate PMTs, which also perform well in high magnetic field environments, could provide higher gain and better efficiency than the current SiPMs, and will be investigated to assess their potential impact on the ST performance.

The GLUEX BCAL is a scintillating fiber calorimeter, which provides timing information for both neutral and charged particles. The measured time resolution of the BCAL for charged particles depends on the reconstructed BCAL energy but had an average value of  $\sim 220$  ps during the GLUEX Spring 2017 run period. For charged particles with large scattering angles ( $11^\circ < \theta < 120^\circ$ ) this additional measure of the interaction time will improve the overall  $K_L$  time resolution when combined with the ST measurement. The GLUEX TOF is composed of two planes of 2.5 cm thick scintillator bars. The measured TOF time resolution was 100 ps from the GLUEX Spring 2017 run period, well below the assumed performance of the ST. Therefore, for reactions with a charged particle, which is produced in the forward region  $\theta < 11^\circ$ , the TOF will be used to provide a better  $K_L$  momentum determination than the ST.

To summarize, The simulation studies in this proposal (See Sec. 11) have assumed a time resolution



of 150 ps, which is adequate for the proposed physics program. With the current detector, the overall  $K_L$  momentum resolution will be determined by utilizing the timing information from the ST, BCAL and TOF detectors to ensure that the 150 ps specification is achieved. Finally, we are exploring potential upgrades to improve the ST time resolution significantly; however, further study is required to understand the impact of such improvements on the extracted resonance parameters for the proposed hyperon spectroscopy program.

### 10.1.7 Measurement of $K_L$ Flux

The  $K_L$  has four dominant decay modes [2]:

1.  $K_L \rightarrow \pi^+\pi^-\pi^0, BR = 12.54 \pm 0.05\%$ .
2.  $K_L \rightarrow \pi^0\pi^0\pi^0, BR = 19.52 \pm 0.12\%$ .
3.  $K_L \rightarrow \pi^\pm e^\mp \nu_e, BR = 40.55 \pm 0.11\%$ .
4.  $K_L \rightarrow \pi^\pm \mu^\mp \nu_\mu, BR = 27.04 \pm 0.07\%$ .

In addition, there are several rare decay modes, including the CP-violating  $K_L \rightarrow 2\pi$  mode. In three of the four principal decay modes of the  $K_L$ , two charged particles are emitted. To measure the flux of the  $K_L$  beam at GlueX, we will measure the rate of  $K_L$  decays to two oppositely charged tracks in the Hall D Pair Spectrometer [133] upstream of the GlueX cryotarget. Timing information from the pair spectrometer will be used to estimate time of flight elapsed between the creation of a  $K_L$  in the Be target and its decay to measure momenta of decayed kaons. In a long run with high statistics, the  $2\pi$  decay mode can also be used for a reference to measure independently the flux and momenta of decayed kaons and reconstruct the flux of incoming kaons. This experiment will employ techniques similar to those used in the most precise measurements of  $K_L$  flux (see, for example, Refs. [123, 134, 135]).

For the measurement of the  $K_L$  flux, we can use regeneration of  $K_S$  and detecting  $\pi^+\pi^-$  pairs in Pair Spectrometer as it was done at Daresbury (see Ref. [76] and references therein).

A measurement of the  $K_L$  flux at the 5% level may require additional instrumentation, but in general is not essential to the proposed physics program.

## 10.2 LH<sub>2</sub>/LD<sub>2</sub> Cryotarget for Neutral Kaon Beam at Hall D

The proposed experiment will utilize the existing GlueX liquid hydrogen cryotarget (Fig. 24) modified to accept a larger diameter target cell [136]. The GlueX target is comprised of a kapton cell containing liquid hydrogen at a temperature and pressure of about 20 K and 19 psia, respectively. The 100 ml cell is filled through a pair of 1.5 m long stainless steel tubes (fill and return) connected to a small container where hydrogen gas is condensed from two room-temperature storage tanks. This condenser is cooled by a pulse tube refrigerator with a base temperature of 3 K and cooling power of about 20 W at 20 K. A 100 W temperature controller regulates the condenser at 18 K.

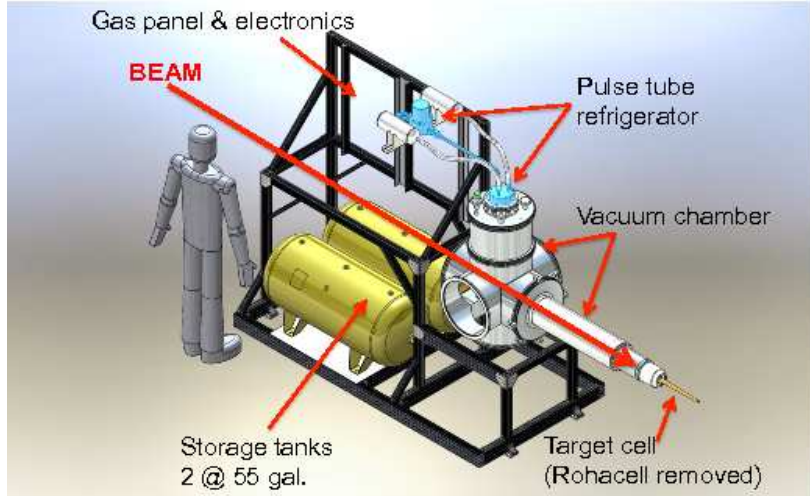


Figure 24: The GlueX liquid hydrogen target.

The entire target assembly is contained within an "L"-shaped stainless steel and aluminum vacuum chamber with a Rohacell extension surrounding the target cell. The Start Counter for the GlueX experiment fits snugly over this extension. The vacuum chamber, along with the hydrogen storage tanks, gas handling system, and control electronics, is mounted on a custom-built beamline cart for easy insertion into the Hall D solenoid. A compact I/O system monitors and controls the performance of the target, while hardware interlocks on the target temperature and pressure and on the chamber vacuum ensure the system's safety and integrity. The target can be cooled from room temperature and filled with liquid hydrogen in about 5 hours. For empty target runs, the liquid can be boiled from the cell in about 20 minutes (the cell remains filled with cold hydrogen gas), and then refilled with liquid in about 40 minutes.

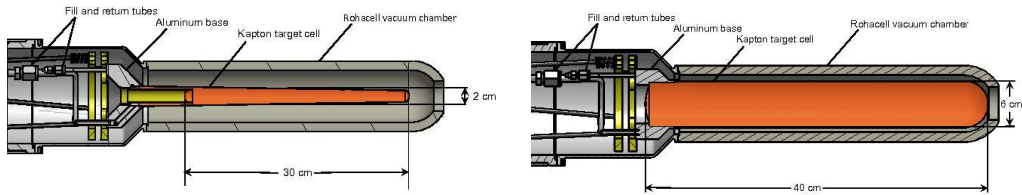


Figure 25: Left plot: Kapton target cell for the GlueX  $\text{LH}_2/\text{LD}_2$  target. Right plot: Conceptual design for a larger target cell for the proposed  $K_L$  beam in Hall D.

The GlueX cell (Fig. 25) is closely modeled on those utilized in Hall B for more than a decade and is a horizontal, tapered cylinder about 38 cm long with a mean diameter of 2 cm. The cell walls are  $130 \mu\text{m}$  kapton glued to an aluminum base. A 2 cm diameter reentrant beam window defines the length of  $\text{LH}_2/\text{LD}_2$  in the beam to be about 30 cm. Both entrance and exit windows on the cell are  $75 \mu\text{m}$  kapton. In normal operation, the cell, the condenser, and the pipes between them are all filled with liquid hydrogen. In this manner the liquid can be subcooled a few degrees below the vapor pressure curve, greatly suppressing bubble formation in the cell. In total, about 0.4 liter of  $\text{LH}_2$  is condensed from the storage tanks, and the system is engineered to recover this quantity of

hydrogen safely back into the tanks during a sudden loss of insulating vacuum, with a maximum allowed cell pressure of 49 psia [137].

A conceptual design for the neutral kaon beam target is also shown in Fig. 25. The proposed target cell has a diameter of 6 cm and a 40 cm length from entrance to exit windows, corresponding to a volume of about 1.1 liter, which will require filling the existing tanks on the target cart to about 50 psia. The collaboration will work with the JLab Target Group to investigate alternative materials and construction techniques to increase the strength of the cell. As an example, the LH<sub>2</sub> target cell recently developed for Hall A is 6.3 cm in diameter, 18 cm long and has a wall thickness of approximately 0.2 mm. The cell is machined from a high-strength aluminum alloy, AL7075-T6, and has a maximum allowed pressure of about 100 psia. It is expected that minor modifications to the cryotarget's piping systems will also be required to satisfy the increased volume of condensed hydrogen.

The proposed system is expected to work equally well with liquid deuterium, which condenses at a slightly higher temperature than hydrogen (23.3 K versus 20.3 K at atmospheric pressure). The expansion ratio of LD<sub>2</sub> is 13% higher, which implies a storage pressure of about 60 psia. Therefore, the new target cell must be engineered and constructed to work with either H<sub>2</sub> or D<sub>2</sub>.

## 11 Running Condition

### 11.1 Event Identification, Reconstruction, Acceptances

The  $K_L$  beam is generated by sampling the momentum distribution of  $K_L$  particles coming from the decays of  $\phi$  mesons produced by interactions of a photon beam with a beryllium target 16 m upstream of the LH<sub>2</sub>/LD<sub>2</sub> cryotarget. The  $K_L$  beam profile was assumed to be uniform within a 3 cm radius at the LH<sub>2</sub>/LD<sub>2</sub> cryotarget. Due to the very strong  $t$ -dependence in the  $\phi$  photoproduction cross section [138] and the  $P$ -wave origin of the  $\phi \rightarrow K_L K_S$  decay, the majority of kaons will be produced at very small angles. In the simulation studies discussed in this section, we assume a flux of  $3 \times 10^4 K_L/s$  on a 40 cm long LH<sub>2</sub> target for a beamtime of 100 PAC days.

#### 11.1.1 Simulations and Reconstruction of Various Channels Using GlueX Detector

The GlueX detector is a large acceptance detector based on a solenoid design with good coverage for both neutral and charged particles. The detector consists of a solenoid magnet enclosing devices for tracking charged particles and detecting neutral particles, and a forward region consisting of two layers of scintillators (TOF) and a lead-glass EM calorimeter (FCAL). A schematic view of the GlueX detector is shown in Fig. 26. The magnetic field at the center of the bore of the magnet for standard running conditions is about 2 T. The trajectories of charged particles produced by interactions of the beam with the 40-cm LH<sub>2</sub>/LD<sub>2</sub> cryotarget at the center of the bore of the magnet are measured using the Central Drift Chamber (CDC) for angles greater than  $\approx 20^\circ$  with respect to the beam line. Forward-going tracks are reconstructed using the Forward Drift Chambers (FDC). The timing of the interaction of the kaon beam with the LH<sub>2</sub> cryotarget is determined using signals

from the ST, an array of 30 mm thin (3 mm thick) scintillators enclosing the target region. Photons are registered in the central region by the Barrel Calorimeter (BCAL). Detector performance and reconstructions techniques were evaluated during the main GlueX program. Details can be found elsewhere [139].

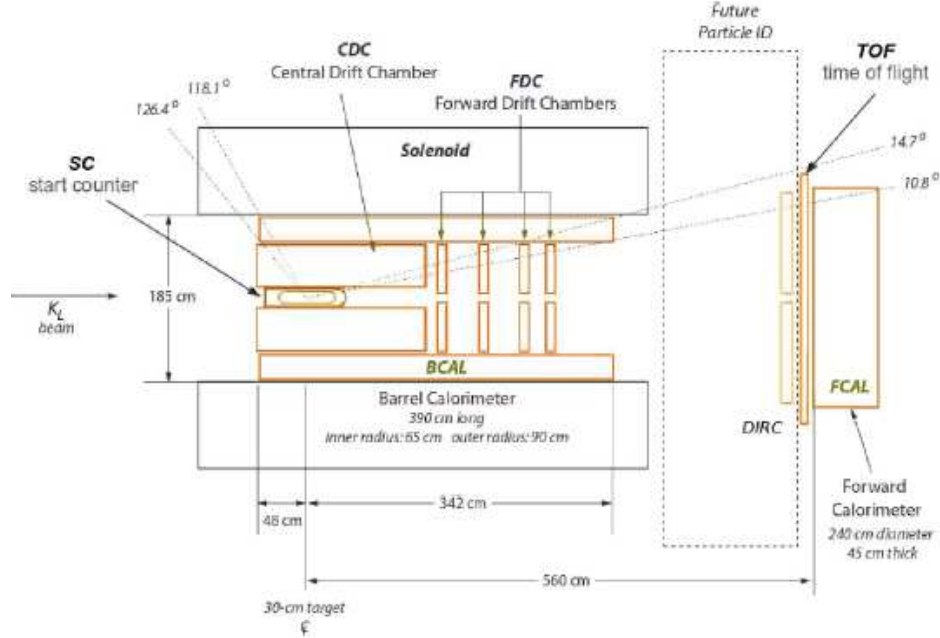


Figure 26: Schematic view of the GlueX detector.

This section describes some simulations of events generated by  $K_L$  beam particles interacting with a  $\text{LH}_2/\text{LD}_2$  cryotarget at the center of the solenoid [140]. The GlueX detector is used to detect one or all of the final-state particles. We will be focusing on a few of the simple two-body reactions, namely  $K_L p \rightarrow K_S p$ ,  $K_L p \rightarrow \pi^+ \Lambda$ ,  $K_L p \rightarrow K^+ \Xi^0$ , and  $K_L p \rightarrow K^+ n$ .

For each topology, one particle (the proton for the  $K_S p$  channel, the  $\pi^+$  for the  $\pi^+ \Lambda$  channel and the  $K^+$  for the  $K^+ \Xi^0$  channel) provides a rough determination for the position of the primary vertex along the beam line that is used in conjunction with the ST to determine the flight time of the  $K_L$  from the beryllium target to the hydrogen target. Protons, pions, and kaons are distinguished using a combination of  $dE/dx$  in the chambers and time-of-flight to the outer detectors (the Barrel Calorimeter (BCAL) and two layers of scintillators (TOF)). See Appendix A4 (Sec. 16) for further details.

### 11.1.2 $K_L p \rightarrow K_S p$ Reaction

The total production cross section, shown in Fig. 27, is reasonably large; however, for the differential cross section there is a fair amount of tension in the existing data sets between different measurements, and the angular coverage in some bins is sparse. Figure 28 shows the existing differential cross-section data for several bins in  $W$ . The cross section as a function of  $\cos \theta_{CM}$  was

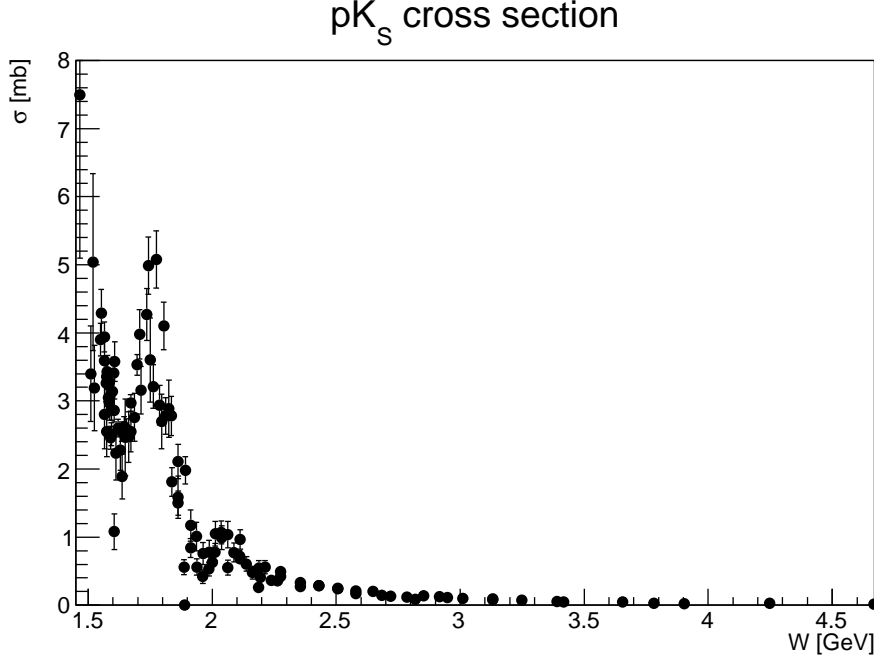


Figure 27: Total cross section for  $K_L p \rightarrow K_S p$  as a function of  $W$ . The measured points are from [141] and references therein.

parametrized using a set of Legendre polynomials (blue curves in Fig. 28); the weights of each polynomial in the set depended on  $W$ . This parametrization was used to generate  $K_L p \rightarrow K_S p$  events that were passed through a full Geant3-based Monte Carlo of the GlueX detector. The final-state particles were constructed using the standard GlueX reconstruction code. We reconstructed the  $K_S$  in its  $\pi^+\pi^-$  channel. More details about the reconstruction of this channel can be found in Appendix A5 (Sec. 17.1.1). Estimates for statistical errors in the measured cross section for 100 days of running at  $3 \times 10^4$   $K_L/s$  as a function of  $\cos \theta_{CM}$  for several values of  $W$  are shown in Fig. 29. We estimate that for  $W < 3$  GeV with an incident  $K_L$  rate of  $3 \times 10^4/s$  on a 40-cm long LH2 target, we will detect on the order of 8M  $K_S p$  events in the  $\pi^+\pi^-$  channel.

### 11.1.3 $K_L p \rightarrow \pi^+ \Lambda$ Reaction

The  $K_L p \rightarrow \pi^+ \Lambda$  and  $K_L p \rightarrow \pi^+ \Sigma^0$  reactions are key to studying hyperon resonances - an analog of  $N\pi$  reactions for the  $N^*$  spectra. They are also the key reaction to disentangling the weak exchange degeneracy of the  $K^*(892)$  and  $K^*(1420)$  trajectories. (A general discussion is given in Sections 13 and 9). The first measurement of this reaction was performed at SLAC in 1974 [142] for  $K_0$  beam momentum range between 1 GeV/c to 12 GeV/c, which is shown in Fig. 30. The total number of  $\pi^+ \Lambda$  events was about 2500 events, which statistically limits the measurement.

Figure 31 shows our estimate of the statistical uncertainty of the  $\pi^+ \Lambda$  total cross section as a function  $K_L$  beam momentum. We kept the same momentum bin size as the one from the SLAC data. The box-shaped error bars in the MC points (red triangles) were increased by a factor of

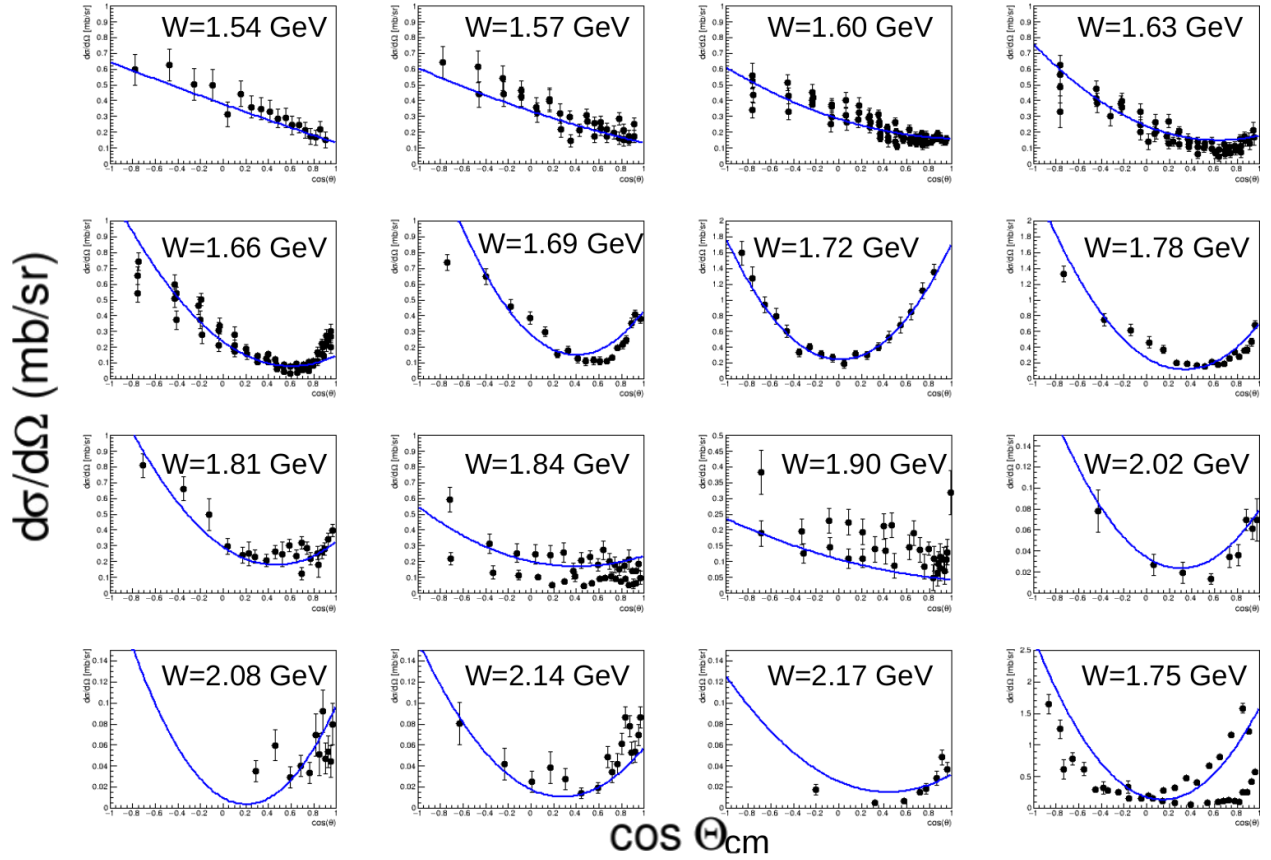


Figure 28: Differential cross-section plots for  $K_L p \rightarrow K_S p$  as a function of  $W$ . The blue curves are the result of a parametrization of the cross section in terms of Legendre polynomials. The measured points are from [141].



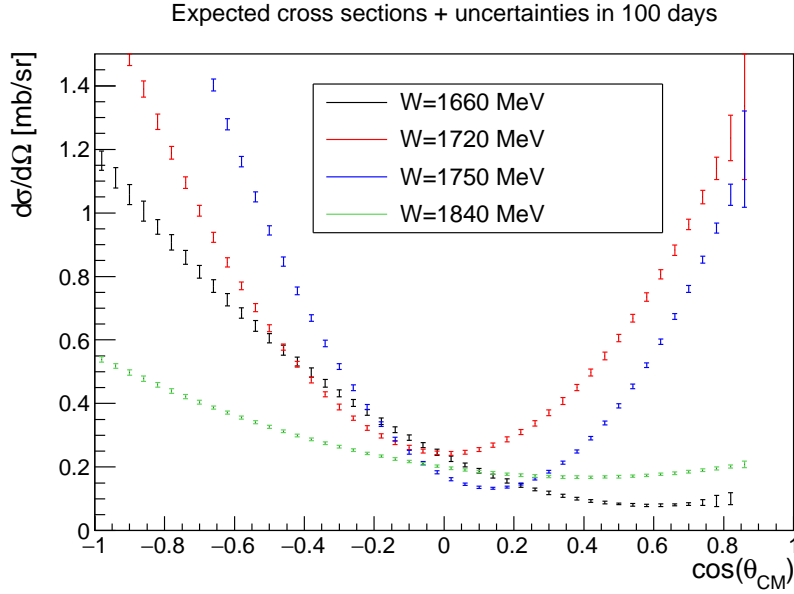


Figure 29: Reconstructed  $K_{LP} \rightarrow K_{SP}$  differential cross sections for various values of  $W$  for 100 days of running.

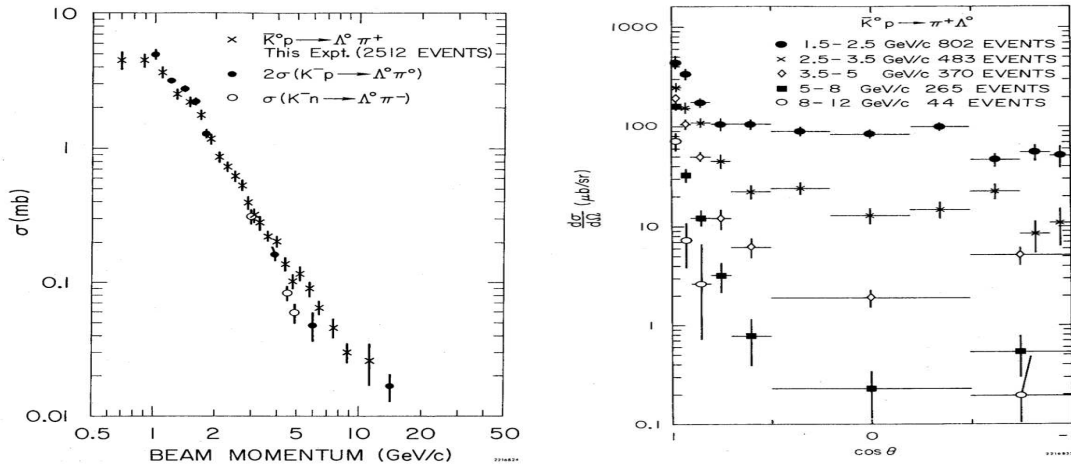


Figure 30: The total cross section for  $K_{LP} \rightarrow \pi^+\Lambda$  reaction as a function of beam momentum [142] (left) and the differential cross sections for various beam momentum ranges.

10 for comparison with the SLAC data. The proposed measurements will provide unprecedented statistical accuracy to determine the cross section for a wide range of  $K_L$  momentum.

#### 11.1.4 $K_{LP} \rightarrow K^+\Xi^0$ Reaction

The study of cascade data will allow us to place stringent constraints on dynamical coupled-channel models. It was recently found in  $N^*$  spectroscopy that many  $N^*$  resonances do not couple strongly



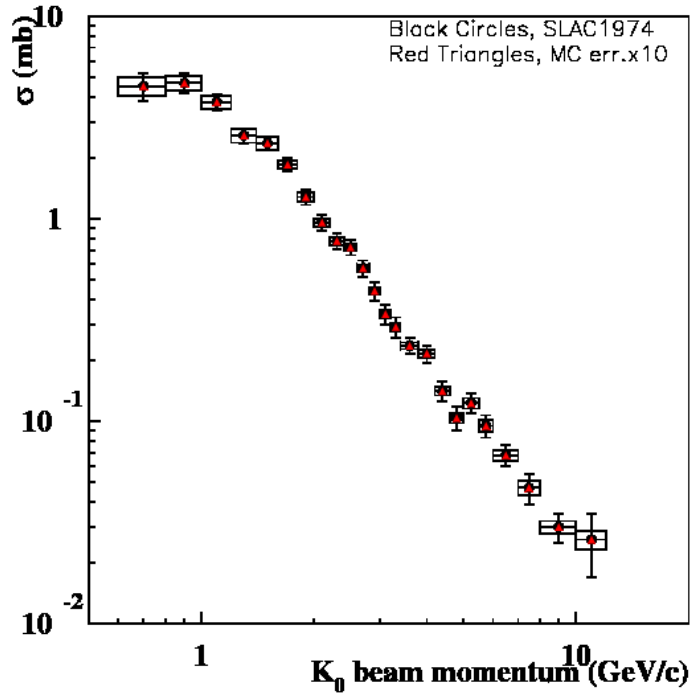


Figure 31: The total cross-section uncertainty estimate (statistical error only) for  $K_L p \rightarrow \pi^+ \Lambda$  reaction as a function of  $K_L$  beam momentum in comparison with SLAC data [142]. The experimental uncertainties have tick marks at the end of the error bars. The box-shaped error bars in the MC points were increased by a factor of 10.

to a  $N\pi$  channel, but are nicely seen in  $K\Lambda$  and  $K\Sigma$  channels. The corresponding situation in hyperon spectroscopy lead to many  $\Lambda^*$  and  $\Sigma^*$  resonances decaying preferably to a  $K\Xi$  channel, see Appendix A1 13 for details. In addition, cascade data will provide us with long-sought information on missing excited  $\Xi$  states and the possibility to measure the quantum numbers of the already established  $\Xi(1690)$  and  $\Xi(1820)$  from a double-moments analysis. The expected large data sample will allow us to determine the induced polarization transfer of the cascade with unprecedented precision, which will place stringent constraints on the underlying dynamics of the reaction. Polarization measurements of hyperons shed light on the contribution from individual quarks to the overall polarization of these states. The polarization of the ground-state cascade can be measured from its weak decay in a straightforward way. With a  $K_L$  beam, the study of the reaction  $K_L p \rightarrow K^+ \Xi^0$  is quite simple and an unprecedented statistical sample can be easily obtained. The statistical uncertainty obtained for 2-fold differential polarization observables with 100 days of beam time ( $\sim 3 \times 10^5$  reconstructed events) is of the order of 0.05-0.1, which is more than an order of magnitude smaller from existing measurements, allowing precision tests on the underlying dynamics to be performed.

Several topologies can be used to reconstruct  $K_L p \rightarrow K^+ \Xi^0$  events, thereby enhancing the available statistics. The biggest contribution results from requiring the reconstruction of only the  $K^+$  in the final state and reconstructing the reaction using the missing-mass technique. The  $\Xi^0$  decays

almost 100% of the time to  $\pi^0\Lambda$ . By utilizing the large branching ratios for  $\Lambda \rightarrow \pi^-p$  and  $\pi^0 \rightarrow \gamma\gamma$  decays, we can also fully reconstruct the  $\Xi^0$ s in the final state using the four-momenta of the detected final-state particles. Figure 32 shows the expected  $W$  resolution for this reaction, depending on the accuracy of the time-of-flight for 300 ps (black), 150 ps (green), 100 ps (red), and when  $W$  is determined from all detected final-state particles (blue).

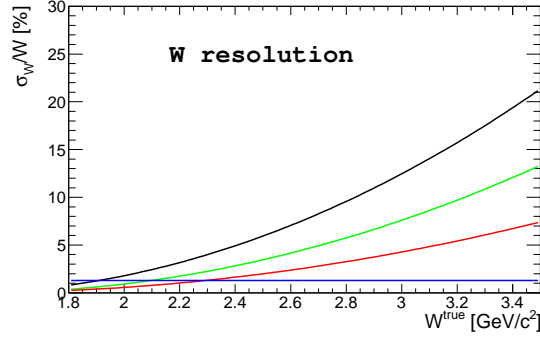


Figure 32:  $W$  resolution of  $\sigma W/W$ , depending on the accuracy of the time-of-flight for 300 ps (black), 150 ps (green), 100 ps (red), and when  $W$  is determined from all detected final-state particles (blue).

In 100 days of beamtime with  $3 \times 10^4 K_L/s$  on the target, we expect  $9 \times 10^6 K_{LP} \rightarrow K^+\Xi^0$  events. From this, the available reconstructed events expected is  $4 \times 10^6$  for Topology 1  $K_{LP} \rightarrow K^+X$ ,  $3 \times 10^5$  for Topology 2  $K_{LP} \rightarrow K^+\Lambda X$ , and  $4 \times 10^4$  for Topology 3  $K_{LP} \rightarrow K^+\Xi^0$ . Figure 33 compares the statistical uncertainties of the total and differential cross sections for the reaction  $K_{LP} \rightarrow K^+\Xi^0$  with existing data taken from [143] for the three different topologies (column 1: only  $K^+$  reconstructed, column 2:  $K^+\Lambda$  reconstructed, and column 3:  $K^+\Xi^0$  reconstructed).

These statistics also allow us to determine the cascade induced polarization by utilizing the fact that the cascade is self-analyzing with an analyzing power of  $-0.406$  [2]. Figure 34 shows the statistical uncertainty estimates of the induced polarization of the cascade by simple fits to the acceptance-corrected yields of the pion angular distribution in the  $\Xi^0$  rest frame.

The main background for this reaction would come from the reactions  $K_{LP} \rightarrow K^+n$  and  $K_{LP} \rightarrow \pi^+\Lambda$ , where the  $\pi^+$  is misidentified as a kaon. The former reaction has an order-of-magnitude higher cross section than  $K_{LP} \rightarrow K^+\Xi^0$ ; however, the  $W$  resolution below  $2.5 \text{ GeV}/c^2$  allows a clean separation of these two reactions. Detection and reconstruction of the  $\Lambda$  places additional constraints that reduce any background contributions significantly. Neutron-induced reactions are not expected to contribute significantly to background and, with missing-mass, invariant-mass, and time-of-flight cuts, such background contributions can be eliminated.

The KL Facility can be utilized to study excited cascade states  $K_{LP} \rightarrow K^+\Xi^*$  with  $\Xi^* \rightarrow \pi\Xi$  and  $\Xi^* \rightarrow \gamma\Xi$ . These excited states should be easily identified and isolated using the missing-mass and invariant-mass techniques. A double-moment analysis can be employed by reconstructing the entire decay chain and establish the spin and parity of these excited states [144].

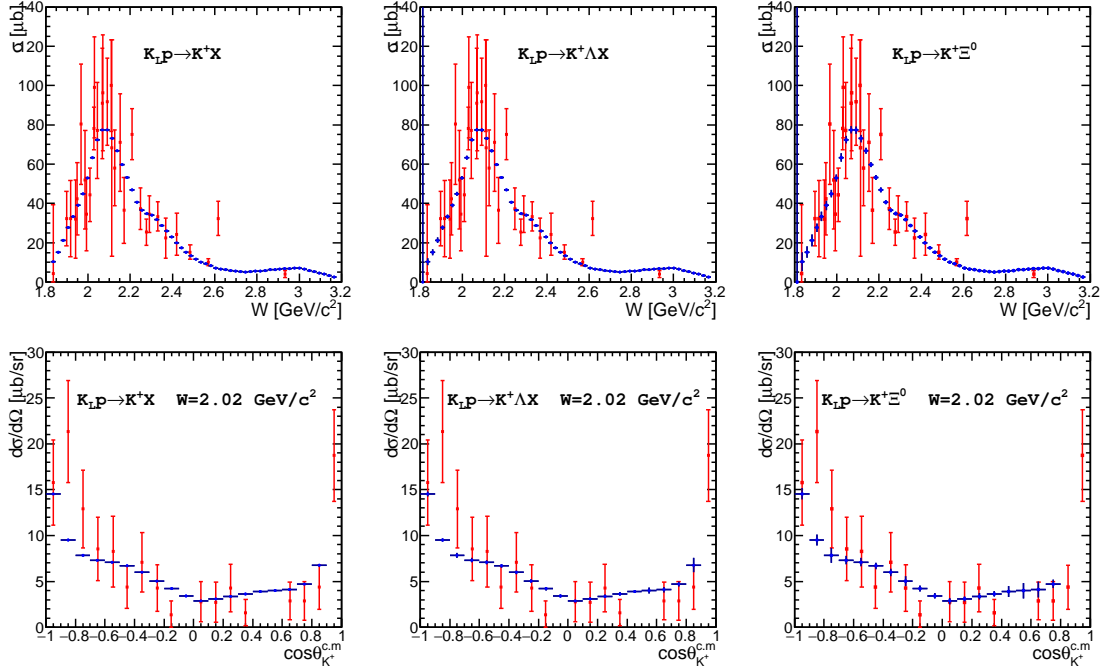


Figure 33: Total and differential cross section statistical uncertainty estimates (blue points) for the three topologies (column 1: only  $K^+$  reconstructed, column 2:  $K^+\Lambda$  reconstructed, and column 3:  $K^+\Xi^0$  reconstructed) in comparison with data taken from Ref. [143] (red points).

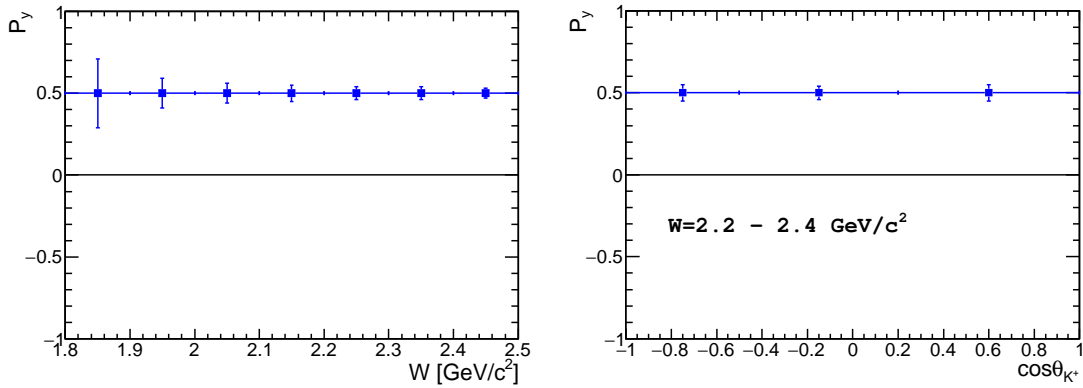


Figure 34: Estimates of the statistical uncertainties of the induced polarization of the cascade as a function of  $W$  (one-fold differential) and  $\cos\theta_{K^+}$  (two-fold differential).

### 11.1.5 $K_L p \rightarrow K^+ n$ Reaction

The  $K_L^0 p \rightarrow K^+ n$  reaction is a very special case in kaon-nucleon scattering. Due to strangeness conservation, formation of intermediate resonances is forbidden for this reaction. The main contribution comes from various non-resonant processes, which can be studied in a clean and controlled way. Similar non-resonant processes can be seen in other reactions where they can interfere with hyperon production amplitudes, causing distortion of the hyperon signals. That is why knowledge

of the non-resonant physical background is important not only for the kaon-induced reactions but for all reactions with strangeness. The non-resonant nature of the reaction does not guarantee the absence of bumps in the total cross section: kaons and/or nucleons can be excited in the intermediate stage, producing bumps in the total cross section.

The reaction  $K_L^0 p \rightarrow K^+ n$  is simple and it has a very high production cross section, see Fig. 35(left); nevertheless, the data on this reaction are scarce. It is a bit simpler to perform a positive kaon beam scattering for the inverse reaction, but the necessity of a neutron target with unavoidable many-body and FSI effects complicates the data analysis. That is why the inverse reaction is also not so well known. A fair amount of differential cross-section data are available in the range  $0.5 < p_{K_L} < 1.5$  GeV/c, predominantly from bubble chambers, see Ref. [145], and there are a few measurements at high momenta:  $p_K = 5.5$  GeV/c [146],  $p_K = 10$  GeV/c [147]. In the energy range  $2 < W < 3.5$  GeV, which can be covered by the KLF experiment with very high statistics, there are no data on this reaction at all.

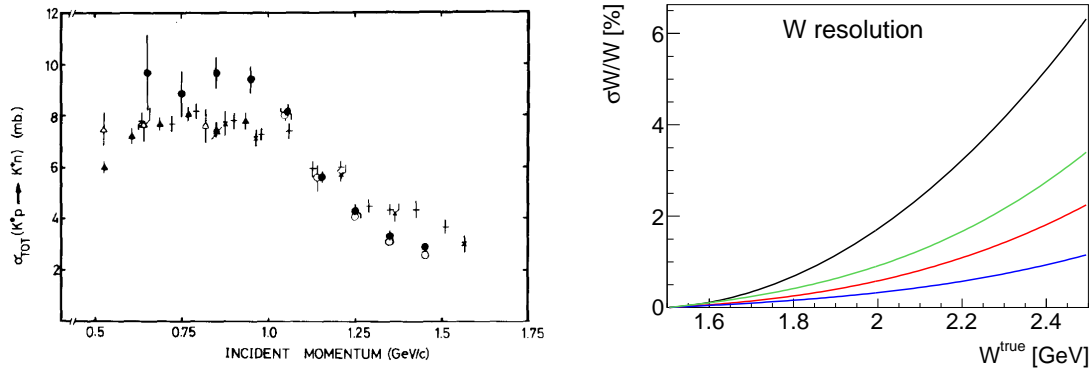


Figure 35: The total cross section for  $K_L p \rightarrow K^+ n$  reaction as a function of  $K_L$  momentum from Ref. [145] (left) and expected  $W$  resolution,  $\Delta W/W$ , depending on time-of-flight accuracy (right) for 300 ps (black), 150 ps (green), 100 ps (red), and 50 ps (blue), respectively.

To reconstruct the reaction fully via missing mass technique it is enough to detect charged kaon. However at higher  $W$ , depending on timing resolution the  $\Delta W$  will blow up, therefore, better timing resolution would be preferable. The Fig. 35(right) shows how the timing resolution affects  $W$  resolution. Future improvements of start counter timing resolution will allow to lower  $W$  resolution further, such that at 150 ps we may get  $\Delta W < 20$  MeV below  $W < 2.2$  GeV, currently this is under the study. The beam energy is determined by TOF technique utilizing the 16-m flight path between the kaon production Be target and the reaction hydrogen target. The beam resolution in this case is driven by the ST time resolution (Sec. 10.1.5). The present ST time resolution leads to a 300 ps vertex time resolution.

In addition to a kaon, one could also detect a neutron; however, due to the poor neutron detection efficiency and the large systematic uncertainties associated with neutron detection we do not expect any improvement in reaction reconstruction in this case.

In 100 days of beamtime with  $3 \times 10^4$   $K_L$ /s on the target, we expect to detect around 200M  $K_L p \rightarrow K^+ n$  events. A typical example of the expected statistics in comparison to previous data

can be seen in Fig. 36(left). The highest flux is expected around  $W = 3$  GeV, where we had to increase statistical errors by a factor of 10 to make them visible, see Fig. 36(right).

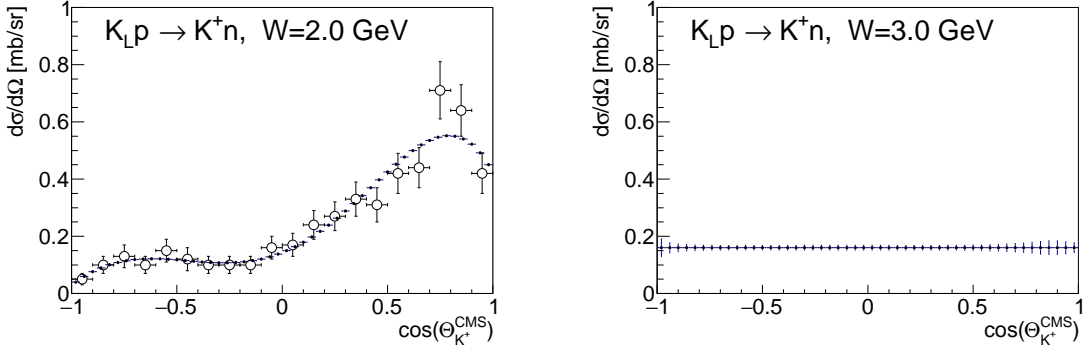


Figure 36: The cross-section uncertainty estimates (statistical only) for  $K_L p \rightarrow K^+ n$  reaction for the  $W = 2$  GeV (left) in comparison with data from Ref. [145] and  $W = 3$  GeV (right) The error bars for the right plot were increased by factor of 10 to make them visible.

There are three major sources of background:  $np \rightarrow K^+ nn$ ,  $np \rightarrow \pi^+ nn$ , and  $K_L p \rightarrow K^+ \Xi^0$ . Neutron flux drops exponentially with energy (see Appendix A4 (Sec. 16) for details) and generally the high-energy neutron flux is small, but nonvanishing. If neutrons and  $K_L$ s have the same speed they cannot be separated by time of flight. Neutron-induced reactions have high cross sections, which is why it is necessary to consider them as a possible source of background. Fortunately, neutron-induced kaon production contributes at the low level of  $10^{-3}$ , which, with missing-mass cuts, can be reduced below  $10^{-4}$ . Some of the pions from  $np \rightarrow \pi^+ nn$  reaction can be misidentified as kaons, but with missing mass and time-of-flight cuts we can reduce the contribution of this background to a sub-per mill level. A detailed description of various backgrounds can be found in Appendix A5 (Sec. 17).  $K_L p \rightarrow K^+ \Xi^0$  has a cross section 100 times smaller than that for  $K_L p \rightarrow K^+ n$ . Below  $W < 2.3$  GeV,  $K_L p \rightarrow K^+ \Xi^0$  can be completely filtered out by a  $3\sigma$   $K^+$  missing-mass cut. At high  $W$ , there is some overlap. One can use conventional background subtraction techniques to eliminate it. The  $\Xi^0$  often has charged particles in its decay chain, which can be used to veto the channel. Our studies show that the background from  $\Xi^0 \rightarrow \pi^0 \Lambda \rightarrow \pi^0 \pi^0 n$  can be reduced below  $10^{-4}$  level as well.

### 11.1.6 Reaction $K_L p \rightarrow K^- \pi^+ p$

#### 1. $I=1/2$ P-wave Phase Shift Analysis

The  $K\pi$   $S$ -wave scattering, below 2 GeV, has two possible isospin channels,  $I = 1/2$  and  $I = 3/2$ . In the same range of mass, the  $P$ -wave has one isospin,  $I = 1/2$ . The  $P$ -wave is a narrow elastic wave peaking at 892 MeV and interpreted as  $K^*(892)$ . The  $I = 3/2$   $S$ -wave is elastic and repulsive up to 1.7 GeV and contains no known resonances. In the  $I = 1/2$   $S$ -wave, a peaking broad resonance appears above 1350 MeV. Moreover, some phenomenological studies [148–152] predict the presence of a resonance with a very large

width in the region close to the  $K\pi$  threshold. The hadroproduction of the  $K\pi$ , using the  $K_L$  facility, provides an adequate environment for studying the  $K^*$  states.

We made a Monte Carlo simulation to study the phase-shift of the  $K\pi$   $P$ -wave in the  $K_L$  facility. The  $K\pi$  production simulation is based on the model given by Estabrooks et al. [96]. The model describes the charged kaon reaction  $K^-p \rightarrow K^-\pi^+n$ . Therefore in this simulation we assume that the cross-section of  $K_L^0p \rightarrow K^-\pi^+p$  is similar to the previous reaction. The model describes the production mechanism in terms of strongly degenerate  $\pi$ - $B$  and  $\rho$ - $A_2$  Regge exchanges and Regge "cuts" that have simple structure in the  $t$ -channel helicity frame. The  $t$ -dependent parametrization of the naturality amplitudes  $L_\lambda^\pm$  for production of a  $K^-\pi^+$  state of invariant mass  $m_{K\pi}$ , center-of-mass (COM) momentum  $q$ , angular momentum  $L$ , and  $t$ -channel helicity  $\lambda$ , by natural (+) and unnatural (-) parity exchange, according to [96], is as follows

$$L_0 = \frac{\sqrt{-t}}{m_\pi^2 - t} G_{K\pi}^L(m_{K\pi}, t), \quad (25)$$

$$L_1^- = \sqrt{\frac{1}{2}L(L+1)} G_{K\pi}^L(m_{K\pi}, t) \gamma_c(m_{K\pi}) \exp(b_c(m_{K\pi})(t - m_\pi^2)), \quad (26)$$

$$L_1^+ = \sqrt{\frac{1}{2}L(L+1)} G_{K\pi}^L(m_{K\pi}, t) [\gamma_c(m_{K\pi}) \exp(b_c(m_{K\pi})(t - m_\pi^2)) - 2i\gamma_a(m_{K\pi}) \exp(b_a(m_{K\pi})|t|(t - m_\pi^2))], \quad (27)$$

$$L_\lambda^\pm = 0, \quad \lambda \geq 2, \quad (28)$$

where  $G_{K\pi}^L$  is related to the  $K\pi$  elastic scattering amplitude  $a_L$  by

$$G_{K\pi}^L(m_{K\pi}, t) = N \frac{m_{K\pi}}{\sqrt{q}} a_L(m_{K\pi}) \exp(b_L(m_{K\pi})(t - m_\pi^2)). \quad (29)$$

The parameters  $\gamma_a$ ,  $\gamma_c$ ,  $b_a$ ,  $b_c$  and  $b_L$  were determined by fitting the LASS  $K^-p \rightarrow K^-\pi^+n$  data. The  $K\pi$  scattering amplitudes are the sum of an isospin-1/2 and 3/2 component,

$$a_L = a_L^{I=1/2} + \frac{1}{2} a_L^{I=3/2}, \quad (30)$$

where  $a_L^I$  is described by a relativistic Breit-Wigner.

In this study, we include only the  $P$ -wave component  $K^*(892)$  in the simulation. The number of events for 100 days of running, at  $3 \times 10^4$   $K_L/s$ , in the range of mass  $m_{K\pi} < 1.5$  GeV and negative transfer 4-momentum  $-t < 0.8$  GeV<sup>2</sup>, is expected to be around 2 million events. The  $K_L$  beam energy used in this simulation is equal to 7 GeV. The generated Monte Carlo events, function of the transfer 4-momentum  $-t$  and the invariant mass  $m_{K\pi}$ , is illustrated in Fig. 37, and the phase-shift function of  $m_{K\pi}$  with mass bin width of 10 MeV and  $|t| < 0.5$  GeV<sup>2</sup> is illustrated in Fig. 38.

As one can see experimental data produced by LASS experiment [97] in the mass regions close to the threshold and above 1.3 GeV are poorly measured and therefore do not provide constrains in these regions. However, according to this simulation study, the proposed  $K_L$  facility can provide statistically high precision data, which will significantly constrain the uncertainty of the phase motion in the full range of  $m_{K\pi}$  from the threshold up to 1.5 GeV.

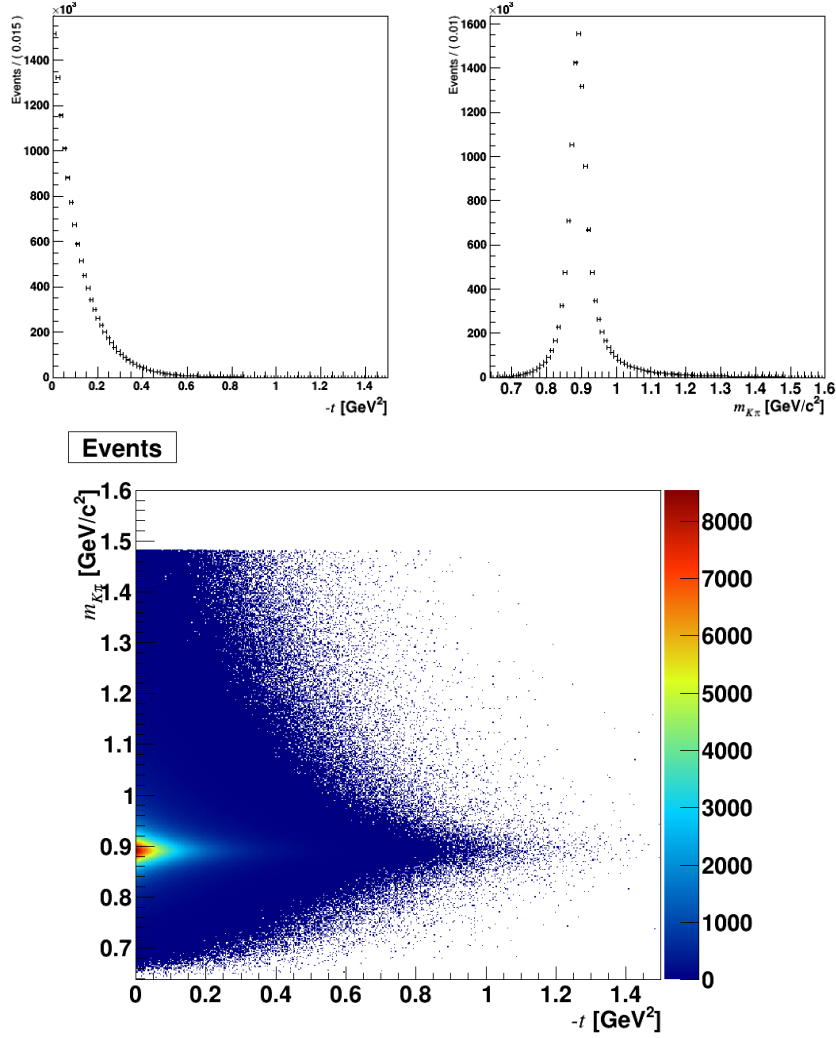


Figure 37: The generated MC events distribution function of  $-t$  (upper left panel);  $m_{K\pi}$  (upper right panel) and  $m_{K\pi}$  vs  $-t$  (lower panel).  $m_{K\pi}$  vs  $-t$  (lower panel).

## 11.2 Summary and Beam Time Request

We propose to perform strange hadron spectroscopy with a secondary  $K_L$  beam in the GlueX setup at JLab. Precise new experimental data (both differential cross sections and recoil polarization of hyperons) for  $K_L p$  scattering with good kinematic coverage will be obtained. This will allow predictions from CQM and LQCD to be checked for all families of excited  $\Lambda^*$ ,  $\Sigma^*$ ,  $\Xi^*$ , and  $\Omega^*$  hyperon resonances for the first time. In addition, it will permit a search for the possible existence of hybrids in the hyperon sector as predicted by the lattice calculations [51].

A complete understanding of three-quark bound states requires accurate measurements of the full spectra of hyperons with their spin-parity assignments, pole positions, and branching ratios. An important impact of these strange hyperon spectroscopy measurements is their significance for the thermodynamic properties of the early universe at freeze-out, which is one of the main physics



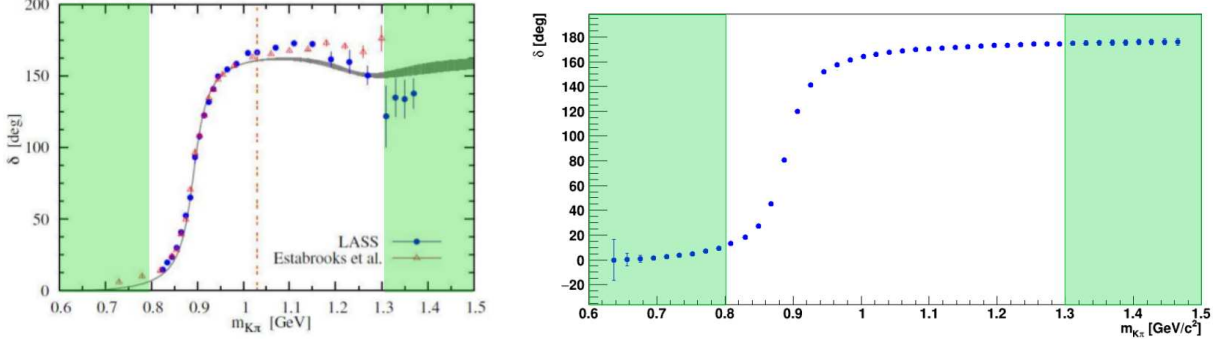


Figure 38: The  $I = 1/2$   $K\pi$  scattering  $P$ -wave phase-shift function of  $m_{K\pi}$ . The left panel shows experimental results from LASS [97] and Estabrooks *et al.* [96]. The gray band represents the fit to the  $\tau$  decay data by Boito *et al.* [112]. On the right panel, we present results of expected measurement for 100 days of running. The statistical errors on the right panel are increased by factor of 10 for a better visibility.

topics at heavy-ion colliders.

Besides hyperon spectroscopy, the experimental data obtained in the strange meson sector in the reactions  $K_L p \rightarrow K^\pm \pi^\mp p$  and  $K_L p \rightarrow K_S \pi^\pm n(p)$  will provide precise and statistically significant data for experimental studies of the  $K\pi$  system. This will allow a determination of quantum numbers of strange meson resonances in S- (including  $\kappa(800)$ ), P-, D-, and higher-wave states. It will also allow a determination of phase shifts to account for final-state  $K\pi$  interactions. Measurements of  $K\pi$  form factors will be important input for Dalitz-plot analyses of  $D$ -meson and charmless  $B$  mesons with  $K\pi$  in final state. These will be important inputs for obtaining accurate an value of the CP-violating CKM matrix element  $V_{us}$  and testing the unitarity relation, in particular through the measurement of the  $\tau \rightarrow K\pi\nu_\tau$  decay rate.

The approval and construction of the proposed facility at JLab will be *unique in the world*. The high-intensity secondary beam of  $K_L$  ( $3 \times 10^4$   $K_L/s$ ) would be produced in electromagnetic interactions using the high-intensity and high-duty-factor CEBAF electron beam with very low neutron contamination as was done at SLAC in the 1970s; but now, with three orders of magnitude higher intensity. The possibility to perform similar studies with charged kaon beams is under discussion at J-PARC with intensities similar to those proposed for the  $K_L$  beam at JLab. If these proposals are approved, the experimental data from J-PARC will be complementary to those of the proposed  $K_L$  measurements.

Below in Table 1, we present the expected statistics for 100 days of running with a  $LH_2$  target in the GlueX setup at JLab. The expected statistics for the 5 major reactions are very large. There are however, two words of cautions at this stage. These numbers correspond to an inclusive reaction reconstruction, which is enough to identify the resonance, but might not be enough to uncover its nature. The need for exclusive reconstruction to extract polarization observables further decrease the expected statistics, e.g., from 4M to **400k** events in the  $K\Xi$  case. These statistics, however, would allow a precise measurement of the double-differential polarization observables with statistical uncertainties on the order of 5–10%. Secondly, kaon flux has a maximum around  $W = 3$  GeV, which decreases rapidly towards high/low  $W$ 's. Thus, the 100 days of beam time on the  $LH_2$  are

essential to maximize the discovery potential of the  $K_L$  Facility and cover the densely populated hyperon regime at low- $W$ .

Table 1: Expected statistics for differential cross sections of different reactions with  $LH_2$  and below  $W = 3.5$  GeV for 100 days of beam time.

| Reaction                          | Statistics<br>(events) |
|-----------------------------------|------------------------|
| $K_L p \rightarrow K_S p$         | 8M                     |
| $K_L p \rightarrow \pi^+ \Lambda$ | 24M                    |
| $K_L p \rightarrow K^+ \Xi^0$     | 4M                     |
| $K_L p \rightarrow K^+ n$         | 200M                   |
| $K_L p \rightarrow K^- \pi^+ p$   | 2M                     |

There are no data on "neutron" targets and, and for this reason, it is hard to make a realistic estimate of the statistics for  $K_L n$  reactions. If we assume similar statistics as on a proton target, the full program will be completed after running 100 days with  $LH_2$  and 100 days with  $LD_2$  targets.

## 12 Cover Letter for KLF Proposal Submission to PAC45

This Proposal follows the Letter of Intent LoI12–15–001, *Physics Opportunities with Secondary  $K_L$  beam at JLab* presented to PAC43 in 2015. The Issues and Recommendations included in the PAC43 Final Report document read as follow:

**Issues:** *It is not clear what this experiment can do that the J-PARC charged kaon program cannot do substantially better. An experimental concern is the transverse size of the KLF beam that must impinge on a 2-3 cm target. Backgrounds from neutrons and  $K_L$  outside the target acceptance may be important in event rates and signal to background rejection.*

**Recommendation:** *Any proposal would require full simulations of the beam line and detector to determine the effect of backgrounds from neutrons and kaons outside the target acceptance. But it is not clear to the committee if this experiment would in any way be competitive with J-PARC or a potential Fermilab or CERN program in this energy range. The superiority of a neutral beam and/or the GlueX detector for these measurements would need to be demonstrated before a future proposal would be considered favorably.*

The KLF Collaboration believes that the current proposal addresses all the concerns following the recommendations expressed by the PAC43:

1. **Q1:** *It is not clear what this experiment can do that the J-PARC charged kaon program cannot do substantially better.*

**A1:** The proposed  $K_L$  beam intensity is similar to the proposed charged kaon beam intensity at J-PARC, so there is no reason to expect that J-PARC will do *substantially better*. Using different probes ( $K_L$  for JLab and  $K^-$  for J-PARC), in principle, we and J-PARC (if charged

kaon beam proposal is approved) will be able to collect data for different reactions. To have full experimental information with different final states is important for coupled-channel analyses to determine hyperon parameters. The JLab and J-PARC measurements will be complementary.

(i) As  $c\tau(K^-) = 3.7$  m, while  $c\tau(K_L) = 15.4$  m, the higher rate of low-momenta kaons with a  $K_L$  beam may be an advantage.

(ii) The proposed experiment will have a  $K_L$  beam with all momenta simultaneously, while J-PARC has to make many thousand different settings to scan the full range of  $W$  distributions in different reactions.

(iii) In the best-case scenario, J-PARC can start a hyperon program in 2024. In Appendix A6 (Sec. 18), we have presented the ability of other possible facilities as FNAL, J-PARC, Belle, BaBar,  $\overline{P}$ ANDA, and COMPASS to do hyperon spectroscopy. We do not see a competition factor here for two reasons: a) some of above-mentioned facilities do not yet have secondary kaon beams; b) even if kaon beams are approved and constructed at these facilities, a hyperon spectroscopy program will not happen before a decade from now.

2. **Q2:** *An experimental concern is the transverse size of the KLF beam that must impinge on a 2-3 cm target. Backgrounds from neutrons and KLF outside the target acceptance may be important in event rates and signal to background rejection.*

**A2:** First of all the collimated beam of  $K_L$  will impinge on the cell of the LH<sub>2</sub>/LD<sub>2</sub> target with  $R = 3$  cm radius. All kaons outside of the solid angle defined by the collimators will be absorbed in a 4 m iron shielding in the sweeping magnet and the concrete shielding in front of the GlueX setup. Second, as was shown by our detailed simulations, the rate of neutrons on the GlueX target at momenta  $p > 1$  GeV/ $c$  is smaller than that of  $K_L$ . On the other hand, production of strange mesons with neutrons at low momenta kinematically cannot occur due to the threshold, because to conserve strangeness at least two final-state kaons have to be produced. Therefore, the physics background from reactions initiated by neutrons is negligible.

The rate of neutrons irradiating GlueX setup outside of the target acceptance will be a total on the level of  $\sim 100$ /s with 90% in the range of energies below 20 MeV, and, therefore, can not cause any background either.

From a radiation point of view, our MCNP6 transport-code calculations have shown that the effect of radiation caused by neutrons is below the RadCon limit.

3. **Q3:** *Any proposal would require full simulations of the beam line and detector to determine the effect of backgrounds from neutrons and kaons outside the target acceptance.*

**A3:** See our answers **A1** and **A2**.

4. **Q4:** *But it is not clear to the committee if this experiment would in any way be competitive with J-PARC or a potential Fermilab or CERN program in this energy range.*

**A4:** See our answer **A1**.

5. **Q5:** *The superiority of a neutral beam and/or the GlueX detector for these measurements would need to be demonstrated before a future proposal would be considered favorably.*

**A5:** Our MC simulations have shown that the proposed experiment will be able to improve

on available world proton target data by three orders of magnitude in statistics. The proposed experiment will provide the first measurements ever on a neutron using LD<sub>2</sub> target. Coupled-channel analyses using both proton and neutron target data promise to find many "missing" hyperons. We will also significantly improve world data on  $K\pi$  PWA with an impact on other fields of particle physics.

The summary of the potential of other facilities is given in Appendix A6 (Sec. 18).

## 13 Appendix A1: Analysis of Three-Body Final States

The understanding of baryon properties is hardly possible without an analysis of reactions with two mesons in the final state. Already in the mass region above 1600 MeV, the excited  $\Lambda$  hyperons decay strongly into the  $\pi\Sigma(1385)$  [153, 154] final state while the  $\Sigma$ -hyperons decay strongly into the  $\pi\Sigma(1385)$  [153] and  $\pi\Lambda(1405)$  [155] channels. Above 1800 MeV almost all known  $\Lambda$  and  $\Sigma$  hyperons have a dominant decay mode defined by production of the vector meson  $K^*(892)$  [154]. In the  $\Sigma$ -sector, a number of resonances were seen in an analysis of the  $\bar{K}\Delta(1230)$  final state. It is natural to expect the decay of  $J^P = 3/2^+$  states into the  $\pi\Lambda(1520)$  [156] channel.

Reactions with two-meson final states provide vital information for the analysis of single-meson production reactions. The singularities that correspond to the opening of the resonance-meson threshold (branching points) can produce structures in other channels that can simulate a resonance-like signal [157, 158]. The situation is notably more severe in the hyperon sector than in the sector of non-strange baryons. Due to the rather small widths of low-mass excited hyperons and meson resonances with an  $s$ -quark, such singularities are situated much closer to the physical region and can notably influence the data. Therefore, a combined analysis of the channels with single and two mesons in the final state is a must in the search for the missing resonances.

The combined analysis should help us to understand the structure of resonances with masses up to 2.5 GeV and their decay properties. One of the important tasks is to find nonet partners of the nucleon states observed in the photo-production reactions in the mass region around 1900 MeV [159]. These states have strong couplings to the  $\rho(770)N$  final state and it is natural to expect that their hyperon partners can be found in an analysis of the  $K^*(892)N$  channel.

The analysis of the three-body final state should be done in the framework of the event-by-event maximum likelihood method, which allows us to take into account all amplitude correlations in the multidimensional phase space. It is very important to extract the polarization observables from the decay of the final hyperons in the  $KN \rightarrow \pi\pi\Lambda$  and  $KN \rightarrow \pi\pi\Sigma$  reactions. One possible simplification is connected with an extraction of the  $K^*(892)N$  state from the  $KN \rightarrow K\pi N$  data, where the analysis can be performed in the framework of the density-matrix-elements approach. However, the analysis should take into account the rescattering of the particles in the final state; e.g., triangle diagrams that lead to logarithmic singularities in the scattering amplitude. Due to the small widths of intermediate states, such singularities can play a more important role than in the case of nucleon and  $\Delta$  excitations. It would be also very important to include in the analysis the CLAS photoproduction data with  $K\pi\Lambda$  and  $K\pi\Sigma$  final states because there is a chance that states with a small  $KN$  coupling could be observed in these reactions.

## 14 Appendix A2: Determination of Pole Positions

In spite of their model dependence, partial-wave Breit-Wigner parameters have for quite some time been the preferred connection between experiment and QCD in hadronic spectroscopy. More recently, however, pole parameters (e.g., pole positions and residues) have justifiably become the preferred connection, and this fact has also been recognized by the Particle Data Group (PDG) in recent editions of the *Review of Particle Physics* [2]. Therefore, the extraction of pole parameters from experimental data becomes a procedure of utmost importance.

Extraction of pole parameters is usually performed in two ways: (a) in an energy-dependent way (ED) or (b) in an energy-independent procedure through single-energy PWAs (SE). In an ED procedure, one measures as many observables as possible to be close to the complete set and then fits the observables with parameters of a well-founded theoretical model that describes the reaction in question. Continuity in energy is enforced by the features of the theoretical model. In a SE procedure, one again measures as many observables as possible but attempts to extract partial waves by fitting energy-binned data independently, therefore, reducing the theoretical input. A discrete set of partial waves is obtained, and the issues of achieving continuity in energy have recently been extensively discussed either by introducing the constraints in analyticity [160] or through angle- and energy-dependent phase ambiguity [161].

In energy-dependent models, pole parameters have been extracted in various ways. The most natural way is the analytic continuation of theoretical model solutions into the complex-energy plane. Simpler single-channel pole extraction methods have been developed such as the speed plot [162], time delay [163], the N/D method [164], regularization procedures [165], and Pade approximants [166], but their success has been limited. In single-energy analyses the situation is even worse: until recently no adequate method has been available for the extraction of pole parameters. All single-channel methods involve first- or higher-order derivatives, so partial-wave data had to be either interpolated or fitted with an unknown function, and that introduced additional and, very often, uncontrolled model dependencies.

That situation has recently been overcome when a new Laurent+Pietarinen (L+P) method applicable to both, ED and SE models, has been introduced [167–171]. The driving concept behind the single-channel (and later multichannel) L+P approach was to replace solving an elaborate theoretical model and analytically continuing its solution into the full complex-energy plane, with a local power-series representation of partial-wave amplitudes having well-defined analytic properties on the real energy axis, and fitting it to the given input. In such a way, the global complexity of a model is replaced by a much simpler model-independent expansion limited to the regions near the real-energy axis, which is sufficient to obtain poles and their residues. This procedure gives the simplest function with known analytic structure that fits the data. Formally, the introduced L+P method is based on the Mittag-Leffler expansion<sup>2</sup> of partial-wave amplitudes near the real-energy axis, representing the regular, but unknown, background term by a conformal-mapping-generated, rapidly converging power series called a Pietarinen expansion<sup>3</sup>. In practice, the regular background

---

<sup>2</sup>Mittag-Leffler expansion [172] is the generalization of a Laurent expansion to a more-than-one pole situation. For simplicity, we will simply refer to this as a Laurent expansion.

<sup>3</sup>A conformal mapping expansion of this particular type was introduced by Ciulli and Fisher [173, 174], was



part is usually fitted with three Pietarinen expansion series, each representing the most general function having a branch point at  $x_{bp}$ , and all free parameters are then fitted to the chosen channel input. The first Pietarinen expansion with branch-point  $x_P$  is restricted to an unphysical energy range and represents all left-hand cut contributions. The next two Pietarinen expansions describe background in the physical range with branch points  $x_Q$  and  $x_R$  defined by the analytic properties of the analyzed partial wave. A second branch point is usually fixed to the elastic channel branch point, and the third one is either fixed to the dominant channel threshold value. Thus, solely on the basis of general physical assumptions about the analytic properties of the fitted process (number of poles and number and position of conformal mapping branch-points) the pole parameters in the complex energy plane are obtained. In such a way, the simplest analytic function with a set of poles and branch points that fits the input is constructed. This method is equally applicable to both theoretical and experimental input<sup>4</sup>

The transition amplitude of the multichannel L+P model is parametrized as

$$T^a(W) = \sum_{j=1}^{N_{pole}} \frac{g_j^a}{W_j - W} + \sum_{i=1}^3 \sum_{k_i=0}^{K_i^a} c_{k_i}^a \left( \frac{\alpha_i^a - \sqrt{x_i^a - W}}{\alpha_i^a + \sqrt{x_i^a - W}} \right)^{k_i}, \quad (31)$$

where  $a$  is a channel index,  $W_j$  are pole positions in the complex  $W$  (energy) plane,  $g_j^a$  coupling constants. The  $x_i^a$  define the branch points,  $c_{k_i}^a$ , and  $\alpha_i^a$  are real coefficients.  $K_i^a$ ,  $i = 1, 2, 3$  are Pietarinen coefficients in channel  $a$ . The first part represents the poles and the second term three branch points. The first branch point is chosen at a negative energy (determined by the fit), the second is fixed at the dominant production threshold, and the third branch point is adjusted to the analytic properties of fitted partial wave.

To enable the fitting, a reduced discrepancy function  $D_{dp}$  is defined as

$$D_{dp} = \sum_a^{all} D_{dp}^a;$$

$$D_{dp}^a = \frac{1}{2 N_W^a - N_{par}^a} \times \sum_{i=1}^{N_W^a} \left\{ \left[ \frac{\text{Re } T^a(W^{(i)}) - \text{Re } T^{a,exp}(W^{(i)})}{Err_{i,a}^{\text{Re}}} \right]^2 + \left[ \frac{\text{Im } T^a(W^{(i)}) - \text{Im } T^{a,exp}(W^{(i)})}{Err_{i,a}^{\text{Im}}} \right]^2 \right\} + \mathcal{P}^a,$$

where

$$\mathcal{P}^a = \lambda_{k_1}^a \sum_{k_1=1}^{K^a} (c_{k_1}^a)^2 k_1^3 + \lambda_{k_2}^a \sum_{k_2=1}^{L^a} (c_{k_2}^a)^2 k_2^3 + \lambda_{k_3}^a \sum_{m=1}^{M^a} (c_{k_3}^a)^2 k_3^3$$

is the Pietarinen penalty function, which ensures fast and optimal convergence.  $N_W^a$  is the number of energies in channel  $a$ ,  $N_{par}^a$  the number of fit parameters in channel  $a$ ,  $\lambda_c^a$ ,  $\lambda_d^a$ ,  $\lambda_e^a$  are Pietarinen

---

described in detail and used in pion-nucleon scattering by Esco Pietarinen [175, 176]. The procedure was denoted as a Pietarinen expansion by Höhler in [80].

<sup>4</sup>Observe that fitting partial-wave data coming from experiment is even more favorable.

weighting factors,  $Err_{i,a}^{\text{Re,Im}}$  . . . errors of the real and imaginary part, and  $c_{k_1}^a, c_{k_2}^a, c_{k_3}^a$  real coupling constants.

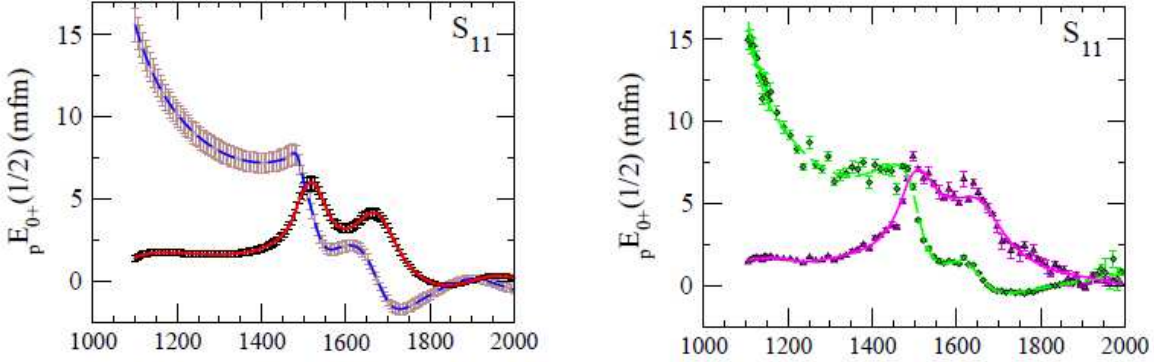


Figure 39: L+P fit to CM12 GWU/SAID pion photoproduction  ${}_pE_{0+}$  ED and SE solutions [177].

In order to obtain reliable answers in the L+P model we have to build knowledge about the analytic structure of the fitted partial wave into the fitting procedure. Because we are looking for poles, we only have to define which branch-points to include. Their analytic form will be determined by the number of Pietarinen coefficients. As we have only three branch-points at our disposal we expect that the first branch-point will describe all subthreshold and left-hand cut processes, the second one is usually fixed to the dominant channel opening, and the third one is to represent background contributions of all channel openings in the physical range. So, in addition to choosing the number of relevant poles, our anticipation of the analytic structure of the observed partial wave is of great importance for the stability of the fit.

The L+P model has been successfully applied to both theoretical models and discrete partial-wave data. As an example, in Fig. 39, we give the achieved quality of the fit for the CM12 GWU/SAID pion photoproduction amplitudes [177].

In summary: Methods of the described L+P model will be used to extract pole parameters for both ED solutions, obtained by the method described in Section 7, and SE solutions developed independently.

## 15 Appendix A3: Statistics Tools for Spectroscopy of Strange Resonances

Several statistical aspects concerning the analysis of  $K_L$  data are discussed in the following. The proposed experiment will be capable of producing a large body of consistent data, which is a pre-



requisite to carry out statistical analyses. So far, the data in the strangeness  $S = -1$  sector were produced in many different experiments, often from the 1980s or earlier, with different systematic uncertainties that are, moreover, unknown in many cases. The problems resemble the situation in pion-induced inelastic reactions [178, 179]. This makes any kind of analysis difficult but statistical tests, e.g., on the significance of a claimed resonance signal, are indispensable to carry out meaningful baryon spectroscopy. Indeed, the search for *missing resonances* is not only a problem of implementing physical principles such as unitarity in the amplitude but also, to a large extent, a statistical one. This becomes especially relevant once one searches for states beyond the most prominent resonances.

## 15.1 Minimizing Resonance Content

Partial-wave analysis, discussed in Section 7 is needed to extract the physically relevant information from data. For resonance spectroscopy, one needs the energy dependence of the amplitude to determine resonance positions and widths. Therefore, energy-dependent (ED) parametrizations of the partial waves are fitted either to data or to single-energy (SE) solutions, generated by conducting partial-wave analysis in narrow energy bins. The resonance content is usually determined by speed-plot techniques or analytic continuation of the ED parametrization to complex scattering energies, where resonances manifest themselves as poles [180].

Yet, the ED parametrization itself contains, almost always, resonance plus background terms in one implementation or another. A problem arises if resonance terms are needed to model missing background dynamics. Then, false positive resonance signals could be obtained [157]. Adding resonance terms will always lower the  $\chi^2$  in a given fit, but the question is how significant this change is.

We plan to address this well-known, yet poorly addressed problem by applying several statistical analysis tools to the amplitude parametrization. Some techniques have been used, so far, to address this problem. For example, in so-called mass scans, the  $\chi^2$  dependence on the mass of an additional resonance is studied [181, 182]. If  $\chi^2$  drops by a certain amount at a given energy, potentially in several reaction channels at once, then a resonance might be responsible.

Beyond mass scans, there exist *model selection* techniques referring to the process of selecting the simplest model with the most conventional explanation. Here, the conventional/simple explanation is an (energy-dependent) background and/or threshold cusps, while the algorithm should penalize unconventional explanations such as resonances.

Minimizing the resonance content in a systematic way is thus a goal within partial-wave analysis. For this, the Least Absolute Shrinkage and Selection Operator (LASSO) technique for model selection can be applied (which provides a Bayesian posterior-mode estimate), in combination with cross validation and/or information theory to control the size of the penalty parameter  $\lambda$  [183–185]. The combination of these techniques effectively suppresses the emergence of resonances except for those really needed by the data. The numerical implementation is especially simple because it affects only the calculation of the  $\chi^2$ . Trial-and-error techniques, sometimes still applied to check for resonances in different partial waves, will become obsolete. Here, one simply starts with an

over-complete resonance set plus flexible backgrounds, and the algorithm will remove all those resonances not needed by data, without manual intervention. Apart from cross validation, we will also consider information theory to regulate  $\lambda$  as proposed in Ref. [186]. In particular, the Akaike and Bayesian information criteria provide easy-to-use model selection. Results should be independent of the choice of the criterion.

In 2017, the LASSO technique was, for the first time, used in pion photoproduction at low energies for the "blindfolded" selection of the relevant multipoles and their simplest parametrization to describe the available data [187]. The analysis of kaon-induced reactions is closely related. For a recent application in a different but related context see Ref. [188]. Once the model selection process is finished, uncertainties on resonance parameters can be obtained by the usual re-sampling techniques.

The existing and proposed partial-wave analysis tools use different construction principles: resonances are included in the form of bare states,  $K$ -matrix poles, or generated from hadron dynamics itself. For the first two classes of approaches, one has at one's disposal the coupling constants that tune the interaction of a bare singularity with the meson-baryon continuum. Those are fit parameters that can be explicitly included in the penalty term. If resonances are generated from the meson-baryon dynamics itself, the case is a bit more complicated, because there are no directly accessible tuning parameters. This parametrization, practiced by the GW/SAID group for many years (see, e.g., Ref. [177]), is, in principle, the cleanest analysis tool, because resonance generation does not require manual intervention. Yet, even here the emergence of resonance terms can be penalized, e.g., through the value of contour integrals on the second Riemann sheet where resonance poles are located (a value of zero corresponds then to the absence of poles).

It should be stressed that the information theory criteria do *not* require a good fit in a frequentist's sense because they merely compare the relative quality of models. This is especially relevant when it comes to the analysis of many different data sets (such as kaon-induced reactions) in which, e.g., the systematic errors might be underestimated such that a  $\chi^2/\text{d.o.f.} \approx 1$  is difficult to achieve.

Systematic uncertainties can be treated as in the GW/SAID approach [81] in which the  $\chi^2$  is defined as

$$\chi^2 = \sum_i \left( \frac{N\Theta_i - \Theta_i^{\text{exp}}}{\epsilon_i} \right)^2 + \left( \frac{N-1}{\epsilon_N} \right)^2, \quad (32)$$

where  $\Theta_i^{\text{exp}}$  is an experimental point in an angular distribution and  $\Theta_i$  is the fit value. Here the overall systematic error,  $\epsilon_N$ , is used to weight an additional  $\chi^2$  penalty term due to renormalization of the fit by the factor  $N$ . The statistical error is given by  $\epsilon_i$ . Note that the fit function is penalized, rather than the data, to avoid the bias discussed in Ref. [189]. See also Ref. [190] for further discussion of this topic.

## 15.2 Goodness-of-Fit Tests

The  $\chi^2$  per degree of freedom,  $\chi_{d.o.f.}^2$ , is usually considered as a criterion for a good fit, but becomes meaningless if thousands of data points are fitted (and should be replaced by Pearson's  $\chi^2$  test). Statistical  $\chi^2$  tests will become possible through the new data, putting resonance analysis on a

firmer ground. While  $\chi^2$  tests are sensitive to under-fitting, they are insensitive to over-fitting. Here, the  $F$ -test [191] is suitable to test the significance of new fit parameters. That test, can, thus, be applied to reduce the number of internal parameters in a partial-wave parametrization, which results in more reliable estimates of uncertainties for extracted resonance parameters such as masses, widths, and branching ratios.

With increased consistency of data through the KLF experiment, other goodness-of-fit criteria can also be applied, such as Smirnov-Kolmogorov or Anderson-Darling tests for normality [192, 193] or run tests from non-parametric statistics. For pion photoproduction, these tests are applied and extensively discussed in Ref. [187].

A prerequisite to carry out classical statistical tests is data consistency. As discussed before, this is unfortunately not always the case in the  $S = -1$  sector. The proposed KLF measurements will produce, for the first time, a body of data large enough to enable such tests reliably.

### 15.3 Representation of Results

As mentioned, ED parametrizations are needed to extract resonance parameters, but single-energy (SE) fits are useful to search for narrow structures, or for other groups to test theoretical models of hadron dynamics. The question arises how the partial waves can be presented to allow the theory community to carry out their fits. As recently demonstrated [194], SE solutions alone carry incomplete statistical information, mainly because they are correlated quantities. We plan to provide the analysis results in a similar form as recently done in Ref. [194] for elastic  $\pi N$  scattering. With this, the theory community can fit partial waves through so-called *correlated*  $\chi^2$  fits obtaining a  $\chi^2$  close to the one obtained in a fit directly to data (see Ref. [194] for an extended discussion). This format ensures that the maximal information from experiment is transmitted to theory, allowing to address the *missing resonance problem* in the wider context of questions related to confinement and mass generation, that have been paramount problems in hadronic physics for decades.

In summary: With a large consistent data set from the KLF experiment, an entire class of statistical tools will become applicable that is needed to conduct rigorous baryon spectroscopy. With the new data, the quantitative significance of resonance signals and the quantitative uncertainties of resonance parameters can be determined.

## 16 Appendix A4: Neutron Background

Overall, our MC simulations for 12 GeV (Fig.18(left)) agreed quite well with the neutron yields measurements that SLAC did for 16 GeV (Fig. 18(right)). Note that with a proton beam, the  $n/K_L$  ratio is  $10^3 - 10^4$  (see, for instance, Table 2 in Appendix A6 (Sec. 18), while in the JLab case, this ratio is less than 10, as Fig. 40 shows.

For MCNP6 calculations, several neutron tallies were placed along the beam and at the experimental hall ceiling for neutron fluence estimation. Calculations were performed for different shielding

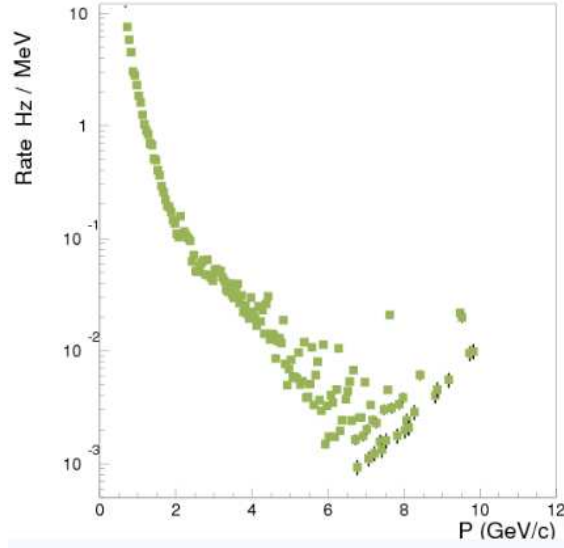


Figure 40: The  $n$  to  $K_L$  ratio associated with Fig. 18(left).

modifications in the beam cave to optimize the neutron dose. Figures 41, 42, and 43 present the vertical cross section of the neutron flux evolved from beginning to final configurations considered in the course of this study. Neutron flux in experimental hall was evaluated for several shielding configurations in the beam cave. First, the shielding wall was located at the end of the beam cave; see Fig.41. Second, the shielding wall is located as close as possible to the first collimator in the beam cave, Fig. 42. Also, two labyrinths were introduced into the MCNP model, Fig. 42, to check their influence on anticipated dose rate. No influence was observed for proper designed labyrinths with no direct view from experimental hall to the source target in the beam cave. Third, the same configuration as in Fig. 42, but second shielding wall is added at half way toward to the end of the beam cave, Fig.43

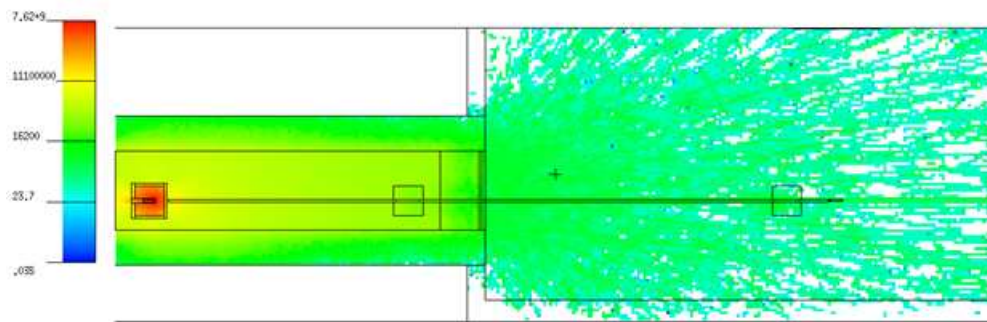


Figure 41: Vertical cross section of the neutron flux calculated for the model where the shielding wall is located at the end of the beam cave.

The energy distribution of neutrons emitted from the Be target (in  $N/(MeV \cdot s \cdot cm^2)$  units) is shown in Fig. 44.

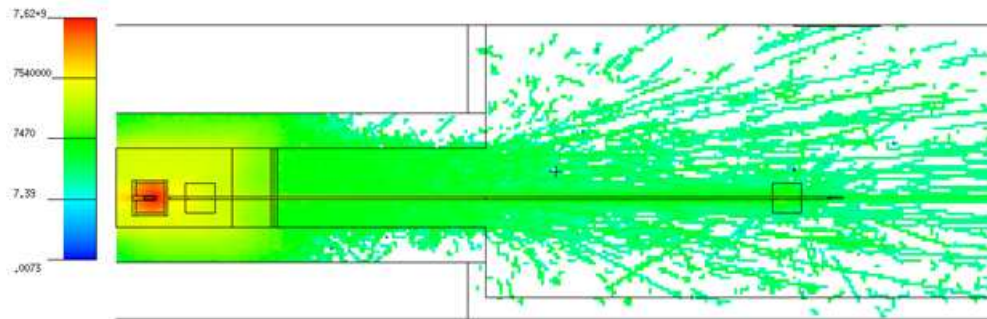


Figure 42: Vertical cross section of the neutron flux calculated for the model where the shielding wall is located as close as possible to the first collimator in the beam cave.

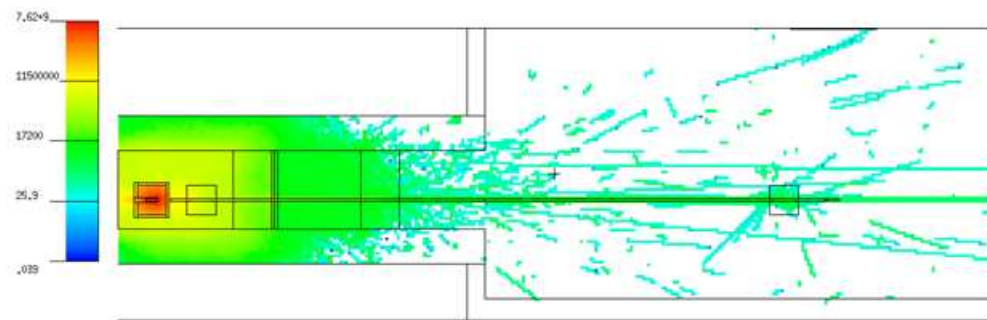


Figure 43: Vertical cross section of the neutron flux calculated for the model where the first shielding wall is located as close as possible to the first collimator and Be-target and the second shielding wall is located at halfway toward to the end of the beam cave.

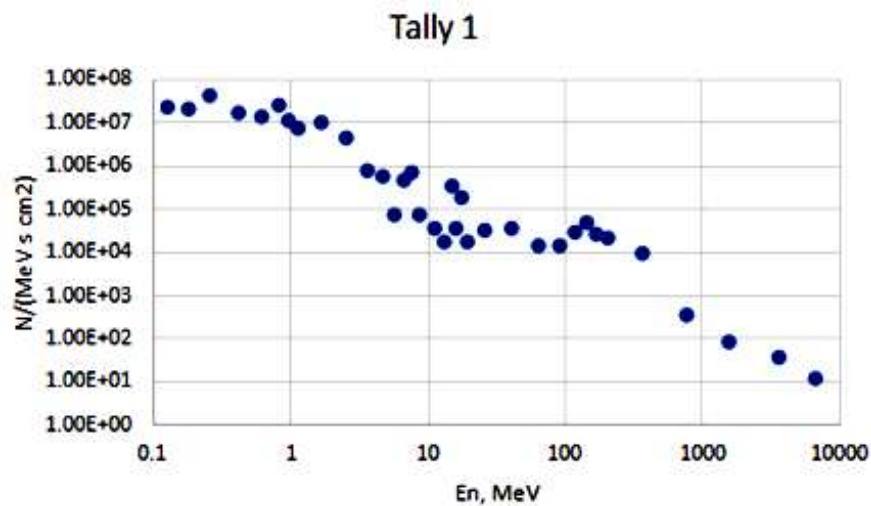


Figure 44: Energy distribution of neutrons (in  $N/(\text{MeV} \cdot \text{s} \cdot \text{cm}^2)$  units) emitted from the Be target, from calculations with the MCNP6 transport code [128].



## 17 Appendix A5: Details of Monte Carlo Study

### 17.1 Particle Identification

For each topology, one primary particle (the proton for the  $K_{Sp}$  channel, the  $\pi K^+$  for the  $\pi^+\Lambda$  channel and the  $K^+$  for the  $K^+\Xi$  and  $K^+n$  channels) provides a rough determination for the position of the primary vertex along the beam line that is used in conjunction with the start counter to determine the flight time and path of the  $K_L$  from the beryllium target to the hydrogen target. Protons, pions, and kaons are distinguished using a combination of  $dE/dx$  in the chambers and time-of-flight to the outer detectors (BCAL and TOF). The energy loss and timing distributions for the  $K_{Sp}$  channel are shown in Fig. 45; the distributions are similar for the  $\pi^+\Lambda$  channel, where a proton band arises from the  $\Lambda \rightarrow \pi^- p$  decay. Also shown is the  $dE/dx$  distribution for the  $K^+\Xi^0$  channel, where a prominent kaon band can be seen, along with pion and proton bands arising from  $\Lambda$  decays.

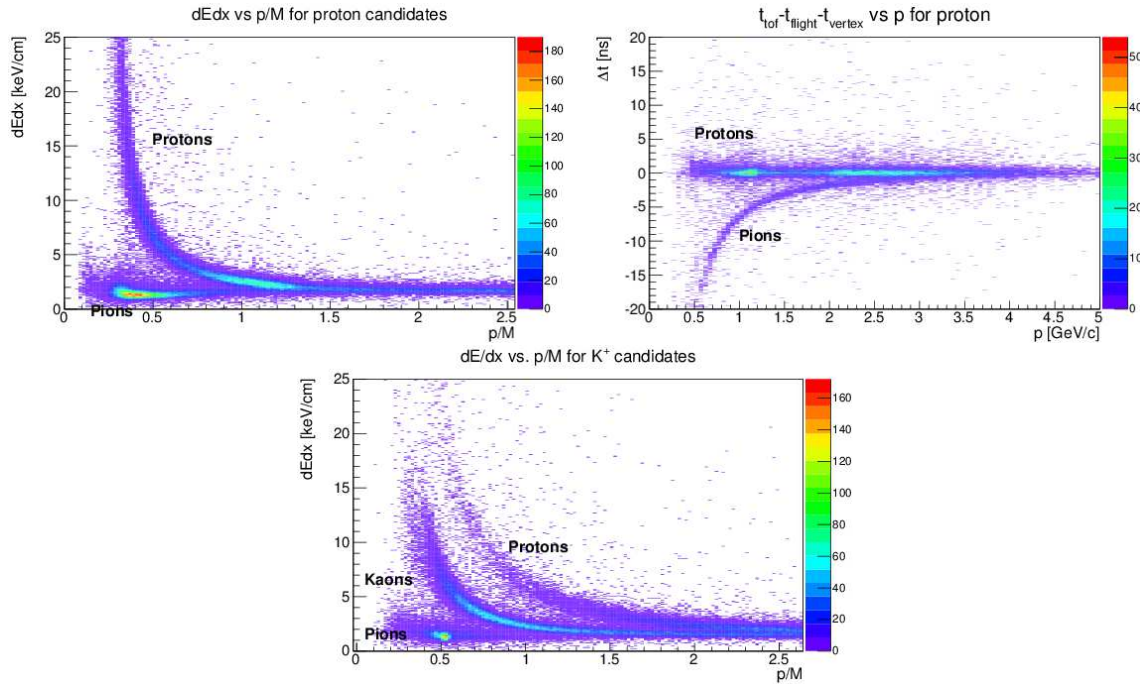


Figure 45: Particle identification. Top left:  $dE/dx$  for the  $K_{Sp}$  channel. Top right: time difference at the primary "vertex" for the proton hypothesis for the  $K_{Sp}$  channel using the TOF. Bottom plot:  $dE/dx$  for the  $K^+\Xi$  channel. The proton and pion bands arise from the decay of the  $\Lambda$ .

Since the GlueX detector has full acceptance in  $\phi$  for charged particles and large acceptance in  $\theta$  (roughly  $1 - 140^\circ$ ), a full reconstruction of events is feasible for the majority of the channels. That will allow to apply four or more overconstrain kinematical fit and improve the resolution considerably. A typical comparison between  $W$  reconstruction using the  $K_L$  momentum for 300 ps ST resolution (red dots) and the other using kinematically fitted final-state particles for the  $K_{Sp}$  channel (blue dots) is shown in Fig. 46.

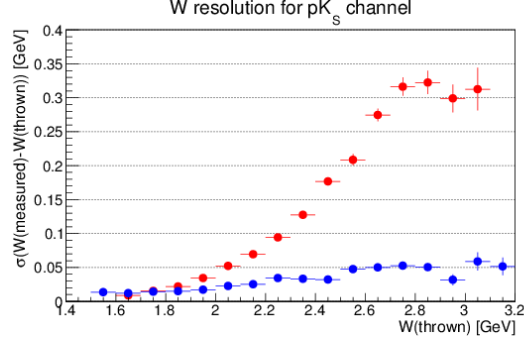


Figure 46:  $W$  resolution for the  $K_{SP}$  channel, (blue dots) using kinematic fitting after reconstruction of all final state particles; (red dots) using  $K_L$  time-of-flight.

### 17.1.1 Details of MC study for $K_{LP} \rightarrow K_{SP}$

For the  $K_{SP}$  channel, we take advantage of the BR of 69.2% for  $K_S \rightarrow \pi^+\pi^-$  [2]: the invariant mass of the  $\pi^+\pi^-$  pair and  $W$  as computed from the four-momenta of the proton and the two pions is shown in Fig. 47.

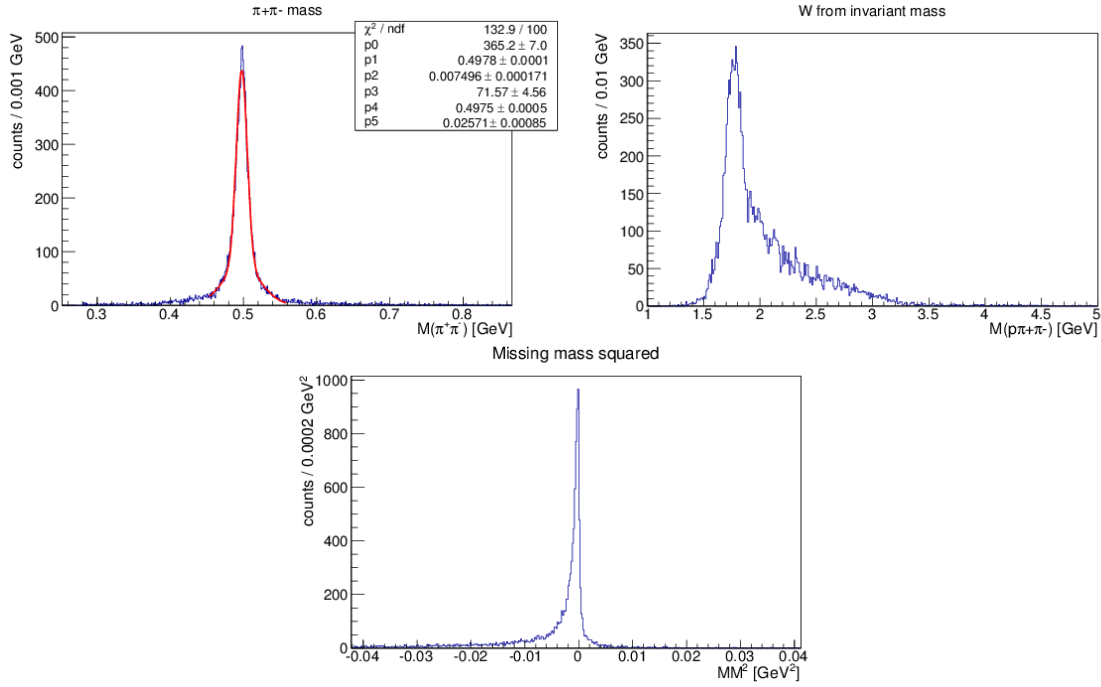


Figure 47: Full reconstruction for  $K_{LP} \rightarrow K_{SP}$  and  $K_S \rightarrow \pi^+\pi^-$ . Top left:  $\pi^+\pi^-$  invariant mass. Top right:  $W$  computed from  $\pi^+\pi^-$  invariant mass. Bottom plot: Missing-mass squared for the full reaction.

After combining the four-momenta of the final-state particles with the four-momenta of the beam and the target, the missing-mass squared for the full reaction should be zero, which is also shown in Fig. 47. Finally, one requires conservation of energy and momentum in the reaction by applying



a kinematic fit to the data. After applying a 0.1 cut on the confidence level of the fit, one computed an estimate for the reconstruction efficiency as a function of  $W$  as shown in Fig. 48. Here the efficiency includes the BR for  $K_S \rightarrow \pi^+ \pi^-$ . The average reconstruction efficiency is about 7%.

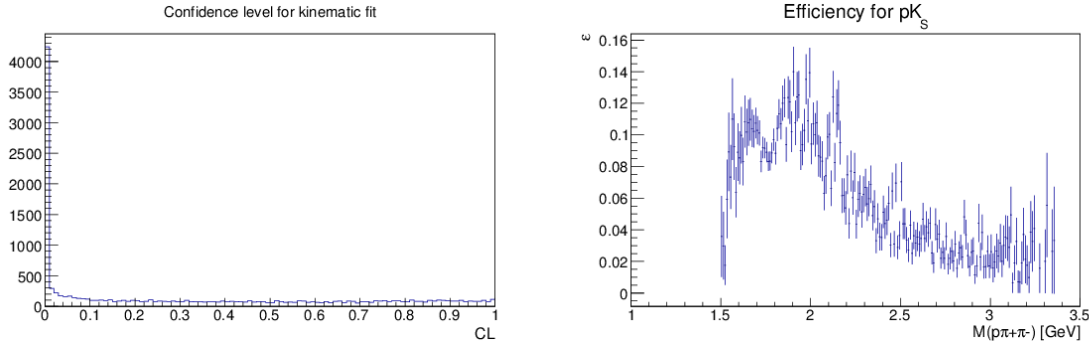


Figure 48: Left plot: Confidence-level distribution for kinematic fit for the  $K_{SP}$  channel. Right plot: Estimate for efficiency for full reconstruction of the  $K_{LP} \rightarrow K_{SP}$  and  $K_S \rightarrow \pi^+ \pi^-$  reaction chain as a function of  $W$ .

### 17.1.2 Details of MC study for $K_{LP} \rightarrow \pi^+ \Lambda$

For our proposed KL Facility in Hall-D, we expect good statistics of  $K_{LP} \rightarrow \pi^+ \Lambda$  for a very wide range of  $K_L$  beam momentum. Figure 49 shows the  $K_L$  beam momentum distributions from the generated (left) and reconstructed (right) with requiring  $\beta_{K_L} > 0.95$  in time-of-flight.

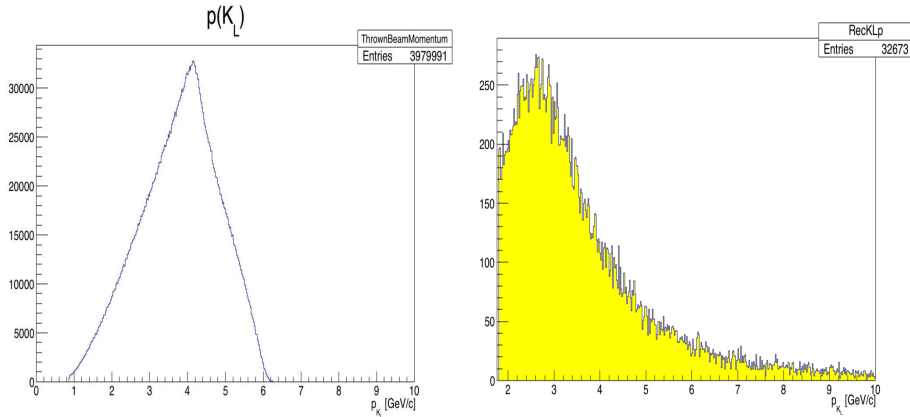


Figure 49: Beam particle ( $K_L$ ) momentum distribution in MC simulation, generated (left) and reconstructed (right).

We have generated the  $K_{LP} \rightarrow \pi^+ \Lambda$  reaction in phase space taking into account the realistic  $K_L$  beam momentum distribution in the event generator. This momentum spectrum is a function of the distance and angle. Then we went through the standard Hall-D full GEANT simulation with GlueX detector and momentum smearing. Finally, we utilized the JANA for particle reconstruction that

we simulated. Figure 50 shows a sample plot for polar angle versus momentum distribution of  $\pi^+$ ,  $\pi^-$ , and protons from the generated event (left) and reconstructed event (right). Figure 51 shows an example of the reconstructed the  $\Lambda$  particle for invariant mass (left) and missing mass (right). We obtained a 5 MeV invariant-mass resolution and a 150 MeV missing-mass resolution. We estimate the expected total number of  $\pi^+\Lambda$  events as final-state particle within topology of  $1\pi^+$ ,  $1\pi^-$ , and 1 proton. In 100 days of beam time with  $3 \times 10^4$   $K_L/s$  on the liquid hydrogen target, we expect to detect around 24M  $K_L p \rightarrow \pi^+\Lambda$  events for  $W < 3$  GeV. Such an unprecedented statistics will improve our knowledge of these states through partial-wave analysis.

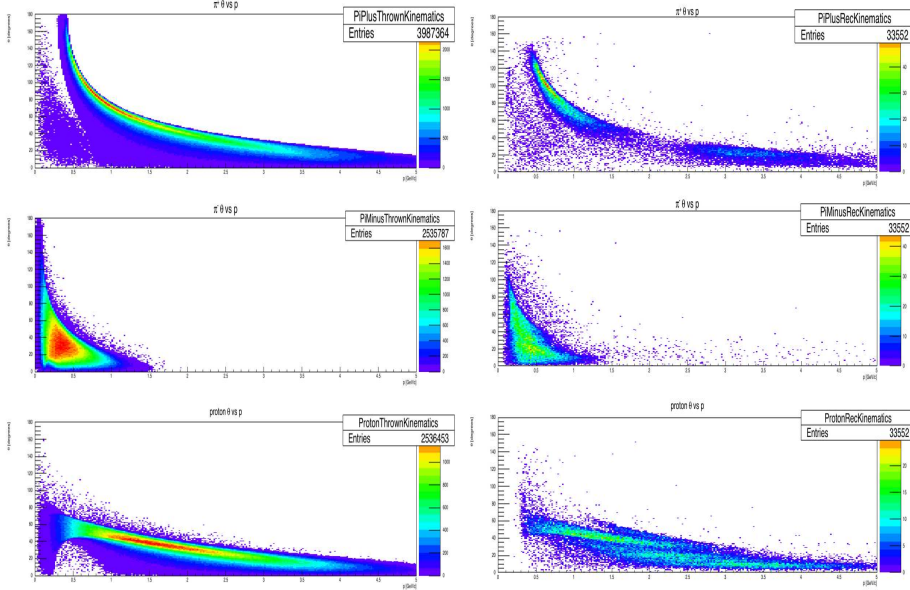


Figure 50: Momentum and angular distributions of  $\pi^+$  (top row),  $\pi^-$  (middle row) and proton (bottom row) of the reaction: generated (left column), reconstructed (right column) events.

Moreover, Fig. 52 (left) shows the correlation between  $\Lambda$  invariant mass from its decay particles ( $p$ ,  $\pi^-$ ) and missing mass of  $\pi^+ X$ . The right plot in Fig. 52 shows the  $\Lambda$  invariant mass as a function of pion angular distribution ( $\theta_{\pi^+}$ ). All these plots are based on the 150 ps time resolution of the ST.

The  $K_L p \rightarrow \pi^+\Lambda$  reaction has a relatively high production cross section the order of a few mb in our proposed  $K_L$  momentum range (1 – 6 GeV/c). The beam resolution has been calculated at the time-of-flight vertex time resolution (150 ps) of the start counter (TOF-ST). The variation of invariant-mass resolution as a function of  $W$  for various TOF-ST timing resolution (100, 150, 300 ps) is similar to those of other reactions [195].

The major source of systematic uncertainty for this reaction would be mistaken particle identification among  $\pi^+$ ,  $K^+$ , and proton in the final state. However, requiring the reconstructed  $\Lambda$  and side-band subtraction technique for background will improve this uncertainty substantially.

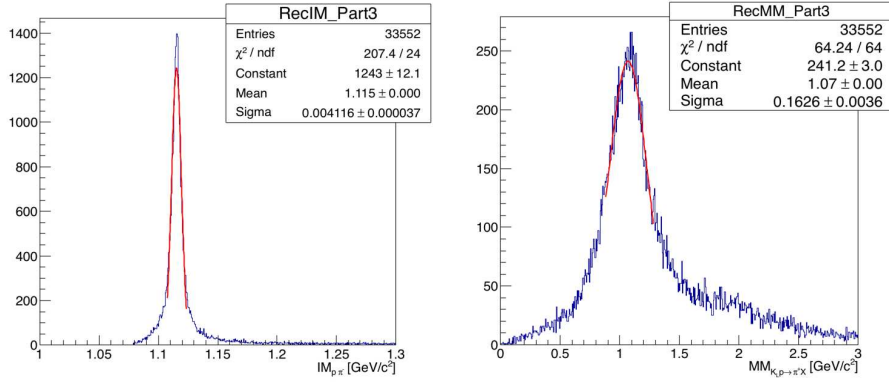


Figure 51: The  $\Lambda$  invariant-mass distribution reconstructed from its  $\pi^- p$  decay particles (left), and the missing mass of  $\pi^+ X$  (right).

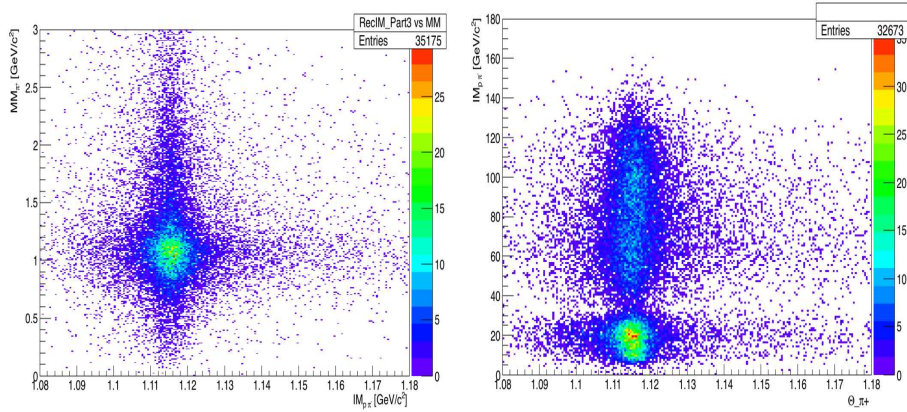


Figure 52: The  $\Lambda$  invariant mass versus missing mass of  $\pi^+ X$  (left) and the  $\theta_{\pi^+}$  angle distribution versus  $\Lambda$  invariant mass (right).

### 17.1.3 Details of MC study for $K_L p \rightarrow K^+ \Xi^0$

Three topologies can be used to reconstruct this reaction. Topology 1 requires the detection of a  $K^+$ , topology 2 requires the detection of a  $K^+$  and a  $\Lambda$  by utilizing its high branching ratio to a  $\pi^- p$  pair (63.9%), and Topology 3 requires the detection of the two-photon decay of the  $\pi^0$  from  $\Xi \rightarrow \pi^0 \Lambda$ . Particle identification is done via a probabilistic approach involving  $dE/dX$ , time-of-flight, and track curvature information as described in Appendix A5 (Sec. 17.1). The  $dE/dX$  distributions for kaon, proton, and  $\pi^-$  candidates are shown in Fig. 53.

At low particle momenta, kaons and protons can be well separated, but high-energy particles cannot be unambiguously differentiated by  $dE/dX$  or by ToF information, which leads to particle misidentification. The higher the  $W$ , the higher ejectile energy we have and the more misidentification contributions we have. In this analysis (specifically Topology 2 and 3), these events were largely removed by making an invariant-mass cut on the  $\pi^- p$  pair.

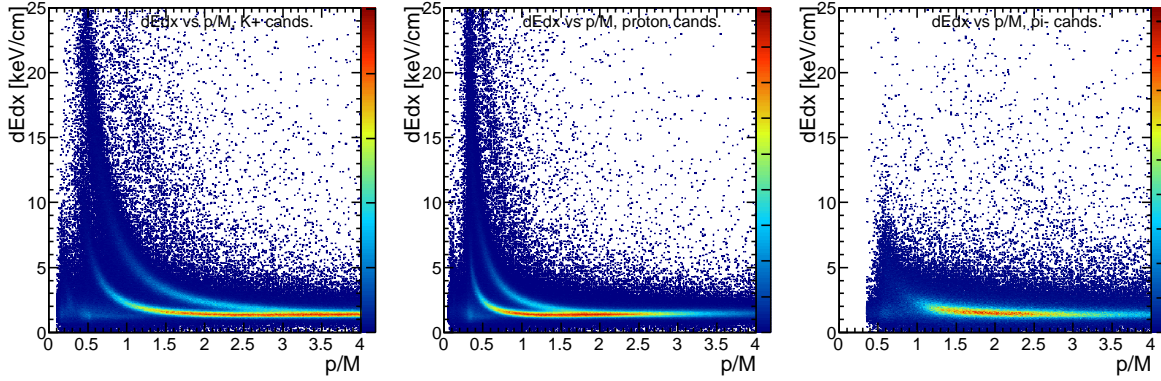


Figure 53:  $dE/dX$  distributions used in kaon proton and  $\pi^-$  identification for the reconstruction of  $K_L p \rightarrow K^+ \Xi^0$ .

Figure 54 shows the missing mass of  $K_L p \rightarrow K^+ X$  for simulated data for the reaction  $K_L p \rightarrow K^+ \Xi^0$  used in the reconstruction of all topologies, the invariant-mass distribution of the  $\pi^- p$  pair used to reconstruct Topology 2 ( $K_L p \rightarrow K^+ \Lambda X$ ) and 3, and the invariant-mass of the two-photon pair used to reconstruct Topology 3 ( $K_L p \rightarrow K^+ \Lambda \pi^0$ ). A  $3\sigma$  cut on these distributions allows us to reconstruct the reaction fully. The left panel of Fig. 54 shows the  $3\sigma$   $W$ -dependent cut applied to select the missing  $\Xi^0$  as well as the  $W$ -dependent  $3\sigma$  cut to reconstruct the reaction  $K_L p \rightarrow K^+ n$ . (See Appendix A5 (Sec. 17.1.4) for more details on the sources of resolution effects on the missing mass.) The latter is one of the major sources of background for our reaction for Topology 1; however, the missing-mass resolution (obtained with a vertex-time resolution of 150 ps) allows a clean separation of these two reactions up to  $W = 2.3$  GeV. Above this value, special treatment of the  $K_L p \rightarrow K^+ n$  background is required as discussed in greater detail in Appendix A5 (Sec. 17.1.3).

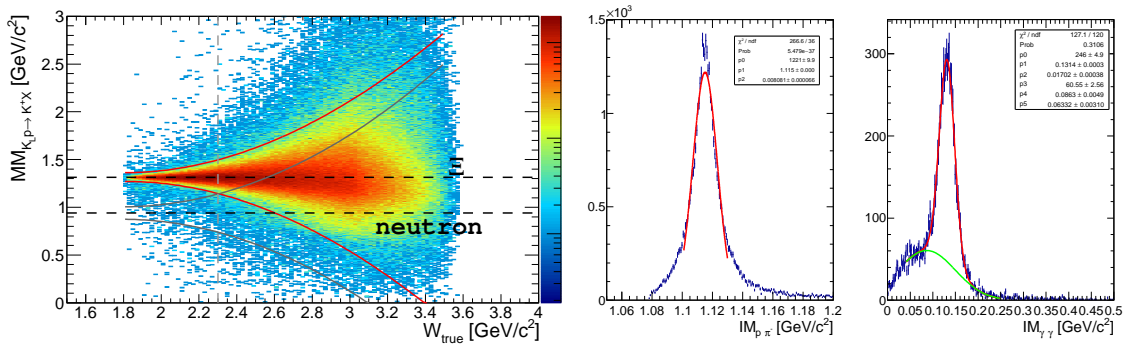


Figure 54: The missing mass of the reaction  $K_L p \rightarrow K^+ X$  used to reconstruct the reaction  $K_L p \rightarrow K^+ \Xi^0$  (Topology 1), and the invariant mass of  $p\pi^-$  pair (Topology 2), and the invariant mass of the two-photon pair (Topology 3).

The detection efficiency as a function of the true  $W$  for each topology is shown in Fig. 55. As expected, the efficiency is highest for Topology 1 reaching a maximum at 60% for  $W = 2.05$  GeV. The efficiency for Topology 2 is about an order of magnitude less than Topology 1, and Topology 3

detection efficiency is on average 0.8%.

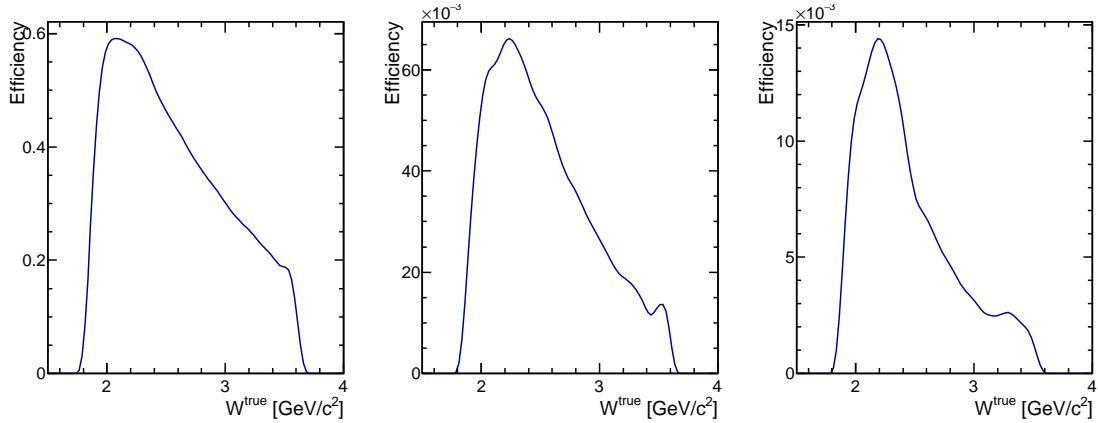


Figure 55: The detection efficiency for the reaction  $K_L p \rightarrow K^+ \Xi^0$  for each topology.

**$K_L p \rightarrow K^+ \Xi^0$  background suppression:** Different sources of background will contribute in the three topologies used to study this reaction. Disentangling our signal  $K_L p \rightarrow K^+ \Xi^0$  from the reaction  $K_L p \rightarrow K^+ n$  (for Topology 1), which has two orders of magnitude larger cross section is expected to be relatively straightforward. As mentioned before, a simple missing-mass cut is sufficient to remove any contributions from this reaction for  $W < 2.3$  GeV. For  $W > 2.3$  GeV, an s-weight approach (or neuralNets, etc.) can be utilized to remove these contribution as the shape of the background under any cascade events can be well established from simulations. Figure 56 shows the  $W$ -dependence of the missing-mass distribution of  $K_L p \rightarrow K^+ X$  for the simulated reactions  $K_L p \rightarrow K^+ \Xi^0$  and  $K_L p \rightarrow K^+ n$  (left panel). The right panel shows the missing-mass projection at  $W = 1.9$  GeV. In addition to  $K_L p \rightarrow K^+ n$ , the reaction  $K_L p \rightarrow \pi^+ \Lambda$  is also a

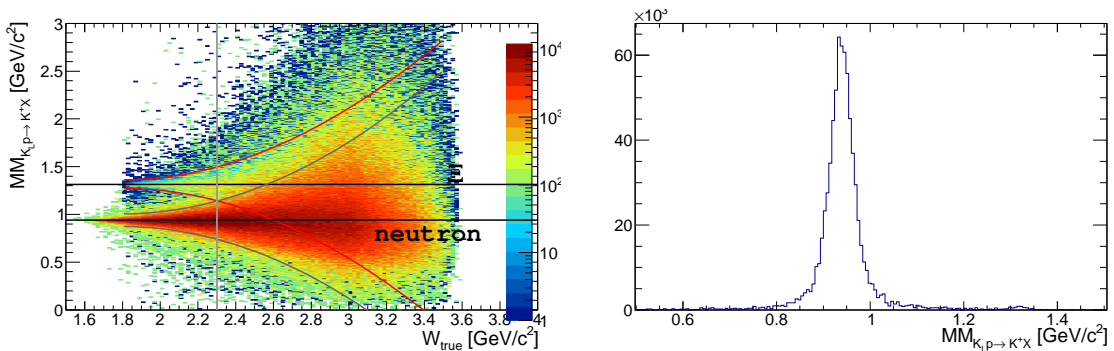


Figure 56: The missing mass of the reaction  $K_L p \rightarrow K^+ X$  used to reconstruct the reactions  $K_L p \rightarrow K^+ \Xi^0$  (Topology 1) and  $K_L p \rightarrow K^+ n$  (which has about 2 orders of magnitude larger cross section). Right panel shows the missing mass at  $W = 1.9$  GeV.

source of background events for Topology 1 ( $K_L p \rightarrow K^+ X$ ) and 2 ( $K_L p \rightarrow K^+ \Lambda X$ ). This channel contributes when the final-state  $\pi^+$  is misidentified as a  $K^+$ . This shifts the missing mass



of  $K_L p \rightarrow \pi^+ X$  to values lower than the ones expected, which leads to a good separation of this source of background below  $W < 2.2$  GeV. Figure 57 shows the missing-mass distribution of these misidentified events. Contributions from these events for Topology 3 is completely removed by the requirement of two photons in the final state that reconstruct the mass of  $\pi^0$ . For Topology 2, coplanarity cuts between the reconstructed (misidentified)  $K^+$  and  $\Lambda$  can reduce contributions, where as a background subtraction approach using the missing-mass information can be used to remove any contribution at  $W > 2.2$  GeV.

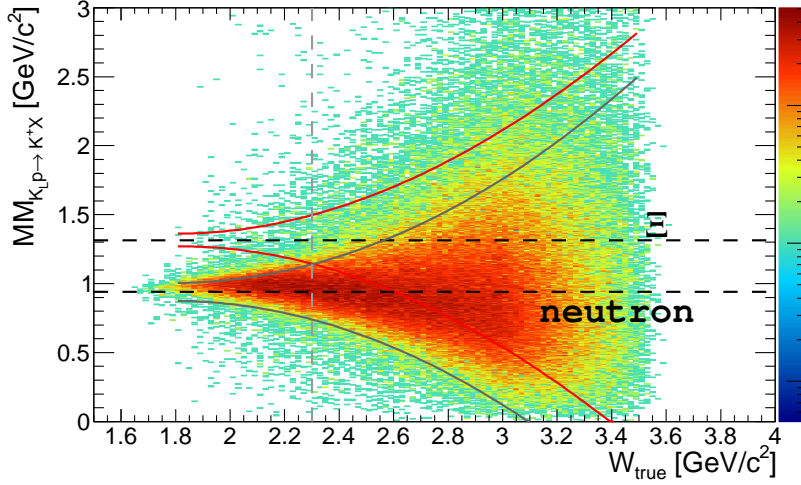


Figure 57: The missing mass of the reaction  $K_L p \rightarrow K^+ X$  for simulated events from the reaction  $K_L p \rightarrow \pi^+ \Lambda$ . The reconstructed events here results from a pion misidentified as a kaon.

**$\Xi^0$  induced polarization:** The parity-violating nature of the cascade's weak decay ( $\Xi^0 \rightarrow \pi^0 \Lambda$ ) yields a pion angular distribution given by

$$n(\theta_\pi^y) = \frac{N}{2}(1 - P_\Xi^y \alpha \cos \theta_\pi^y), \quad (33)$$

where  $P_\Xi^y$  is the induced polarization of the cascade, and is the analyzing power  $\alpha = 0.406 \pm 0.013$  [2]. Figure 58 shows the production plane defined in the center-of-momentum system containing the incoming  $K_L$  and proton target. The decay plane is defined in the rest-frame of the cascade and contains its decay products.

In terms of four-vectors, conservation of energy and momentum for this reaction is written as follows:

$$\mathcal{P}_{K_L} + \mathcal{P}_p = \mathcal{P}_{K^+} + \mathcal{P}_{\Xi^0}. \quad (34)$$

The production plane is then defined by

$$\hat{y} = \frac{\vec{P}_\Xi \times \vec{P}_{K_L}}{|\vec{P}_\Xi \times \vec{P}_{K_L}|}. \quad (35)$$

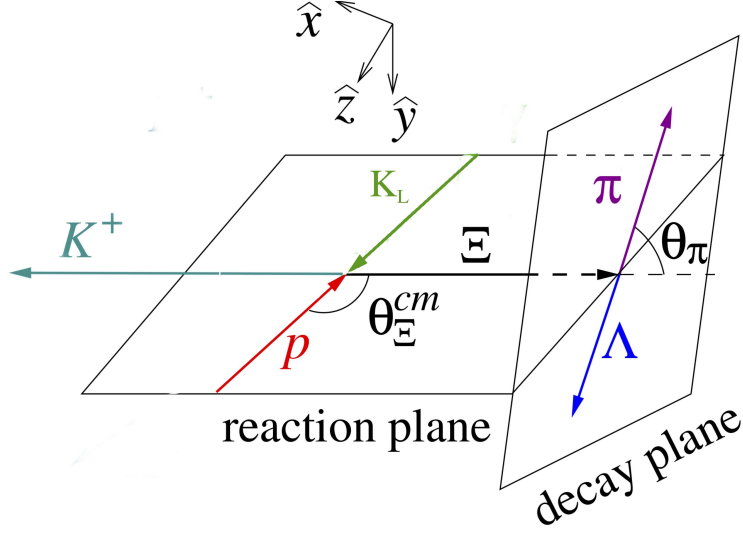


Figure 58: The production plane from  $K_L p \rightarrow K^+ \Xi^0$  defined in the center-of-momentum system containing the incoming  $K_L$  and proton target. The decay plane is defined in the rest-frame of the cascade and contains its decay products. The induced polarization  $P_{\Xi}^y$  is defined to lie perpendicular to the reaction plane.

The  $\hat{z}$  axis lies along the beam direction

$$\hat{z} = \frac{\vec{P}_{K_L}}{|\vec{P}_{K_L}|}, \quad (36)$$

and thus the  $\hat{x}$  axis is defined to give a right-handed coordinate system:

$$\hat{x} = \hat{y} \times \hat{z}. \quad (37)$$

The determination of  $P_{\Xi}^y$  can be established by linear fits to the acceptance-corrected pion angular ( $\cos \theta_{\pi}^y$ ) yields. Fitting these distributions with a first-degree polynomial,

$$y = a_0(1 + a_1 \cos \theta_{\pi}^y), \quad (38)$$

allows the determination of  $a_1$ , which gives us the the induced polarization

$$a_1 = P_{\Xi}^y \alpha. \quad (39)$$

Alternatively, one can determine the induced polarization transfer from determining the forward-backward asymmetry,  $A^y$ , of the pion angular distribution. This asymmetry is defined as

$$A^y = \frac{N_+^y - N_-^y}{N_+^y + N_-^y}, \quad (40)$$

where  $N_+^y$  and  $N_-^y$  are the acceptance-corrected yields with  $\cos \theta_{\pi}^y$  positive and negative, respectively. The asymmetry is related to the induced polarization by

$$P_{\Xi}^y = \frac{-2A^y}{\alpha}. \quad (41)$$



The statistical uncertainty in the asymmetry measurement of  $P_{\Xi}^y$  is related to the Poisson uncertainty in  $N_+^y$  and  $N_-^y$ . Propagating this uncertainty to the uncertainty of  $A^y$  gives

$$\sigma_{A^y} = \frac{2}{(N_+^y + N_-^y)^2} \sqrt{N_+^y N_-^y (N_+^y + N_-^y)}. \quad (42)$$

The uncertainty in  $P_{\Xi}^y$  is then found by propagating  $\sigma_{A^y}$  and  $\sigma_{\alpha}$ :

$$\frac{\sigma_{P_{\Xi}^y}}{P_{\Xi}^y} = \sqrt{\left(\frac{\sigma_{A^y}}{A^y}\right)^2 + \left(\frac{\sigma_{\alpha}}{\alpha}\right)^2}. \quad (43)$$

#### 17.1.4 Details of MC study for $K_L p \rightarrow K^+ n$

As described in Section 11.1.5 we used only  $K^+$  detection to reconstruct this reaction. Kaon identification is done with a probabilistic approach involving  $dE/dX$ , time-of-flight, and track curvature information; see Appendix A5 (Sec. 17.1) for further details. Even in pure  $K_L p \rightarrow K^+ n$  MC case one can have more than one charged particle track reconstructed due to various reactions in the detector volume. That is why in addition to the pronounced  $K^+$  banana in Fig. 59(left) we see some traces of pion and proton bands. At low  $K^+$  momenta, kaons can be well separated from pions and protons, but high-energy particles cannot be differentiated by  $dE/dX$  or by ToF information, which leading to particle misidentification. The higher the  $W$ , the higher the ejectile energy we have and the more kaons we lose due to misidentification; see Fig. 59(right, green). In our analysis, we restricted ourselves to one and only one reconstructed charged-particle track. This condition helps to suppress the background, but does not reduce the reconstruction efficiency; see Fig. 59(right, black).

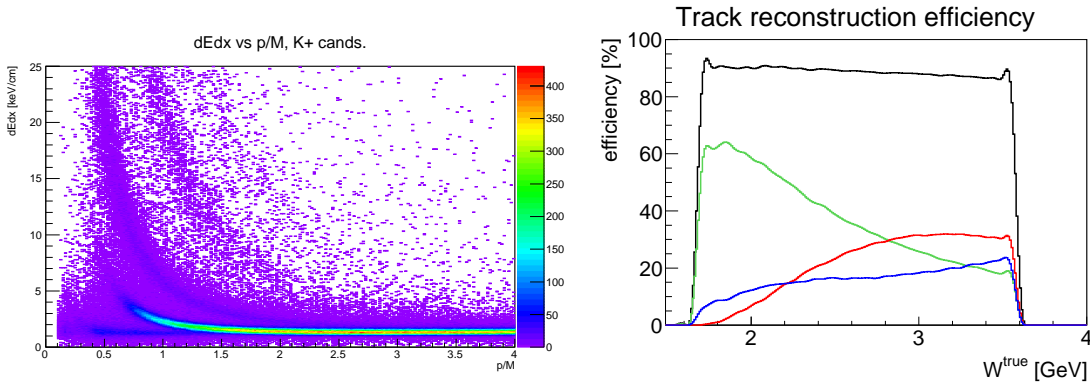


Figure 59: Left plot:  $dE/dx$  for the  $K_L p \rightarrow K^+ n$  channel Right plot: single charged-particle track detection efficiency as a function of  $W$  for the  $K_L p \rightarrow K^+ n$  channel. Any charged particle (black), kaon (green), proton (red), pion (blue).

Charged-particle track detection efficiency stays flat over the full range of  $W$ , but kaon reconstruction efficiency drops from about 60% at low  $W$  to 20% at highest available energy. Since the GlueX acceptance is large and essentially hole-less, kaon reconstruction efficiency does not

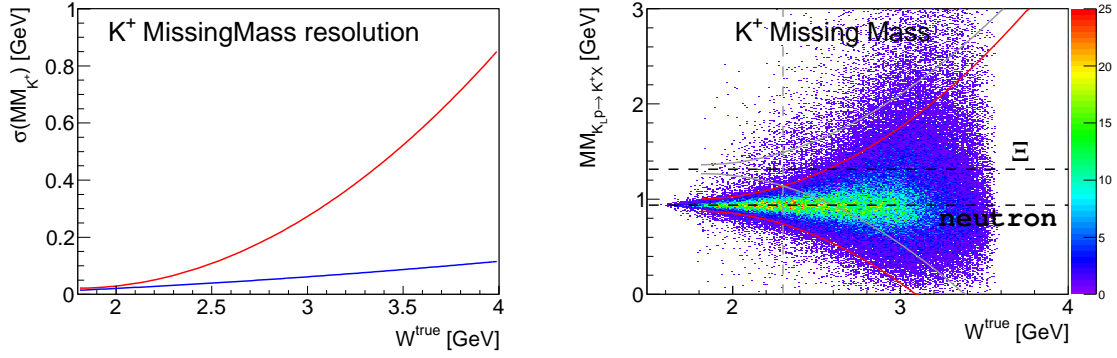


Figure 60: Left plot: Full (red) and detector related (blue)  $K^+$  missing-mass resolution in terms of  $\sigma$ . In second case, the true  $K_L$  momentum was used to calculate the missing mass. Right plot:  $K^+$  missing-mass resolution as a function of  $W$ .  $3\sigma$  missing-mass cuts for the  $K_L p \rightarrow K^+ n$  (red) and  $K_L p \rightarrow K^+ \Xi$  (gray) reactions are indicated by solid lines. Horizontal dashed lines show nominal masses of the neutron and  $\Xi$  baryon. The vertical gray dashed line indicates the range of pure missing-mass separation between these two reactions.

depend on yet unknown angular distributions. For the final selection of the  $K_L p \rightarrow K^+ n$  reaction, we used a  $3\sigma$  missing-mass cut around the neutron's mass; see Fig. 60.

Figure 60 was plotted under the assumption of a 150 ps vertex time resolution. Both  $W$  (Fig. 35) and missing-mass resolutions are driven by the  $K_L$  momentum resolution. That is why a start counter upgrade is essential. Any further time resolution improvement below 150 ps would significantly simplify reaction analysis and background suppression for all reactions of interest.

Below  $W = 2.3$  GeV, the  $K_L p \rightarrow K^+ n$  and  $K_L p \rightarrow K^+ \Xi$  reactions can be disentangled by  $K^+$  missing mass alone. Above this value, special treatment of the  $K_L p \rightarrow K^+ \Xi$  background is required. One may notice that a  $3\sigma$  cut for the  $K_L p \rightarrow K^+ n$  reaction rises faster than for  $K_L p \rightarrow K^+ \Xi^0$ . This effect has a purely kinematical explanation - due to the higher mass of the  $\Xi^0$  baryon, the  $K^+$  produced in  $K_L p \rightarrow K^+ \Xi$  reaction has a lower energy for the same value of  $W$ . The lower the  $K^+$  energy we have, the better missing-mass resolution we get, and the more narrow the missing-mass cut one needs to apply.

**$K_L p \rightarrow K^+ n$  background suppression:** Due to its very high cross section, the  $K_L p \rightarrow K^+ n$  reaction is essentially background free. Due to the extremely high statistics expected for this reaction our uncertainties will be dominated by systematics. We have identified three major sources of physical background:  $np \rightarrow K^+ nn$ ,  $np \rightarrow \pi^+ nn$ , and  $K_L p \rightarrow K^+ \Xi$  reactions.

Details on  $K_L p \rightarrow K^+ n$  and  $K_L p \rightarrow K^+ \Xi$  separation can be found in Appendix A5 (Section 17.1.3). For  $W < 2.3$  GeV, these two reactions can be separated by a  $3\sigma$   $K^+$  missing-mass cut. Above  $W = 2.3$  GeV, one can use standard background suppression techniques - S-weights, Q-weights, NeuralNets, etc. . . . The main decay branch of  $\Xi$  is  $\Xi^0 \rightarrow \pi^0 \Lambda \rightarrow \pi^0 \pi^- p$ , which leads to several charged particles in the final state besides  $K^+$ ; hence filtered out by a "one-charge-track-only" selection criterion. Another decay branch  $\Xi^0 \rightarrow \pi^0 \Lambda \rightarrow \pi^0 \pi^0 n$  cannot be filtered out

that easily; however, due to its smaller branching ratio combined with the small  $K_L p \rightarrow K^+ \Xi$  production cross section, this channel only contributes at the level of  $10^{-3}$  even without any background suppression techniques. Further suppression vetoing multiple neutral tracks and/or Q-weight should push this background far below  $10^{-4}$ .

Neutron flux drops exponentially with energy (see Appendix A4 16 for details) and generally the high-energy neutron flux is small, but nonvanishing. If neutrons and  $K_L$ s have the same speed, they cannot be separated by time of flight. Neutron-induced reactions have high cross sections, which is why one needs to consider them as a possible source of background. In Fig. 61, one can see a comparison of kaon and neutron fluxes for the worse-case scenario when no neutron suppression is employed, similar to Fig. 18(right) in terms of  $\beta$ . Particles with the same  $\beta$  cannot be separated by time of flight. At  $\beta = 0.95$  neutron and kaon fluxes become equal. This speed corresponds to a neutron momentum of  $p_n = 2.9$  GeV/c and kaon momentum of  $p_K = 1.5$  GeV/c.

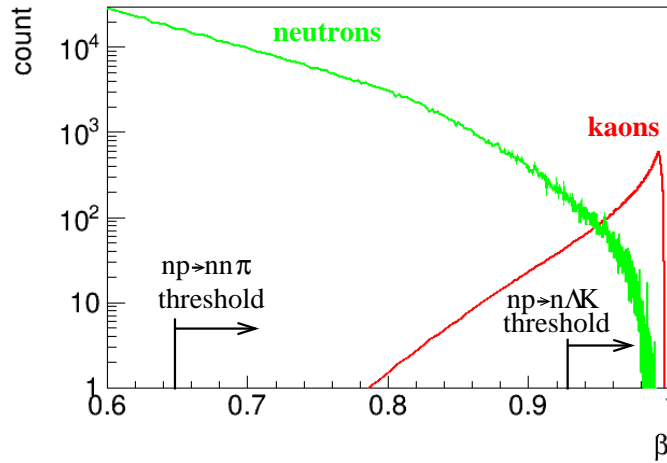


Figure 61: Neutron and  $K_L$  fluxes as a function of speed  $\beta$ .

To evaluate the amount of background, we need to fold this flux with production cross section and reconstruction efficiency. Let's first consider the  $np \rightarrow K^+ \Lambda n$  background. Unfortunately, this reaction is not very well measured, so we would use the  $pp \rightarrow K^+ \Lambda p$  cross-section parametrization together with the knowledge of  $\frac{\sigma(pp \rightarrow K^+ \Lambda p)}{\sigma(np \rightarrow K^+ \Lambda n)} = 2$  from Ref. [196]. In Fig. 62, one can see the flux of  $K^+$ s from kaon-induced  $K_L p \rightarrow K^+ n$  reaction in comparison to a neutron-induced  $np \rightarrow K^+ \Lambda n$  as a function of projectile speeds.

As one can see in Fig. 62, neutron-induced  $K^+$  production contributes only in a very narrow range of energies. The contribution is also very small. One can further suppress this type of background by vetoing charged particles from  $\Lambda$  decay and performing a  $K^+$  missing-mass cut. Altogether one can suppress this type of background below  $10^{-4}$ .

The most dangerous type of neutron-induced background originates from the  $np \rightarrow \pi^+ nn$  reaction with fast  $\pi^+$  misidentification as  $K^+$ . There are no measurements of  $np \rightarrow \pi^+ nn$  reaction but due to isospin symmetry one can relate this reaction to an isospin symmetric case  $np \rightarrow \pi^- pp$ . The later reaction is known, see Ref. [197]. The total cross section for this reaction is about 2 mb. The

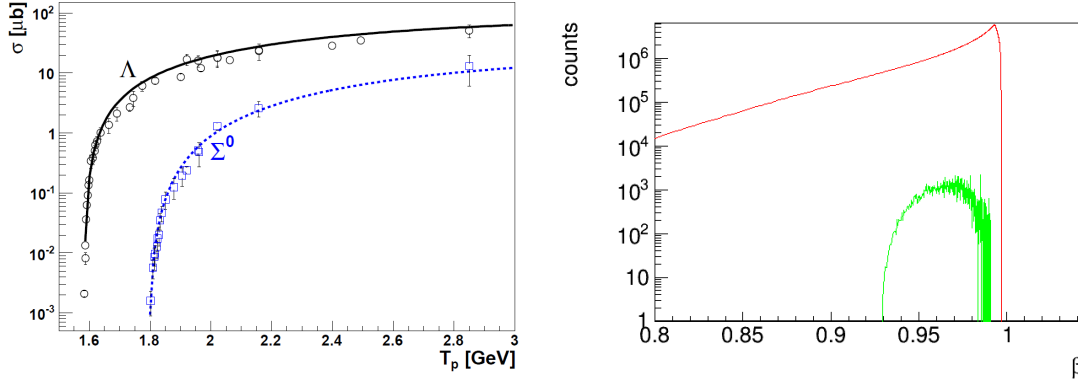


Figure 62: Left plot:  $pp \rightarrow K^+ \Lambda p$  total cross section from Ref. [196]. Right plot:  $K^+$  flux as a function of projectile speed  $\beta$  for neutron-induced (green) and kaon-induced (red) reactions.

$np \rightarrow \pi^+ nn$  reaction has a much lower threshold compared to  $np \rightarrow K^+ \Lambda n$ , so it can utilize an enormous flux of low-energy neutrons. However, low-energy neutrons predominately produce low-energy pions, which can be separated from kaons. The background needs to be considered only for  $\beta > 0.8$ ; see Fig. 63. The background level looks much higher compared to Fig. 62, but it can be severely suppressed with the " $K^+$ " missing-mass cut since pion kinematics of the three-body  $np \rightarrow \pi^+ nn$  reaction are very different from  $K_L p \rightarrow K^+ n$ .

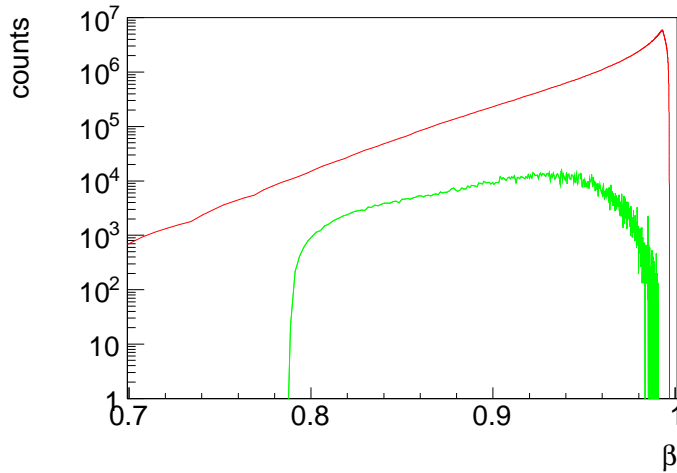


Figure 63:  $K^+$  flux as a function of projectile speed for the  $np \rightarrow \pi^+ nn$  (green) and  $K_L p \rightarrow K^+ n$  (red) reactions. Pion misidentification efficiency for the neutron-induced reaction is extracted from the full MC Geant simulation.

In summary: Kaon particle identification together with a simple  $3\sigma$  missing-mass cut and assumption of  $K_L$  beam can efficiently suppress all physical backgrounds of the  $K_L p \rightarrow K^+ n$  reaction.

## 18 Appendix A6: Current Hadronic Projects

Past measurements involving kaon scattering measurements were made at a variety of laboratories, mainly in the 1960s and 1980s when experimental techniques were far inferior to the standards of today (short summary is given in Sec. 6). It is important to recognize that current projects are largely complementary to the proposed Jlab KL hadron beam facility. We summarize the status of the FNAL, J-PARC, Belle, BaBar,  $\overline{P}$ ANDA, and COMPASS efforts here.

### 18.1 Project X, USA

The status of Project X at FNAL [198,199] is as follows: First stage of Project X aims for neutrinos. Proposed  $K_L$  beam can be used to study rare decays and CP-violation [200]. It may be impossible to use the FNAL  $K_L$  beam for hyperon spectroscopy because of momentum range and  $n/K_L$  ratio (columns 4 and 6 at Table 2). In particular, the 8-yr old FNAL LoI addressed to the CP-violation study proposed to have a neutral kaon beam rate of  $10^{10}$ /hr for high energies and very broad energy binning [201].

Table 2: Comparison of the  $K_L$  production yield. The BNL AGS kaon and neutron yields are taken from RSVP reviews in 2004 and 2005. The Project X yields are for a thick target, fully simulated with LAQSM/MARS15 into the KOPIO beam solid angle and momentum acceptance from Ref. [199].

| Project   | Beam energy<br>(GeV) | Target<br>( $\lambda_I$ ) | $p(K_L)$<br>(MeV/c) | $K_L/s$<br>(into 0.5 msr) | $n/K_L$<br>( $E_n > 10$ MeV) |
|-----------|----------------------|---------------------------|---------------------|---------------------------|------------------------------|
| BNL AGS   | 24                   | 1.1 Pt                    | 300–1200            | $60 \times 10^6$          | $\sim 1 : 1000$              |
| Project X | 3                    | 1.0 C                     | 300–1200            | $450 \times 10^6$         | $\sim 1 : 2700$              |

### 18.2 J-PARC, Japan

While J-PARC has a whole program of charged strange particle and hypernuclear reactions, the photon beam at GlueX KLF allows unique access to other channels. J-PARC provides separated secondary beam lines up to 2 GeV/c (Table 3). The operation of the Hadron Experimental Facility resumed in April of 2015 following a two-year suspension to renovate the facility after the accident that occurred in May 2013 [202]. The primary beam intensity is currently 25 kW, and can be upgraded to 100 kW. This will correspond to  $\sim 10^9$  ppp (particles per pulse) for pion beam intensity and to  $\sim 10^6$  ppp for kaon beam flux. The  $K/\pi$  ratio is expected to be close to 10, which is realized with double-stage electrostatic separators. One of the main problems in the  $K/\pi$  separation is a high duty-factor of the J-PARC Complex.

With  $K^-$  beams, currently there is no proposal specific for  $S = -1$  hyperons, but the cascades will be studied in the early stage of E50 [204], hopefully in this year, 2018. The  $\Delta p/p$  is a few percent, which is not good to look for narrow hyperons. One can think that the systematic study

Table 3: J-PARC Beam line specifications from Ref. [203]

| Beamline | Paricle   | Momentum Range           | Typical Beam Intensity<br>(40 kW MR operation)  |
|----------|---|--------------------------|---|
| K1.8BR   | $\pi^\pm, K^\pm$ , and $p, \bar{p}$ (separated)   | $< 1.1 \text{ GeV}/c$    | $1.5 \times 10^5 \text{ K}^-/\text{spill}$ at $1 \text{ GeV}/c$   |
| K1.8     | $\pi^\pm, K^\pm$ , and $p, \bar{p}$ (separated)   | $< 2.0 \text{ GeV}/c$    | $5 \times 10^5 \text{ K}^-/\text{spill}$ at $2 \text{ GeV}/c$   |
| K1.1     | $\pi^\pm, K^\pm$ , and $p, \bar{p}$ (separated)   | $< 1.1 \text{ GeV}/c$    | $1.5 \times 10^5 \text{ K}^-/\text{spill}$ at $1 \text{ GeV}/c$   |
| High-p   | $\pi^\pm, K^\pm$ , and $p, \bar{p}$ (unseparated) | up to $20 \text{ GeV}/c$ | $> \sim 10^7 \pi^-/\text{spill}$ at $20 \text{ GeV}/c$<br>$> \sim 10^6 \text{ K}^-/\text{spill}$ at $7 \text{ GeV}/c$ |
|          | Primary Proton                                    | 30 GeV                   | $\sim 10^{11}$ proton/spill   |

for  $S = -1$  hyperons even with charged kaons is desirable and J-PARC folks think that such a study is definitely needed but currently there is no room to accept a new proposal to require a long beam line. J-PARC is focusing on hypernuclei physics [205].

There is no  $K_L$  beam line for hyperon physics at J-PARC. It is 100% dedicated to the study of CP-violation. The momentum is spread out from 1 to 4  $\text{GeV}/c$ , there is no concept of  $\Delta p/p$  since the beam cannot be focused with EM devices.

### 18.3 Belle, Japan

The Belle Collaboration at KEK has plenty of  $e^+e^-$  data, and people in Belle [Belle Nuclear Physics Consortium (Belle NPC)] are now extracting various charm-baryon decay processes, which can be used for cascade resonance spectroscopy, from those "raw"  $e^+e^-$  data [206].

### 18.4 BaBar, USA

The BaBar Collaboration at SLAC studied, for instance, properties of the  $\Xi(1530)^0$  in the decay of  $\Lambda_C^+ \rightarrow (\pi^+\Xi^-)K^+$  and  $\Xi(1690)^0$  in the decay of  $\Lambda_C^+ \rightarrow (\bar{K}^0\Lambda)K^+$  [207] (see, for instance, a recent overview by Ziegler [208])

### 18.5 $\bar{P}$ ANDA, Germany

The  $\bar{P}$ ANDA experiment [209] will measure annihilation reactions of antiprotons with nucleons and nuclei in order to provide complementary and in part uniquely decisive information on a wide range of QCD aspects. The scientific scope of  $\bar{P}$ ANDA is ordered into several pillars: hadron spectroscopy, properties of hadrons in matter, nucleon structure and hypernuclei. Antiprotons are produced with a primary proton beam, collected and phase-space cooled in the CR (Collector Ring), and then transferred to the HESR (High Energy Storage Ring) where they are stacked, further phase-space cooled, and then directed onto an internal target located at the center of the  $\bar{P}$ ANDA detector. The facility will start with a luminosity of  $10^{31} \text{ cm}^2/\text{s}$  and a momentum resolu-

tion of  $\Delta p/p = 10^{-4}$ , and later improve to  $2 \times 10^{32}$  and  $4 \times 10^{-5}$ , respectively. The large cross section into baryon-antibaryon final states (e.g.,  $\sim 1 \mu b$  for  $\Xi\bar{\Xi}$  or  $0.1 \mu b$  for  $\Omega\bar{\Omega}$ ) make spectroscopic studies of excited multi-strange hyperons a very compelling part of the initial program of  $\overline{P}$ ANDA, which is expected to commence by 2025 [210].

## 18.6 COMPASS, CERN

COMPASS is thinking of the physics using an RF-separated beam of charged kaons. It is still in the discussion stage. The rates, which were presented as a very first guess by the CERN beamline group were very interesting for a strangeness physics program via diffractive production of strange resonances [211]. The cost of a RF-separated beam is high; however, something like this had been built in the past.

Charged kaons could be used to extend the  $\chi$ PT investigations into the strangeness sector (e.g., Primakoff) and the spectroscopy program. At present, COMPASS filters out kaons in the COMPASS charged pion beam via Cherenkov detectors but they make up only about 2.6% of all beam particles.

The energy of the kaon beam would probably be below 100 GeV but above 40 – 50 GeV. The latter number is defined by the stability of the power supplies for the beam line, which after all is about 1 km long... and of course the decay losses.

## 19 Appendix A7: Additional Physics Potential with a $K_L$ Beam

As stated in the summary of Mini-Proceedings of the Workshop on Excited Hyperons in QCD Thermodynamics at Freeze-Out (YSTAR2016) [212]: a very interesting further opportunity for the KL Facility is to investigate KL reactions on complex nuclei. By selecting events with the appropriate beam momentum together with a fast forward-going pion, events can be identified, in which a hyperon is produced at low relative momentum to the target nucleus or even into a bound state. Baryons with strangeness embedded in the nuclear environment, hypernuclei or hyperatoms, are the only available tool to approach the many-body aspect of the three-flavor strong interaction. Furthermore, appropriate events with a forward-going  $K^+$  could deposit a double-strange hyperon into the remaining nucleus, potentially enabling searches for and studies of double- $\Lambda$  hypernuclei.

Similarly, the scattering of kaons from nuclear targets could be a favorable method to measure the matter form factor (and, therefore, neutron skin) of heavy nuclei, with different and potentially smaller systematics than other probes. The character of the neutron skin, therefore, has a wide impact and the potential to give important new information on neutron star structure and cooling mechanisms [213–217], searches for physics beyond the standard model [218, 219], the nature of 3-body forces in nuclei [220, 221], collective nuclear excitations [222–225] and flows in heavy-ion collisions [226, 227]. Theoretical developments and investigations will be required to underpin such a program, but the science impact of such measurements is high.

Further potential exists to search for – or exclude – possible exotic baryonic states that cannot



easily be described by the usual three-valence-quark structure. Recent results from LHCb provide tantalizing hints for the existence of so-called pentaquarks that include a charm valence quark; however, the interpretation of those results is under discussion. In contrast, elastic scattering of  $K_L$  with a hydrogen target gives unambiguous information on the potential existence of such states. With the given flux of  $K_L$  at the proposed facility, a clear proof of existence or proof of absence will be obtained within the integrated luminosity required for the excited hyperon spectroscopy program that forms the basis of this proposal.

There are two particles in the reaction  $K_L p \rightarrow \pi Y$  and  $KY$  that can carry polarization: the target and recoil baryons. Hence, there are two possible double-polarization experiments: target/recoil. The total number of observables is three. The formalism and definitions of observables commonly used to describe the reaction  $K_L p \rightarrow KY$  is given in Sec. 7. Although one cannot easily measure recoil polarization with GlueX, the self-analyzing decay of hyperons makes this possible. Double-polarization experiments, using, e.g., a polarized target like FROST [136], will however be left for future proposal(s).

The physics potential connected with studies of CP-violating decays of the  $K_L$  is very appealing; however, that topic is not currently the focus of this proposal, since a detailed comparison with the competition from existing and upcoming experiments is needed in order to identify the most attractive measurements that could be done at the proposed KL Facility at JLab.

## 20 Appendix A8: List of New Equipment and of Changes in Existing Setup Required

The following major changes to existing are summarized below.

- Compact photon source (a rough cost estimate is about \$500k).
- Start Counter upgrade.
- The upgrade of the  $LH_2/LD_2$  cryotarget (a rough cost estimate is about \$30k).
- Modifications of the beam line from the beginning of the collimator cave to the cryogenic target, which includes the Be target, the shielding, new vacuum chambers etc:
  - Engineering and design: 0.5FTE\*Y ME and 1FTE\*Y MD<sup>5</sup>.
  - Equipment: \$300k.
  - Changeover from the photon to KL beam line: 4-6 months depending on the type of shielding, at a level of 3.5FTE MT.
  - Changeover from the KL beamline to the photon beam line (after the radiological cooldown of the KL beamline): about 4-5 months.

---

<sup>5</sup> ME,MD,MT - mechanical engineer, designer, technician

## 21 References

### References

- [1] *The 2015 Long Range Plan for Nuclear Science*, <http://science.energy.gov/np/nsac/>.
- [2] C. Patrignani *et al.* (Particle Data Group), *Chin. Phys. C* **40**, 100001 (2016).
- [3] B.M.K. Nefkens,  *$\pi N$  Newsletter*, **14**, 150 (1997).
- [4] R. Koniuk and N. Isgur, *Phys. Rev. Lett.* **44**, 845 (1980).
- [5] H. Al Ghouli *et al.* (GlueX Collaboration), *AIP Conf. Proc.* **1735**, 020001 (2016), *Proceedings of the 16th International Conference on Hadron Spectroscopy (Hadron2015)*, Newport News, VA, Sept. 2015, edited by M. Pennington.
- [6] A. AlekSejevs *et al.* (GlueX Collaboration), arXiv:1305.1523 [nucl-ex].
- [7] Y. Qiang, Ya.I. Azimov, I.I. Strakovsky, W.J. Briscoe, H. Gao, D.W. Higinbotham, and V.V. Nelyubin, *Phys. Lett. B* **694**, 123 (2010).
- [8] W.J. Briscoe, M. Döring, H. Habermann, D.M. Manley, M. Naruki, I.I. Strakovsky, and E. Swanson, *Eur. Phys. J. A* **51**, 129 (2015)
- [9] Web page of the Workshop on *Physics with Neutral Kaon Beam at JLab (KL2016)*, JLab, Newport News, VA, USA, Feb. 2016: <https://www.jlab.org/conferences/kl2016/> contains presentations.
- [10] Web page of the Workshop on *Excited Hyperons in QCD Thermodynamics at Freeze-Out (YSTAR2016)*, JLab, Newport News, VA, USA, Nov. 2016: <https://www.jlab.org/conferences/YSTAR2016/> contains presentations.
- [11] Web page of the Workshop on *New Opportunities with High-Intensity Photon Sources (HISP2017)*, CUA, Washington, DC, USA, Feb. 2017: <https://www.jlab.org/conferences/HIPS2017/> contains presentations.
- [12] M. Albrow *et al.*, Mini-Proceedings of the Workshop on *Physics with Neutral Kaon Beam at JLab (KL2016)*, JLab, Newport News, VA, USA, Feb. 2016, edited by M. Amarian, E. Chudakov, C. Meyer, M. Pennington, J. Ritman, and I. Strakovsky, arXiv:1604.02141 [hep-ph].
- [13] *Physics opportunities with secondary  $K_L$  beam at JLab*, Spokesperson: M. Amarian (GlueX Collaborations), JLab LoI12-15-001, Newport News, VA, USA, 2015.
- [14] *Photoproduction of the very strangest baryons on the proton target in CLAS12*, Spokespersons: L. Guo, M. Dugger, J. Goetz, E. Pasyuk, I.I. Strakovsky, D.P. Watts, N. Zachariou, and V. Ziegler (Very Strange Collaboration for CLAS Collaboration), JLab Proposal E12-11-005A, Newport News, VA, USA, 2013.

- [15] *Nucleon resonance structure studies via exclusive KY electroproduction at 6.6 GeV and 8.8 GeV*, Spokespersons: D.S. Carman, R. Gothe, and V. Mokeev (CLAS Collaboration), JLab E12–16–010A, Newport News, VA, USA, 2016.
- [16] P. Alba *et al.*, Mini-Proceedings of the Workshop on *Excited Hyperons in QCD Thermodynamics at Freeze-Out* (YSTAR2016), JLab, Newport News, VA, USA, Nov. 2016, edited by M. Amarian, E. Chudakov, K. Rajagopal, C. Ratti, J. Ritman, and I. Strakovsky, arXiv:1701.07346 [hep-ph].
- [17] S. Ali *et al.*, Mini-Proceedings of the Workshop on *New Opportunities with High-Intensity Photon Sources*, CUA, Washington, DC, USA, Nov. 2016, edited by T. Horn, C. Keppel, C. Munoz-Camacho, and I. Strakovsky, arXiv:1704.00816 [nucl-ex].
- [18] C. Amsler, S. Eidelman, T. Gutsche, C. Hanhart, S. Spanier, and N.A. Törnqvist, in: Ref. [2]; S. Descotes-Genon, and B. Moussallam, *Eur. Phys. J. C* **48**, 553 (2006).
- [19] J. Julia-Diaz *et al.*, *Phys. Rev. C* **75**, 015205 (2007).
- [20] T. Sato and T.S.-H. Lee, *J. Phys. G* **36**, 073001 (2009).
- [21] Z.-W. Liu *et al.*, *Phys. Rev. D* **95**, 014506 (2017).
- [22] J. A. Oller and U.-G. Meißner, *Phys. Lett. B* **500**, 263 (2001).
- [23] A. Cieplý *et al.*, *Nucl. Phys. A* **954**, 17 (2016).
- [24] K. Moriya *et al.* (CLAS Collaboration), *Phys. Rev. C* **87**, 035206 (2013).
- [25] M. Mai and U. G. Meißner, *Eur. Phys. J. A* **51**, 30 (2015).
- [26] W. Kamleh, *PoS CD15*, 037 (2016).
- [27] N.N. Scoccola *et al.*, *Phys. Lett. B* **201**, 425 (1988); **220**, 658 (1989).
- [28] C. Callan *et al.*, *Phys. Lett. B* **202**, 269 (1988).
- [29] L.Ya. Glozman and D.O. Riska, *Phys. Rept.* **268**, 263 (1996).
- [30] K.-F. Liu *et al.*, *PoS LATTICE2013*, 507 (2014).
- [31] F. Coester *et al.*, *Nucl. Phys. A* **364**, 335 (1998).
- [32] M. Luscher, *Nucl. Phys. B* **354**, 531 (1991).
- [33] K. Rummukainen and S.A. Gottlieb, *Nucl. Phys. B* **450**, 397 (1995).
- [34] S. Aoki *et al.*, *Phys. Rev. D* **76**, 094506 (2007).
- [35] Xu Feng, K. Jansen, and D.B. Renner, *Phys. Rev. D* **83**, 094505 (2011).
- [36] J.J. Dudek, R.G. Edwards, and C.E. Thomas, *Phys. Rev. D* **87**, 034505 (2013).

- [37] D. Guo, A. Alexandru, R. Molina, and M. Döring, Phys. Rev. D **94**, 034501 (2016).
- [38] C. Alexandrou *et al.*, arXiv:1704.05439 [hep-lat].
- [39] J. Bulava, B. Fahy, B. Hörz, K. J. Juge, C. Morningstar, and C. H. Wong, Nucl. Phys. B **910**, 842 (2016).
- [40] C.B. Lang, D. Mohler, S. Prelovsek, and M. Vidmar, Phys. Rev. D **84**, 054503 (2011); Erratum: [Phys. Rev. D **89**, 059903 (2014)]
- [41] P. Guo, J.J. Dudek, R.G. Edwards, and A.P. Szczepaniak, Phys. Rev. D **88**, 014501 (2013).
- [42] R.A. Briceno, and Z. Davoudi, Phys. Rev. D **88**, 094507 (2013).
- [43] U.-G. Meißner, G. Rios, and A. Rusetsky, Phys. Rev. Lett. **114**, 091602 (2015).
- [44] C. Liu, X. Feng, and S. He, Int. J. Mod. Phys. A **21**, 847 (2006).
- [45] M. Lage, U. G. Meißner, and A. Rusetsky, Phys. Lett. B **681**, 439 (2009).
- [46] D.J. Wilson, R.A. Briceno, J.J. Dudek, R.G. Edwards, and C.E. Thomas, Phys. Rev. D **92**, 094502 (2015).
- [47] D.J. Wilson, J.J. Dudek, R.G. Edwards, and C.E. Thomas, Phys. Rev. D **91**, 054008 (2015).
- [48] J.J. Dudek, R.G. Edwards, and C.E. Thomas, Phys. Rev. Lett. **113**, 182001 (2014).
- [49] R.G. Edwards, J.J. Dudek, D.G. Richards, and S.J. Wallace, Phys. Rev. D **84**, 074508 (2011).
- [50] G. P. Engel *et al.* (BGR Collaboration), Phys. Rev. D **87**, 074504 (2013).
- [51] J.J. Dudek and R.G. Edwards, Phys. Rev. D **85**, 054016 (2012).
- [52] R.G. Edwards, N. Mathur, D.G. Richards, and S.J. Wallace (Hadrons Spectrum Collaboration), Phys. Rev. D **87**, 054506 (2013).
- [53] R. Bellwied, S. Borsanyi, Z. Fodor, S.D. Katz, and C. Ratti, Phys. Rev. Lett. **111**, 202302 (2013).
- [54] S. Borsanyi *et al.* (Wuppertal-Budapest Collaboration), JHEP **1009**, 073 (2010).
- [55] A. Bazavov *et al.* (HotQCD Collaboration), Phys. Rev. D **90**, 094503 (2014).
- [56] M. Floris, Nucl. Phys. A **931**, 103 (2014).
- [57] L. Adamczyk *et al.* (STAR Collaboration), Phys. Rev. Lett. **112**, 032302 (2014).
- [58] L. Adamczyk *et al.* (STAR Collaboration), Phys. Rev. Lett. **113**, 092301 (2014).
- [59] P. Alba, W. Alberico, R. Bellwied, M. Bluhm, V. Mantovani Sarti, M. Nahrgang, and C. Ratti, Phys. Lett. B **738**, 305 (2014).

- [60] J. Adam *et al.* (ALICE Collaboration), arXiv:1606.07424 [nucl-ex].
- [61] R. Dashen, S. K. Ma, and H. J. Bernstein, Phys. Rev. **187**, 345 (1969).
- [62] R. Venugopalan and M. Prakash, Nucl. Phys. A **546**, 718 (1992).
- [63] F. Karsch, K. Redlich, and A. Tawfik, Phys. Lett. B **571**, 67 (2003).
- [64] A. Tawfik, Phys. Rev. D **71**, 054502 (2005).
- [65] R. Hagedorn, Prog. Sci. Culture **1**, 395 (1976).
- [66] S. Capstick and N. Isgur, Phys. Rev. D **34**, 2809 (1986).
- [67] D. Ebert, R.N. Faustov, and V.O. Galkin, Phys. Rev. D **79**, 114029 (2009).
- [68] A. Majumder and B. Muller, Phys. Rev. Lett. **105**, 252002 (2010).
- [69] A. Bazavov *et al.*, Phys. Rev. Lett. **113**, 072001 (2014).
- [70] P. Alba *et al.*, arXiv:1702.01113 [hep-lat].
- [71] M. M. Giannini and E. Santopinto, Chin. J. Phys. **53**, 020301 (2015).
- [72] C. Amsler *et al.* (Particle Data Group), Phys. Lett. B **667**, 1 (2008).
- [73] E. Santopinto and J. Ferretti, Phys. Rev. C **92**, 025202 (2015).
- [74] The Durham HEP Reaction Data Databases (UK) (Durham HepData): <http://durpdg.dur.ac.uk/hepdata/reac.html> .
- [75] M.G. Albrow *et al.*, Nucl. Phys. B **23**, 509 (1970).
- [76] M.G. Albrow, in: *Workshop on Physics with Neutral Kaon Beam at JLab: mini-Proceedings*, arXiv:1604.02141 [hep-ph] (February, 2016), p. 5.
- [77] A.D. Brody *et al.*, Phys. Rev. Lett. **22**, 966 (1969).
- [78] S.D. Drell and M. Jacob, Phys. Rev. **138**, B1312 (1965).
- [79] The George Washington University INS Data Analysis Center (SAID); <http://gwdac.phys.gwu.edu> .
- [80] G. Höhler, *Pion-Nucleon Scattering*, Landoldt-Börnstein, Vol. I/9b2, edited by H. Schopper (Springer-Verlag, Berlin, 1983).
- [81] R.A. Arndt, W.J. Briscoe, I.I. Strakovsky, and R.L. Workman, Phys. Rev. C **74**, 045205 (2006)
- [82] D.M. Manley, in: *Workshop on Physics with Neutral Kaon Beam at JLab: mini-Proceedings*, arXiv:1604.02141 [hep-ph] (February, 2016), p. 42.
- [83] H. Zhang, J. Tulpan, M. Shrestha, and D.M. Manley, Phys. Rev. C **88**, 035204 (2013).

- [84] H. Zhang, J. Tulpan, M. Shrestha, and D.M. Manley, Phys. Rev. C **88**, 035205 (2013).
- [85] J.K. Hassall *et al.*, Nucl. Phys. B **189**, 397 (1981).
- [86] H. Kamano, S.X. Nakamura, T.-S.H. Lee, and T. Sato, Phys. Rev. C **90**, 065204 (2014).
- [87] H. Kamano, S.X. Nakamura, T.-S.H. Lee, and T. Sato, Phys. Rev. C **92**, 025205 (2015)
- [88] B. C. Jackson, Y. Oh, H. Haberzettl, and K. Nakayama, Phys. Rev. C **91**, 065208 (2015).
- [89] D.J. Wilson, J.J. Dudek, R.G. Edwards, and C.E. Thomas, Phys. Rev. D **91**, 054008 (2015).
- [90] J.J. Dudek *et al.* (Hadron Spectrum Collaboration), Phys. Rev. Lett. **113**, 182001 (2014).
- [91] Y. Ikeda, T. Hyodo, and W. Weise, Nucl. Phys. A **881**, 98 (2012).
- [92] Z. H. Guo and J. A. Oller, Phys. Rev. C **87**, 035202 (2013).
- [93] A. Cieplý and J. Smejkal, Nucl. Phys. A **881**, 115 (2012).
- [94] M. Mai and U.-G. Meißner, Nucl. Phys. A **900**, 51 (2013).
- [95] P.C. Bruns, M. Mai, and U.-G. Meißner, Phys. Lett. B **697**, 254 (2011).
- [96] P. Estabrooks *et al.*, Nucl. Phys. B **133**, 490 (1978).
- [97] D. Aston *et al.*, Nucl. Phys. B **296**, 493 (1988).
- [98] J. Gasser and U.-G. Meißner, Nucl. Phys. B **357**, 90 (1991).
- [99] U.-G. Meißner and J. Oller, Nucl. Phys. A **679**, 671 (2001).
- [100] J. Oller, E. Oset, and J. Palomar, Phys. Rev. D **63**, 114009 (2001).
- [101] M. Frink, B. Kubis, and U.-G. Meißner, Eur. Phys. J. C **25**, 259 (2002).
- [102] J. Bijnens and P. Talavera, Nucl. Phys. B **669**, 341 (2003).
- [103] T.A. Lähde and U.-G. Meißner, Phys. Rev. D **74**, 034021 (2006).
- [104] V. Bernard and E. Passemar, JHEP **04**, 001 (2010).
- [105] Z.-H. Guo, J. Oller, and J. Ruiz de Elvira, Phys. Rev. D **86**, 054006 (2012).
- [106] J.F. Donoghue, J. Gasser, and H. Leutwyler, Nucl. Phys. B **343**, 341 (1990).
- [107] V. Bernard and E. Passemar, Phys. Lett. B **661**, 95 (2008).
- [108] S. Descotes-Genon and B. Moussallam, Eur. Phys. J. C **48**, 553 (2006).
- [109] J.R. Pelaez and A. Rhodas, arXiv:1703.07661.
- [110] F. Niecknig and B. Kubis, JHEP **1510**, 142 (2015).



- [111] M. Döring, U.-G. Meißner, and W. Wang, JHEP **1310**, 011 (2013).
- [112] D.R. Boito, R. Escribano, and M. Jamin, JHEP **1009**, 031 (2010).
- [113] P. Büttiker, S. Descotes-Genon, and B. Moussallam, Eur. Phys. J. C **33**, 409 (2004).
- [114] [https://wiki.jlab.org/cuawiki/images/3/32/Sergey\\_Abrahamyan\\_WACS\\_NPS\\_2014\\_update.pdf](https://wiki.jlab.org/cuawiki/images/3/32/Sergey_Abrahamyan_WACS_NPS_2014_update.pdf)
- [115] *Polarization observables in wide-angle Compton scattering at photon energies up to 8 GeV*, Spokespersons: B. Wojtsekhowski, S. Abrahamyan, and G. Niculescu (Neutral Particle Spectrometer Collaboration), JLab Proposal PR12-15-003, Newport News, VA, USA, 2015.
- [116] P. Degtyarenko and B. Wojtsekhowski, in: *Workshop on Physics with Neutral Kaon Beam at JLab: mini-Proceedings*, arXiv:1604.02141 [hep-ph] (February, 2016), p. 214.
- [117] T. Horn, C. Keppel, C. Munoz-Camacho, I. Strakovsky, *Workshop on New Opportunities with High-Intensity Photon Sources: mini-Proceedings*, arXiv:1704.00816 [nucl-ex] (February, 2017), p. 61.
- [118] We used modified version of Pythia package for the GlueX Collaboration at JLab Hall D, <http://home.thep.lu.se/torbjorn/Pythia.html>
- [119] A. Titov and T.-S.H. Lee, Phys. Rev. C **67**, 065205 (2003).
- [120] G. McClellan *et al.*, Phys. Rev. Lett. **21**, 1593, (1971).
- [121] A. Titov and B. Kampfer, Phys. Rev. C **76**, 035202 (2007).
- [122] T. Mibe *et al.* (CLAS Collaboration), Phys. Rev. C **76**, 052202 (2007).
- [123] G.W. Brandenburg *et al.*, Phys. Rev. D **7**, 708 (1973).
- [124] I. Larin, in: *Workshop on Physics with Neutral Kaon Beam at JLab: mini-Proceedings*, arXiv:1604.02141 [hep-ph] (February, 2016), p. 198.
- [125] Application Software Group, GEANT - *Detector Description and Simulation Tool*, CERN Program Library Long Writeup W5013, CERN, Geneva, Switzerland (1994).
- [126] L. Keller, private communication, 2015.
- [127] J. Allison *et al.* (Geant4 Collaboration), Nucl. Instrum. and Meth. A **835**, 186 (2016).
- [128] T. Goorley *et al.*, Nucl. Tech. **180**, 298. (2012); <https://mcnp.lanl.gov/>.
- [129] ICRP 116 Publication, *Conversion Coefficients for Radiological Protection Quantities for External Radiation Exposures*, Annals of the ICRP, **40**, No 2-5 (2010)
- [130] D. Androic *et al.*, Nucl. Instrum. Meth. A **646**, 59 (2011).
- [131] M. Spata, private communication, 2016.
- [132] E. Pooser, Ph.D. Thesis, Florida International University (2016).



- [133] F. Barbosa, C. Hutton, A. Sitnikov, A. Somov, S. Somov, and I. Tolstukhin, *Nucl. Instrum. and Meth. A* **795**, 376 (2015).
- [134] G.A. Slayer *et al.*, *Phys. Rev.* **169**, 1045 (1968).
- [135] K.G. Vorseburgh *et al.*, *Phys. Rev. D* **6**, 1834 (1972).
- [136] C. Keith, in: *Workshop on Physics with Neutral Kaon Beam at JLab: mini-Proceedings*, arXiv:1604.02141 [hep-ph] (February, 2016), p. 223.
- [137] D. Meekins, TGT-CALC-401-007: *Hall D Cryogenic Target: General calculations for relief of the LH<sub>2</sub> target*.
- [138] H. Seraydaryan *et al.*, *Phys. Rev. C* **89**, 055206 (2014).
- [139] H. Al Ghoul *et al.* (GlueX Collaboration) arXiv:1512.03699v4 [nucl-ex].
- [140] S. Tylor, in: *Workshop on Physics with Neutral Kaon Beam at JLab: mini-Proceedings*, arXiv:1604.02141 [hep-ph] (February, 2016), p. 205.
- [141] P. Capiluppi, G. Giacomelli, G. Mandrioli, A.M. Rossi, P. Serra-Lugaresi, and L. Zitelli, IFUB-81-25.
- [142] R.J. Yamartino, Ph. D Thesis, SLAC Stanford University, May (1974).
- [143] D.A. Sharov, V.L. Korotkikh, and D.E. Lanskoj, *Eur. Phys. J. A* **47**, 109 (2011).
- [144] S.F. Biagi *et al.*, *Z Phys. C* **34**, 175 (1987).
- [145] J.C.M. Armitage *et al.*, *Nucl. Phys. B* **123**, 11 (1977).
- [146] D. Cline, J. Penn, and D.D. Reeder, *Nucl. Phys. B* **22**, 247 (1970).
- [147] P. Bajllon *et al.*, *Nucl. Phys. B* **134**, 31 (1978).
- [148] A.V. Anisovich and A.V. Sarantsev, *Phys. Lett. B* **413**, 137 (1997).
- [149] C. Cawlfild *et al.*, *Phys. Rev. D* **74**, 031108 (2006).
- [150] R. Delbourgo and M.D. Scadron, *Int. J. Mod. Phys. A* **13**, 657 (1998).
- [151] M.D. Scadron, F. Kleefeld, G. Rupp, and E. van Beveren, *Nucl. Phys. A* **724**, 391 (2003).
- [152] Z.Y. Zhou and H.Q. Zheng, *Nucl. Phys. A* **775**, 212 (2006).
- [153] J. Prevost *et al.* (CERN-Heidelberg-Saclay Collaboration), *Nucl. Phys. B* **69**, 246 (1974).
- [154] W. Cameron *et al.* (Rutherford-London Collaboration), *Nucl. Phys. B* **143**, 189 (1978).
- [155] J. Timmermans *et al.* (Amsterdam-CERN-Nijmegen-Oxford Collaboration), *Nucl. Phys. B* **112**, 77 (1976).

- [156] W. Cameron *et al.* (Rutherford-London Collaboration), Nucl. Phys. B **131**, 399 (1977).
- [157] S. Ceci, M. Döring, C. Hanhart, S. Krewald, U.-G. Meissner, and A. Svarc, Phys. Rev. C **84**, 015205 (2011).
- [158] V.D. Burkert *et al.*, arXiv:1412.0241 [nucl-ex].
- [159] A.V. Anisovich, R. Beck, E. Klempt, V.A. Nikonov, A.V. Sarantsev and U. Thoma, Eur. Phys. J. A **48**, 15 (2012).
- [160] H. Osmanović, Talk at The International Workshop on Partial Wave Analyses and Advanced Tools for Hadron Spectroscopy (PWA9/ATHOS4, Bad Honnef near Bonn (Germany), March, 2017.
- [161] A. Švarc, Talk at The International Workshop on Partial Wave Analyses and Advanced Tools for Hadron Spectroscopy (PWA9/ATHOS4, Bad Honnef near Bonn (Germany), March, 2017.
- [162] G. Höhler,  $\pi$ N Newsletter **9**, 1 (1993).
- [163] N.G. Kelkar and M. Nowakowski, Phys. Rev. A **78**, 012709 (2008), and references therein.
- [164] G.F. Chew and S. Mandelstam, Phys. Rev. **119**, 467 (1960).
- [165] S. Ceci, J. Stahov, A. Švarc, S. Watson, and B. Zauner, Phys. Rev. D **77**, 116007 (2008).
- [166] P. Masjuan, J. Ruiz de Elvira, and J. José Sanz-Cillero, Phys. Rev. D **90**, 097901 (2014).
- [167] A. Š, M. Hadžimehmedović, H. Osmanović, J. Stahov, L. Tiator, and R.L. Workman, Phys. Rev. C **88**, 035206 (2013).
- [168] A. Š, M. Hadžimehmedović, R. Omerović, H. Osmanović, and J. Stahov, Phys. Rev. C **89**, 45205 (2014).
- [169] A. Š, M. Hadžimehmedović, H. Osmanović, J. Stahov, L. Tiator, and R.L. Workman, Phys. Rev. C **89**, 065208 (2014).
- [170] A. Š, M. Hadžimehmedović, H. Osmanović, J. Stahov, and R.L. Workman, Phys. Rev. C **91**, 015207 (2015).
- [171] A. Š, M. Hadžimehmedović, H. Osmanović, J. Stahov, L. Tiator, and R.L. Workman, Phys. Lett. B **755**, 452 (2016).
- [172] Michiel Hazewinkel: Encyclopaedia of Mathematics, Vol.6, Springer, 31. 8. 1990, pg. 251.
- [173] S. Ciulli and J. Fischer, Nucl. Phys. **24**, 465 (1961).
- [174] I. Ciulli, S. Ciulli, and J. Fisher, Nuovo Cimento **23**, 1129 (1962).
- [175] E. Pietarinen, Nuovo Cimento Soc. Ital. Fis. **12A**, 522 (1972).
- [176] E. Pietarinen, Nucl. Phys. B **107**, 21 (1976).

- [177] R.L. Workman, M.W. Paris, W.J. Briscoe, and I.I. Strakovsky, Phys. Rev. C **86**, 015202 (2012).
- [178] D. Rönchen, M. Döring, F. Huang, H. Haberzettl, J. Haidenbauer, C. Hanhart, S. Krewald, U.-G. Meißner, and K Nakayama, Eur. Phys. J. A **49**, 44 (2013).
- [179] M. Döring, C. Hanhart, F. Huang, S. Krewald, U.-G. Meißner, and D. Rönchen, Nucl. Phys. A **851**, 58 (2011).
- [180] M. Döring, C. Hanhart, F. Huang, S. Krewald, and U.-G. Meißner, Nucl. Phys. A **829**, 170 (2009).
- [181] R.A. Arndt, I.I. Strakovsky, and R.L. Workman, Phys. Rev. C **68**, 042201(R) (2003), Ya.I. Azimov, R.A. Arndt, I.I. Strakovsky, and R.L. Workman, Phys. Rev. C **68**, 045204 (2003).
- [182] A.V. Anisovich, E. Klempt, V.A. Nikonov, A.V. Sarantsev, H. Schmieden, and U. Thoma, Phys. Lett. B **711**, 162 (2012).
- [183] R. Tibshirani, J.R. Statist. Soc. B **58**, 267 (1996).
- [184] *The Elements of Statistical Learning: Data Mining, Inference, and Prediction*, T. Hasti, R. Tibshirani, J. Friedman, Springer 2009. second ed.; E-book available at <http://statweb.stanford.edu/tibs/ElemStatLearn/index.html> .
- [185] *An Introduction to Statistical Learning*, Gareth James, Daniela Witten, Trevor Hastie and Robert Tibshirani, Springer 2015; 6th printing; E-book available at <http://www-bcf.usc.edu/gareth/ISL/> .
- [186] B. Guegan, J. Hardin, J. Stevens, and M. Williams, JINST **10**, P09002 (2015).
- [187] J. Landay, M. Döring, C. Fernández-Ramírez, B. Hu, and R. Molina, Phys. Rev. C **95**, 015203 (2017).
- [188] D. Agadjanov, M. Döring, M. Mai, U.-G. Meißner, and A. Rusetsky, arXiv:1603.07205 [hep-lat].
- [189] G. D'Agostini, Nucl. Instrum. Meth. A **346**, 306 (1994).
- [190] R.D. Ball *et al.* (NNPDF Collaboration), JHEP **1005**, 075 (2010).
- [191] L. Wilkinson and G.E. Dallal, Technometrics **23**, 377 (1981).
- [192] T. W. Anderson, and D. A. Darling, Annals of Mathematical Statistics **23**, 193 (1952).
- [193] M. A. Stephens, Journal of the American Statistical Association **69**, 730 (1974).
- [194] M. Döring, arXiv:1603.07265 [nucl-th].
- [195] KLong bi-weekly group meeting, <https://wiki.jlab.org/klproject/index.php/March-1st,-2017>.

- [196] Yu. Valdaou *et al.*, Phys. Rev. C **84**, 055207 (2011).
- [197] P. Adlarson *et al.*, arXiv:1702.07212.
- [198] *Project X Physics Study*, <https://indico.fnal.gov/event/projectxps12> .
- [199] *Project X: Physics Opportunities*, Part 1 edited by S.D. Holmes, arXiv:1306.5022 [physics.acc-ph]; Part 2 edited by A.S. Kronfeld and R.S. Tschirhart, arXiv:1306.5009 [physics.acc-ph]; and Part 3 edited D.M. Asner, P.C. Bhat, S. Henderson, R. Plunkett, arXiv:1306.5024 [physics.acc-ph].
- [200] C. Quigg, private communication, 2015.
- [201] B. Winstein *et al.*, *High precision, high intensivity  $K^0$  physics at the main injector*, FNAL LoI 0804, 1988.
- [202] *Summary of the Report from the Working Group for The External Expert Panel on the Radioactive Material Leak Accident at the Hadron Experimental Facility of J-PARC*; [http://j-parc.jp/en/topics/HDAccident20130827\\_02.p](http://j-parc.jp/en/topics/HDAccident20130827_02.p)
- [203] H. Ohnishi, in: *Workshop on Physics with Neutral Kaon Beam at JLab: mini-Proceedings*, arXiv:1604.02141 [hep-ph] (February, 2016), p. 22.
- [204] H. Noumi *et al.*, *Charmed baryon spectroscopy experiment at J-PARC*, J-PARC Proposal E50, 2012.
- [205] M. Naruki, private communication, 2015.
- [206] K. Abe *et al.* (Belle Collaboration), Phys. Lett. B **524**, 33 (2002); T. Lesiak *et al.* (Belle Collaboration), Phys. Lett. B **605**, 237 (2004).
- [207] B. Aubert *et al.* (BaBar Collaboration), Phys. Rev. D **78**, 034008 (2008); B. Aubert *et al.* (BaBar Collaboration), Phys. Rev. Lett. **97**, 112001 (2006); B. Aubert *et al.* (BaBar Collaboration), Phys. Rev. Lett. **95**, 142003 (2005).
- [208] V. Ziegler, in: *Workshop on Physics with Neutral Kaon Beam at JLab: mini-Proceedings*, arXiv:1604.02141 [hep-ph] (February, 2016), p. 113.
- [209] W. Erni *et al.* ( $\overline{P}$ ANDA Collaboration), arXiv:0903.3905 [hep-ex].
- [210] J. Ritman, invited talk at *Excited Hyperons in QCD Thermodynamics at Freeze-Out Workshop*, see Ref. [10].
- [211] S. Paul, private communication, 2016.
- [212] J. Goity, P. Huovinen, J. Ritman, and A. Tang, in: *Workshop on Excited Hyperons in QCD Thermodynamics at Freeze-Out: mini-Proceedings*, arXiv:1701.07346 [hep-ph], (November, 2016) p. 158.
- [213] A.W. Steiner, M. Prakash, J.M. Lattimer, and P.J. Ellis, Phys. Rep. **411**, 325 (2005).

- [214] C.J. Horowitz and J. Piekarewicz, Phys. Rev. Lett. **86**, 5647 (2001).
- [215] J. Xu *et. al.*, Astrophys. J. **697**, 1549 (2009).
- [216] A.W. Steiner, J.M. Lattimer, and E.F. Brown, Astrophys. J. **722**, 33 (2010).
- [217] B.G. Todd-Rutel and J. Piekarewicz, Phys. Rev. Lett. **95**, 122501 (2005).
- [218] De-Hua Wen, Bao-An Li, and Lie-Wen Chen, Phys. Rev. Lett. **103**, 211102 (2009).
- [219] S.J. Pollock and M.C. Welliver, Phys. Lett. B **464**, 177 (1999).
- [220] M.B. Tsang *et. al.*, Phys. Rev. C **86**, 015803 (2012).
- [221] K. Hebeler, J.M. Lattimer, C.J. Pethick, and A. Schwenk, Phys. Rev. Lett. **105**, 161102 (2010).
- [222] M. Centelles, X. Roca-Maza, X. Viñas, and M. Warda, Phys. Rev. Lett. **102**, 122502 (2009).
- [223] A. Carbone *et. al.*, Phys. Rev. C **81**, 041301(R) (2010).
- [224] L.W. Chen *et. al.*, Phys. Rev. C **82**, 024321 (2010).
- [225] A. Tamii *et. al.*, Phys. Rev. Lett. **107**, 062502 (2011).
- [226] B.A. Li, L.W. Chen, and C.M. Ko, Phys. Rep. **464**, 113 (2008).
- [227] M.B. Tsang *et. al.*, Phys. Rev. Lett. **102**, 122701 (2009).